2
Principles of Drilling and Excavation

Gang Han, Maurice B. Dusseault, Emmanuel Detournay, Bradley J. Thomson, and Kris Zacny

2.1
Introduction

Predicting the performance of drills requires analytical capabilities that account for the tool's characteristics, rock properties and behavior, the temperature, and other parameters. Also, it necessitates understanding the effect of the applied forces, details of the bit, and the interaction with the drilled rock. This chapter covers the principles of drilling and excavation, both analytically and experimentally, and the requirements for optimization of the drilling operation.

2.2
Physical Properties of Rocks

2.2.1
Terrestrial Rocks

The vast array of terrestrial rocks can be simplified into a few basic types. One useful classification scheme is to group rocks via their mode of origin, specifically into igneous, sedimentary, and metamorphic rock types. Igneous rocks are those that solidified directly from a molten state, of which basalt is the prime example. Such rocks can be glassy if quickly cooled, or fully crystalline if allowed to cool slowly. Sedimentary rocks, in contrast, are composed of individual mineral or lithic fragments that have been transported and deposited in layers or strata. These strata have been compacted or re-cemented to form a rock-like mass. Finally, metamorphic rocks are igneous or sedimentary rocks that have altered during burial by heat and/or pressure. The original rock fabric, textures, and mineral assemblages are gradually replaced or overprinted as metamorphism progresses.

Drilling in Extreme Environments. Edited by Yoseph Bar-Cohen and Kris Zacny

ISBN: 978-3-527-40852-8

2.2.1.1 Rock Properties Related to Rock Failure and Breakage

Rock response to external loading depends not only on the level of applied loads, but also on rock properties. Based on their functionalities, there are three categories of rock properties often used in the analysis of rock behavior:

- Elastic properties such as Young's modulus, shear modulus, bulk modulus, Poisson's ratio, bulk compressibility, and grain or matrix compressibility. They define rock elastic deformation.
- Strength properties describing the loading limit a rock could afford and its plastic behavior. There are several strength variables, such as cohesive strength, tensile strength, compressive strength, and internal friction angle.
- Transport properties, for example, rock porosity and permeability, describe the ability of fluid to pass through a rock.

These properties are essential for any analytical or numerical effort to describe or predict rock mechanical behavior. The reliability of their values is at least as important as the prediction method itself, if not more so. Rock properties from these categories are not independent. Often, it is found that they are related to each other either directly or indirectly. For example, rocks with high strength are likely to have high modulus, low Poisson's ratio, and low porosity. In this section, we will first describe each rock property and its connection with others; then, we will briefly discuss the two methods generally applied to determine its value.

2.2.1.2 Elastic Properties

Elastic properties, such as Young's modulus (E), bulk modulus (K), shear modulus (G), and Poisson's ratio (ν), are used to describe elastic deformation of rock under loading. For isotropic rocks in which the properties do not vary with direction, the elastic stress–strain relationship can be written as

$$\sigma_{xx} = (\lambda + 2G)\varepsilon_{xx} + \lambda\varepsilon_{yy} + \lambda\varepsilon_{zz}, \sigma_{xy} = 2G\varepsilon_{xy} \tag{2.1a}$$

$$\sigma_{yy} = \lambda\varepsilon_{xx} + (\lambda + 2G)\varepsilon_{yy} + \lambda\varepsilon_{zz}, \sigma_{yz} = 2G\varepsilon_{yz} \tag{2.1b}$$

$$\sigma_{zz} = \lambda\varepsilon_{xx} + \lambda\varepsilon_{yy} + (\lambda + 2G)\varepsilon_{zz}, \sigma_{xz} = 2G\varepsilon_{xz} \tag{2.1c}$$

where λ and G are the two independent Lamé elastic constants, and subscripts x, y, z are the three Cartesian coordinates. G is also called the shear modulus as it governs shear deformation. The engineering parameters E and ν are related to the two Lamé constants through

$$E = \frac{G(3\lambda + 2G)}{\lambda + G} \tag{2.2}$$

$$\nu = \frac{\lambda}{2(\lambda + G)} \tag{2.3}$$

The shear modulus (G) and bulk modulus (K) are related to Young's modulus and Poisson's ratio through

$$G = \frac{E}{2(1+\nu)} \tag{2.4}$$

$$K = \frac{E}{3(1-2\nu)} \tag{2.5}$$

Their values for some typical rocks are listed in Table 2.1.

Young's modulus, E, is also called the "modulus of elasticity", "tangent modulus", or "stiffness". It is the ratio between stress and strain when rock behaves elastically (Figure 2.1). For a linear rock, its value is a constant, and so stress and strain are related by $\sigma = E\varepsilon_a$, where σ is the axial loading stress and ε_a is the rock strain (i.e., fractional change in length) in the axial loading direction. For a nonlinear rock, the tangent modulus must be defined as

$$E = \frac{d\sigma}{d\varepsilon_a} \tag{2.6}$$

Table 2.1 lists some values of Young's modulus for different rocks.

According to Voigt (1910), the Young's modulus of a "composite" rock can be approximated by

$$\frac{1}{E_{\text{eff}}} = \frac{V_a}{E_a} + \frac{V_b}{E_b} + \frac{V_c}{E_c} + \dots \tag{2.7}$$

where V_a, V_b, V_c are the percentages of different minerals in the rock and E_a, E_b and E_c are the Young's modulus of the respective minerals. Reuss (1929) provided another method to estimate the effective stiffness of multi-minerals rock:

$$E_{\text{eff}} = V_a E_a + V_b E_b + V_c E_c + \dots \tag{2.8}$$

Voight's average assumes uniform strain of the mineral aggregates, whereas Reuss' average assumes uniform stress or pressure in the aggregate. Therefore, the former gives the upper limit and the latter gives the lower limit, and the actual stiffness value will be somewhere between them (Lama and Vutukuri, 1978).

Poisson's ratio, ν, is defined as the ratio between the radial (or lateral) and axial (or longitudinal) strain increments during uniaxial loading, as shown in Figure 2.1:

$$\nu = -\frac{d\varepsilon_r}{d\varepsilon_a} \tag{2.9}$$

It varies over a wide range of possible values in rock: from 0 to 0.5 in principle. Most minerals have values in the range 0.1–0.3, but cracks tend to lower the value of ν, while liquid saturation causes ν to increase.

Rock compressibility, C, may be defined as either linear or volumetric compressibility. Volumetric compressibility is also defined as the inverse of bulk modulus (K):

$$C_b = -\frac{1}{V}\left(\frac{\partial V}{\partial P}\right)_T = \frac{1}{\rho}\left(\frac{\partial \rho}{\partial P}\right)_T \tag{2.10}$$

where V is specific volume at a given pressure P and temperature T, and ρ is the density. The negative sign indicates the compression is taken to be positive. Bulk

Table 2.1 Laboratory mechanical properties of rocks[a] (Lama and Vutukuri, 1978).

Rock	Location and description		ρ (g cm^{-3})	*E* (GPa)	*G* (GPa)	ν	UCS (MPa)	σ_T (MPa)	Remarks
Chalk	USA, Niobrara		1.28	1.24	3.03		0.83		Smoky Hill formation
Claystone	Idaho, Palisades Dam, USA		2.20	2.83	0.04		8.27		Weathered, porous, calcareous, montmorillonite matrix
Dolomite	Oneota, USA		2.45	43.9*	0.34*		86.9	4.41	Porous, massive, fg, 50% of fracture
	Mankato, USA			51.71		0.25	105.5	13.1 (R)	$\phi = 9.5$
Gneiss	Euclides da Cunda Dam, Brazil		2.79	78.4		0.22	32.4		
	Dworshak Dam, USA		2.79	53.6*		0.34	162	6.89	Mg-fg, foliations at 45°. At 50% fract.
Granite	Grand Coulee, Washington, USA		2.61	8.96		0.11	64.81		Slightly altered
	USA		2.66	44.20	16.89		244.07		$R = 18.62–25.5$
				27.37*	15.17*		226.15	7.10	
Limestone	Kansas City, MO, USA		2.10	25.7		0.20	50.6		
	Quebec, Canada			77.22		0.33	293.72		
	Saligo, Mine, TN, USA		2.73	27.17*	11.7*	0.22*	173.0	5.52 (R)	$\phi = 3.4$, fg.
				30.7		0.28			
Mudstone	Bistrica, Bulgaria			0.55		0.28	1.41	0.15	
	Nokanam		2.35				10.8		$\phi = 6.0\%$, silty
Quartz	Kansas, OK, USA		2.72	1.71		0.20	328.88	33.78	$\phi = 2.0\%$ secant at 50
Quartzite	Baraboo, USA		2.62	88.4		0.11	320.10	11	Massive, fg
	Rivett, Canada			10.69		0.27	78.6	10.34 (R)	Fg, competent
Sandstone	Chambers, AZ, USA		2.60	11.03		0.31	32.82		$\phi = 25\%$ tan. 50%
	Bridge Canyon Dam, AZ, USA		2.39	27.58		0.04	90.32	5.17	Ferruginous, mg. Massive, grain = 0.06–2.0 mm
	PA, USA		2.20	8.27*	4.69*	0.11*	86.9	4.1 (R)	$\phi = 12\%$
				16.4		0.27			
	USA	#1	2.06	6.0*	3.2*	0.06*	71.71	3.12 (R)	$\phi = 16\%$, weakly cemented, mg
		#2		6.7*	3.2*	0.05*	55.15	5.19 (R)	
		#3		8.8*	4.4*	0.03*	53.09	5.59 (R)	

Shale	UT, USA	2.81	58.19*	26.61*	0.09*	215.81	17.24 (R)	$\phi = 0.9\%$
	Johathan mine, OH, USA	2.56	11.1*	7.9*	0.29	75.2	2.07	Kaolinite and sericite
	Saligo mine, TN, USA	2.30	13.44*	7.10*	0.02*	110.3	2.76 (R)	Kaolinite and quartz, $\phi = 1.7\%$
			11.93		0.22			
Shale + sandstone	Estancia Valley, USA		4.21		0.39	69.3		Secant at 21 MPa
Siltstone	Alaska, USA + shale	2.76	53.23*	25.30*		256.48	18.62 (R)	$\phi = 0.8\%$
	Alaska, USA + shale + sandstone	2.76	39.92	22.68		184.78	15.17 (R)	$\phi = 1.7\%$

[a]Abbreviations and symbols: fg, fine grained; cg, coarse grained; mg, medium grained; *, dynamic tested; **, saturated or wet; R, test in bending; #1, #2, #3, the directions of loading.

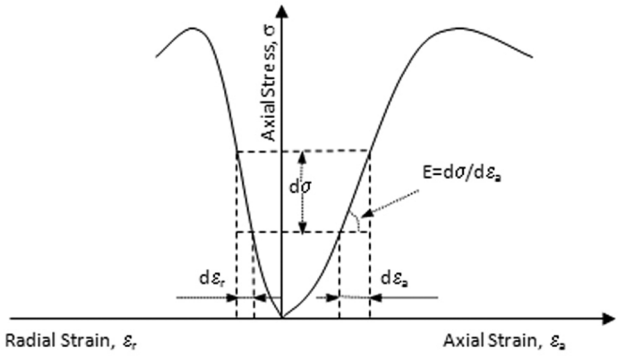

Figure 2.1 Typical rock response during a uniaxial loading test.

compressibility depends on the compressibility of individual grains, pores and cracks. It could range from 0.191 GPa^{-1} for a weak formation to 0.036 GPa^{-1} for an extremely strong formation (Ghalambor, Hayatdavoudl and Koliba, 1994).

Shear modulus, G, is the ratio of shear stress to shear strain during elastic shear deformation. Because rock more often fails in the shear mode, as a result of the difference between loading and confining stresses, it is an important parameter to quantify how much shear deformation a rock undergoes before a shear-failure plane forms (such as the one shown in Figure 2.2).

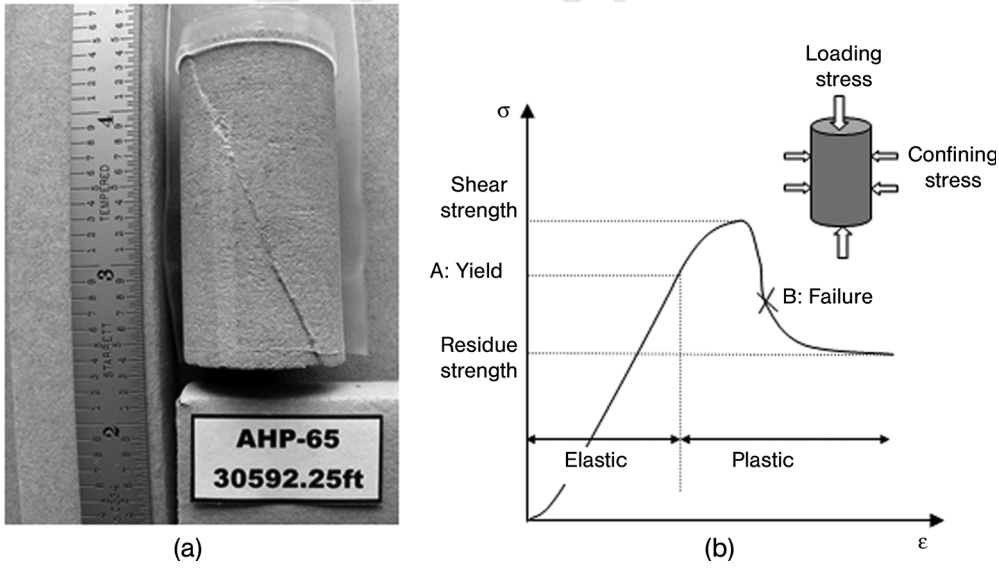

Figure 2.2 (a) Failed rock sample after a triaxial test: the core is one of the deepest from Gulf of Mexico, 30 592.25 ft beneath a drilling platform. (b) Typical stress–strain response in a triaxial test.

2.2.1.3 Strength Properties

When subject to external loading, rock may lose its integrity if the applied force exceeds the rock strength. This leads to rock breakage during drilling and excavation, and also collapse of the borehole, tunnel, or cavern. The mechanical strength of rock is its most crucial property in stability analysis, and it appears in different forms: shear strength, uniaxial compressive strength (UCS), tensile strength, and residual strength.

Shear strength, also called compressive strength, is the maximum compressive stress that a rock can sustain. The resistive forces come from two contributions: the cohesive resistive force (cohesive strength) and the frictional resistive force (frictional strength). Cohesion not only comes from mineral cementation from quartz, calcareous, and ferruginous materials and cohesive bonding such as capillary force, but can also be due to the intergranular fabric, which is an intrinsic property of the contacts among particles. This interlocking mechanism among particle grains must be overcome before grains can slide. Because mineral cements are brittle, strains leading to cohesion loss can be as small as 0.3% (Santarelli and Brown, 1989).

Figure 2.2a shows a sample of failed rock after a confined triaxial test. The sample is one of the deepest from Gulf of Mexico, 30 592.25 ft beneath a drilling platform. It is clearly shown that a shear-induced fracture diagonally extends through the sample. Figure 2.2b illustrates a typical rock mechanical response in a triaxial test, where rock is confined radially and loaded axially. Usually there are two parts of stress–strain curve showing nonlinear trends upon loading (Han *et al.*, 2004): when the rock is initially loaded, and it deforms elastically; and when the load exceeds a certain level, and the rock starts to yield and behave plastically. At the grain scale, the initial stress increase may result in the closure of existing fractures and rearrangement of sand particles to form a denser and stiffer rock. Plastic responses such as yield point A and failure (point B), however, involve larger-scale behaviors such as deterioration of cementation, generation of microfissure arrays, and grain sliding along a macroscopic plane. Also, this response may accompany grain-scale effects such as plastic grain deformation and crushing at elevated stress level.

Various criteria have been developed to estimate the maximum loading that a rock could afford in a compressional mode (Jaeger, Cook and Zimmerman, 2007). The most widely accepted empirical relationship that captures both frictional and cohesive strength factors is the "Mohr–Coulomb" M–C failure criterion:

$$\tau = c_0 + \sigma'_n \tan\varphi \tag{2.11}$$

where τ is the shear strength, φ is the internal friction angle, and c_0 is the rock's cohesive strength. The effective normal stress, σ'_n, is the difference between the rock total stress, σ_n, and the pore pressure, P: $\sigma'_n = \sigma_n - \alpha P$, where α is Biot's poroelastic constant. In a 2D Cartesian coordinate system, the M–C criterion can be written as

$$\sigma'_1 = 2c_0 \tan\beta + \sigma'_3 \tan^2\beta \tag{2.12}$$

where σ'_1 and σ'_3 are the largest and smallest principal stresses, respectively, and β is the failure angle, related to the friction angle through

$$\beta = (\pi/4) + (\varphi/2) \tag{2.13}$$

Another form of the M–C criterion is

$$\sigma'_1 - N\sigma'_3 + S = 0 \tag{2.14}$$

where

$$S = -\frac{2\cos(\varphi)c_0}{1-\sin(\varphi)}$$

and

$$N = \frac{1+\sin(\varphi)}{1-\sin(\varphi)}$$

2.2.1.3.1 **Uniaxial Compressive Strength (UCS)** As shown in Figure 2.3, UCS is the peak stress that rock can sustain during a uniaxial compression test with no lateral confinement, that is, when the confining stress is zero. Usually, it is treated as a benchmark for sand stability because of its ease of measurement. Rock is assumed to be more stable if its UCS is higher. Table 2.1 lists some UCS values of various rocks. It can be estimated from Equation 2.15, by setting the confining stress σ'_3 to zero:

$$\mathrm{UCS} = \frac{2\cos(\varphi)c_0}{1-\sin(\varphi)} \tag{2.15}$$

2.2.1.3.2 **Tensile Strength** When rock is loaded in tension, the maximum resistance to prevent rock from being pulled apart is called the tensile strength. Based on the modified Griffith criterion (Jaeger, Cook and Zimmerman, 2007), the ratio between tensile strength, σ_T, and UCS is

$$\mathrm{UCS} = 4\left(\sqrt{\mu^2+1}-\mu\right)\sigma_T \tag{2.16}$$

where the coefficient of friction is given by $\mu = \tan\varphi$, φ being the friction angle of the Coulomb criterion (often close to 30° for sandstone). Tensile strength is generally much smaller than compressive strength, which indicates that rock fails more easily

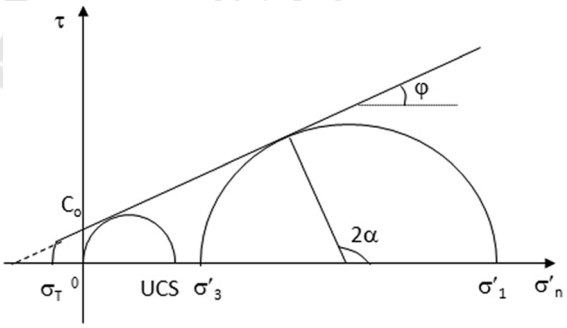

Figure 2.3 Mohr–Coulomb failure criteria.

in tension than in compression. Tensile strength values of some rocks are listed in Table 2.1.

2.2.1.3.3 **Residual Strength** Another strength concept defined in Figure 2.2 is rock residual strength: the strength the rock has after losing its cohesive strength component and original structure integrity. This strength is important to evaluate rock post-failure behavior.

In both crystalline igneous rocks and in sedimentary rocks, there is often a disparity between the strength of an intact rock sample and the strength of individual mineralogical constituents. Rock strength is affected by numerous internal factors, including grain size, mineral cement type, contact patterns, original cracks and fissures, anisotropy, and external conditions such as water saturation, stress state, and loading path. This leads to great difficulties in obtaining accurate rock strength data, especially for *in situ* conditions.

The *modulus of toughness*, M_t, represents the maximum amount of energy that a unit volume of rock can absorb without fracture, and it can be estimated through (Bell, 1978)

$$M_t = \frac{2}{3} \times \mathrm{UCS}\varepsilon_f \tag{2.17}$$

where ε_f is the strain at rock failure. In a laboratory test, this energy is measured as the area under the stress–strain curve, which represents the work required to fail the test specimen.

2.2.1.4 **Transport Properties**

Transport properties mainly refer to rock porosity and permeability, which determine rock fluid flow conductivity. Permeability can be defined by Darcy's law:

$$k = \frac{Q\mu}{A(\Delta P/\Delta L)} \tag{2.18}$$

where Q is the volume flow rate per unit time, μ is fluid viscosity, $\Delta P/\Delta L$ is the pressure gradient in the direction of flow, and A is the cross-sectional area perpendicular to the flow direction. For viscous fluids such as oil or water flowing through the pores, the fluid tends to "stick" to the walls of the pores, developing a thin static boundary layer at the mineral surface. For gases, however, a phenomenon termed "slippage" occurs, which gives rise to an apparent dependence of permeability on pressure, known as the Klinkenberg effect.

Many approaches have been proposed to describe the relationship of permeability to porosity and other rock properties. These approaches can be classified into two categories (Dullien, 1979): geometric permeability models that treat fluid flow in porous media as a network of closed conduits, and statistical permeability models in which a probability law is applied. Among the geometric models, the Carman–Kozeny model is popular because of its simplicity:

$$k = \frac{\phi^3}{5(1-\phi)^2 S^2} \tag{2.19}$$

where S is the specific surface area, defined as

$$S = \sqrt{\frac{\phi_i^3}{5(1-\phi_i)^2 k_i}}$$

and ϕ_i and k_i are porosity and permeability under initial conditions. This model holds relatively well for unconsolidated and weakly consolidated spherical particulate assemblies, if the packing density is not too low (Le Pennec *et al.*, 1998). For sandstones in hydrocarbon reservoirs below the yield level during hydrostatic and nonhydrostatic loading, Holt (1990) recommended the following correlation:

$$K = \frac{a^2}{45}\frac{\phi^3}{(1-\phi)^2} \tag{2.20}$$

where a is the particle radius.

However, it should be noted that permeability can easily deviate from the above equations, and of course relative permeability in multi-phase cases cannot easily be based on such a relationship. For example, Davies and Davies (2001) showed that there is no consistent relationship between porosity and permeability for sand samples from the Gulf of Mexico and southern California when the porosity exceeds 20%. In fact, permeability is dependent not only on porosity and specific surface area, but also on the size distribution, skewness, the topographical arrangement of capillaries, and the amount and location of interstitial fine-grained minerals.

Porosity can be used as an indication of strength. In ceramics with uniform grain size, laboratory measurements show that there is a correlation between UCS and porosity (ϕ) (Sarda *et al.*, 1993):

$$\mathrm{UCS} = \sigma_0 e^{-\beta\phi} \tag{2.21}$$

For alumina, this correlation covers the porosity range 2–62%, and the value of β is 8 or 9 depending on the orientation of the pores with respect to the loading direction. The authors proposed a correlation for porosity up to 30% when quartz content varies from 48 to 99%:

$$\mathrm{UCS} = 258e^{-9\phi} \tag{2.22}$$

Smorodinov, Motovilov and Volkov (1970) related rock compressive strength, σ_c, with porosity ϕ or density ρ for a group of carbonate rocks (porosity between 0.11 and 37.4%):

$$\sigma_c = 2590e^{-0.091\phi} \tag{2.23a}$$

$$\sigma_c = 0.88e^{2.85\rho} \tag{2.23b}$$

Despite the efforts to relate rock strength with porosity, the correlations are completely empirical. In many cases it is difficult to make any, as a wide scatter in strength versus porosity exists (e.g., Plumb, 1994). Therefore, these empirical correlations should not be used unless verified with laboratory tests.

2.2.1.5 Determination of Failure Related to Rock Properties

Based on the magnitude of stress perturbation and its rate of change, strength determination can be divided into static (or experimental) methods and dynamic (or logging-derived correlation) methods. Laboratory and log data could be complementary to each other, if both are available, since none of them could be claimed superior than the other. The most reliable approach to determine rock strength is through triaxial tests of core samples in the laboratory. However, it is time consuming and costly. The core samples are often not readily available and usually damaged to some unknown extent during coring, handling, and transporting processes.

Well logs can reflect *in situ* stress conditions and provide continuous profiles that reveal the trend of formation properties. Unfortunately, since no logging tool directly yields static strength values, dynamic methods have to face tremendous difficulties to interpret and calibrate, and "... no one should be offended by the statement that it is far from being solved, even today." (Raaen *et al.*, 1996).

2.2.1.5.1 **Static Method** Static methods directly measure the rock sample under laboratory conditions after cores have been recovered from specific depths. In order to retrieve the maximum information on rock deformation behavior, many kinds of experiments may be implemented, for example, uniaxial compression test, uniaxial tension test, biaxial compression test, triaxial compression test, and hydrostatic test.

Introduction to Rock Testing Useful measurements of strength and deformation of rocks in the laboratory depend on having high-quality core and good technique. Although many properties are needed for fully coupled analysis, here we focus only on strength and deformation. Other properties can also be measured, such as porosity, mineral density and bulk density, coefficient of thermal expansion, transport properties such as thermal conductivity, permeability, acoustic velocities, electromagnetic properties, and so on.

Index Testing An index test is a quick test carried out on rock to classify it into categories, to yield an estimate strength and stiffness, or to serve as an empirical assessment of the material response. For example, the potential response of shale to aqueous solutions of different chemistry can be empirically assessed by immersion of intact shale pieces or drill chips in prepared solutions in small beakers, and the degree of swelling or slaking after a set period of time can be noted (Dusseault *et al.*, 1983).

Index tests should be carried out systematically on core or drill cuttings so that a consistent picture can be developed, and also for quality control and correlation with other data. Cuttings can be tested with Brinell hardness (Schmitt, Forsans and Santarelli, 1994) or dispersion methods, and also micro-acoustic measurements. Cores or core fragments are usually tested by one or more of the following methods: penetration tests of various types, elastic rebound tests using a calibrated steel mandril, point load tests for strength estimates, and core scratch tests to provide a continuous strength estimate measure along the core axis.

Strength Testing Tensile strength is difficult to measure reliably because the value is highly sensitive to the size and orientation of internal flaws (microcracks), to the nature of preparation of the rock surface, and to the state of core damage. All types of beam bending tests are suspect, direct tensile testing is too difficult, so the standard rock mechanics test of tensile strength is an indirect tensile strength measure based on compression of a disk-shaped segment of core, with a length about 40% the diameter, usually a minimum of 75 mm in diameter.

Uniaxial Compression Strength Testing The standard quick test of core strength is the UCS test. Cylindrical specimens with $L:D$ ratio $\sim 2:1$ are prepared from high-quality core samples so that the ends are flat, parallel, and prepared to a specified degree of surface finish. These specimens are mounted in a compression frame and subjected to an increasing compressive load applied at a consistent specified rate so as to achieve strain-weakening in about 5 min [International Society for Rock Mechanics (ISRM) standards].

If large amounts of core are available, systematic UCS tests are carried out, partly as strength estimates, partly to help correlate with tests such as the core scratch test, and partly to help extrapolate triaxial test data on a limited number of specimens to the larger core data base. It is common practice to take the average of five UCS tests from the same lithostratigraphic unit.

Shear Testing of Interfaces There are circumstances where the shear strength along a bedding plane, a lithological interface (sand/shale interface), or a joint surface is needed. The simplest is the direct shear test without pore pressure control but with variable normal load and vertical deformation measurement (Figure 2.4).

The interface is prepared and mounted in a horizontally split shear box so that the interface will be at the enforced slip plane. A normal load is placed across the interface, and shear load is applied parallel to the future slip plane by a constant displacement rate of the lower half of the box. The small vertical movements at 90° to the shear direction are measured and related to the potential to dilate (or contract) during shear.

Three to five tests on "identical" specimens of the interface are preferred, but seldom possible from core. Normal effective stresses used during testing might be, for example, values of 1, 2, 4, 8, and 15 MPa. It is common simply to carry out one test at a standard chosen normal stress, obtain peak and ultimate strengths, and use these to generate a shear yield criterion to use in analysis.

Triaxial Testing Triaxial tests are the "gold standard" for strength and deformation; entire conferences, books and many papers exist (e.g., Donaghe, Chaney and Silver, 1988; Paterson and Wong, 2005; ISRM website). Three to five cylindrical specimens with $L:D=2:1$ are used to determine the standard full M–C yield criterion over a range of stresses. The group should be as homogeneous as feasible, given the core available. In petroleum engineering, it is common practice to subcore a 25–40 mm diameter plug from a larger core, although larger specimens are of interest if the equipment is available for reasons of scale effects. Precise volume and

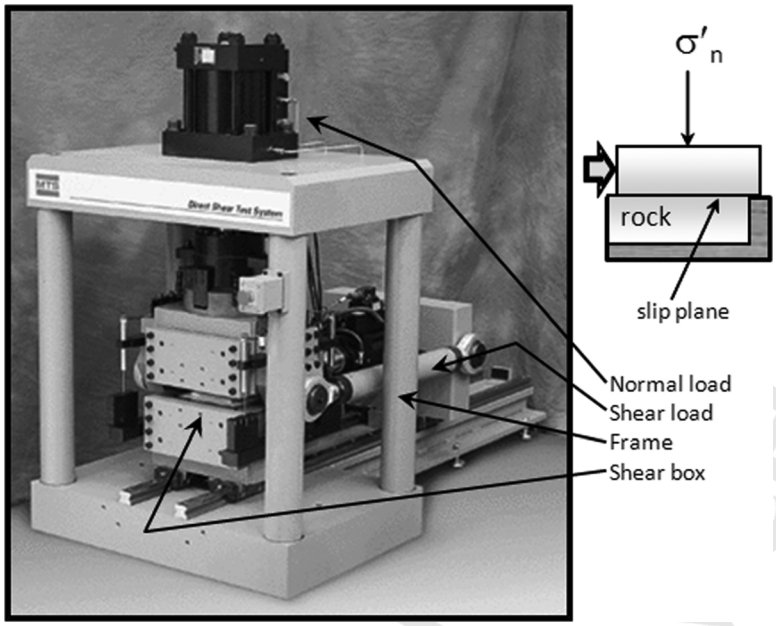

Figure 2.4 Direct shear test of a rock joint. Photograph courtesy MTS Laboratories.

weight measurements are taken from each specimen, and nondestructive tests such as acoustic velocity are applied. The core chunks sawn from each end of the specimen are used for slake-dispersion behavior for shales, point load tests, oriented thin-section preparation, and other index tests.

Figure 2.5 shows a real cell, and Figure 2.6 shows the specimen disposition and a cross-section of a triaxial cell. In a cell such as shown, capabilities include full pore pressure control, axial and radial displacements for deformability, acoustic measurements, cyclic load response, and even thermal expansion to temperatures as high as 200 °C.

A careful, consistent methodology is followed while measuring all parameters such as resistance, expansion, and changes in velocities. Typically, the specimens are failed at 3–5 different values of effective confining stress, such as 0.5, 1, 3, 8, and 15 MPa. During all aspects of the test program, quality control practices are followed to assure that the outcome consists of reliable and useful data. The strength data are now considered suitable to use in design and analysis.

Deformation Properties Deformation data are collected during triaxial tests. Pre-yield axial and radial deformation data, especially those from unload–reload cycles, are converted to values of Young's modulus and Poisson's ratio. Because tests are carried out at different confining stresses, the non-linear relationship between E and σ'_3 can also be explored. The elastic and strength anisotropy of shale and other anisotropic rocks is studied with specimens taken at different orientations. If the major goal of a test program is to obtain highly reliable and systematic deformability data, special test conditions and procedures may be stipulated.

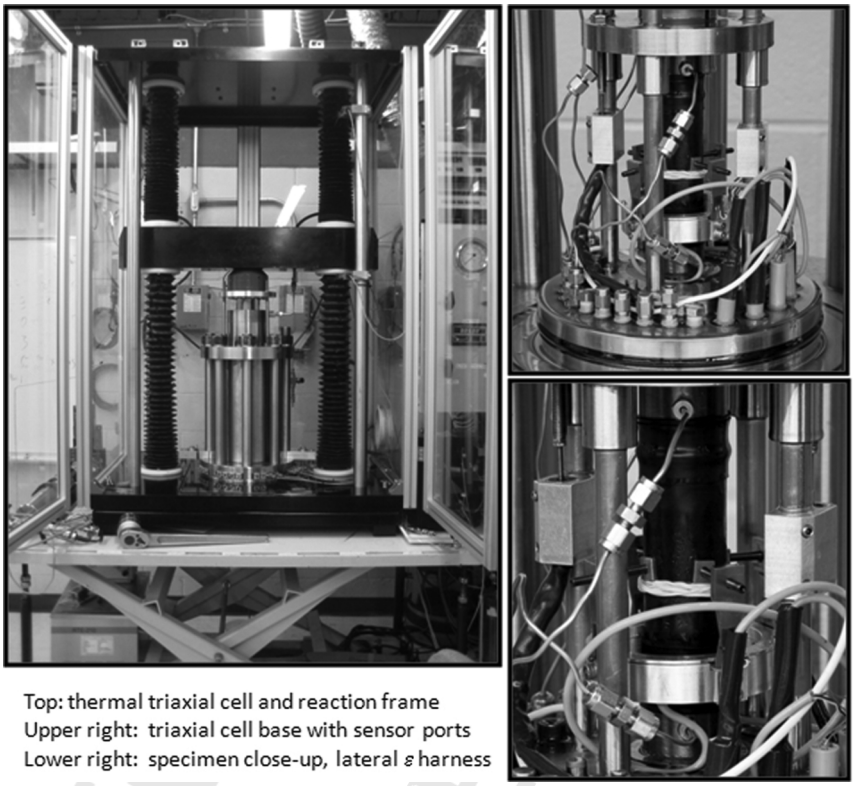

Figure 2.5 A high-capability triaxial apparatus. (a) Thermal triaxial cell and reaction frame; (b) triaxial cell base with sensor ports; (c) specimen close-up, lateral harness. Courtesy Metarock Laboratories.

The volume change behavior of sandstones can be measured through pore liquid volume monitoring in triaxial tests, but because boundary conditions in a test cell are very different from those *in situ*, determining constrained dilation behavior for field applications is far more challenging than simple testing. Compaction behavior or laterally constrained modulus tests ($\varepsilon_x = \varepsilon_y = 0$) are carried out in one-dimensional compaction cells, which can also be used to explore permeability relationships under different strain conditions. Such testing is rarely done for drilling or borehole stability assessment. Deformation tests of shales under ionic diffusion of different species or for thermal conductivity and compressibility require special equipment modifications of uniaxial or triaxial compression cells.

Creep Tests Salt and ductile shales exhibit time-dependent deformation when subjected to significant differential loads, even if temperatures and pressures are kept constant. Salt can squeeze into a borehole during drilling, and shale can deform to cause a tight hole that traps equipment in the hole during trips to change the bit. Evaluating creep behavior over a range of temperatures and confining stresses

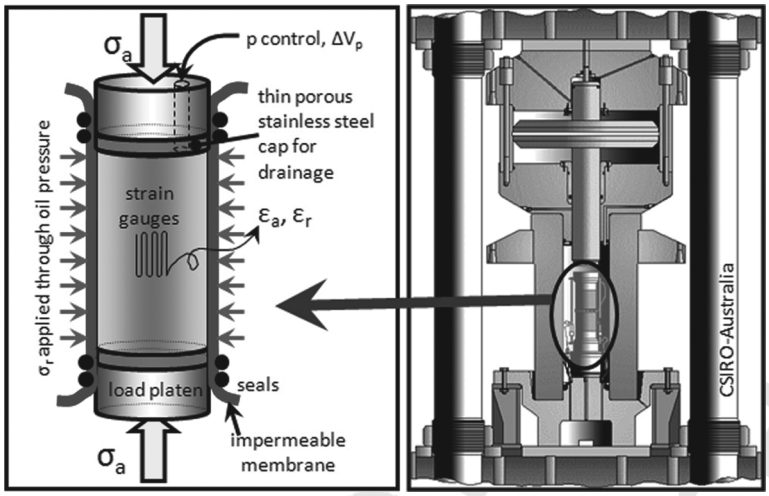

Figure 2.6 Mounted test specimen and a cross-section of a triaxial cell. (Please find a color version of this figure on the color Plates).

requires special creep testing procedures and triaxial cells that can maintain constant loading for weeks, perhaps months (Dusseault and Fordham, 1994). Cylindrical specimens are prepared with flat ends, mounted in a cell (Figure 2.6), and loaded differentially. Deformation data over time are taken for a series of tests at different stress and temperature conditions to delineate the creep behavior over the range of interest.

2.2.1.5.2 **Dynamic Method** In the oil and gas industries, elastic constants are often related to sonic compressional wave velocity, shear wave velocity, bulk density, and shale content. There are four logs that are usually used: gamma ray, sonic, density, and neutron. Density logs give rock bulk density, whereas shaliness can be roughly related to the gamma ray response. A neutron-density cross-plot is deployed to determine total porosity, effective porosity, and clay volume (Schlumberger Educational Services, 1987). Two types of sonic waves are focused on: a compressional wave that is most sensitive to rock density, Young's modulus, and Poisson's ratio, and a shear wave that responds to rock shear modulus. Fluid saturation influences both sonic wave velocities. The high fluid saturation tends to reduce the apparent formation density, stiffness, and strength, and increase rock bulk compressibility. Hence in a multi-phase flow system, introductions of a neutron log and an electrical log are also required.

The rock properties that can be inferred from logs are shear modulus, Young's modulus, bulk compressibility, and Poisson's ratio. Based on acoustic travel velocities (compressional wave velocity v_c and shear wave velocity v_s) and bulk density (ρ_b), King (1969) developed the followings:

$$\text{Young's modulus}: E = \frac{\rho_b v_s (3v_c^2 - 4v_s^2)}{v_c^2 - v_s^2} \tag{2.24a}$$

$$\text{Shear modulus}: G = \rho_b v_s^2 \tag{2.24b}$$

$$\text{Poisson's ratio}: \nu = \frac{v_c^2 - 2v_s^2}{2(v_c^2 - v_s^2)} \tag{2.24c}$$

$$\text{Bulk compressibility}: C_b = \frac{1.0}{\rho_b\left(v_c^2 - \frac{4}{3}v_s^2\right)} \tag{2.24d}$$

In addition to v_p and v_s used directly to determine rock elastic properties, the simple velocity ratio v_p/v_s may indicate whether formations are consolidated or unconsolidated and if gas or oil is present. Gardner and Harris (1968) showed that v_p/v_s values greater than 2.0 were characteristic of water-saturated unconsolidated sands, and values less than 2.0 indicated either a well-consolidated rock or the presence of gas in unconsolidated sand. Gregory (1976) confirmed this conclusion, and found that the ratio varies from 1.42 to 1.98 for water-saturated rocks and from 1.30 to 1.69 for gas-saturated rocks. Furthermore, the effect of increasing the gas saturation is to decrease v_p/v_s by 3–30% in consolidated rocks. The stress level was found to reduce the acoustic velocity ratio to some extent, but the effect was not always consistent or predictable over a wide range of porosity.

2.2.1.5.3 **From Logs to Strength** Unfortunately, rock strength cannot be measured by logs. However, it can be estimated based on the elastic properties interpreted from log data. Various empirical correlations have been attempted; some examples are the following:

- Tokle, Hosrud and Bratli (1986) combined different logs into one equation to determine the UCS:

$$\text{UCS} = a\text{GR}' + b\text{DT}' + c\text{RHOB}' + d\text{NPHI}' + e\text{CAL}' + f\text{ROK}' + \ldots \tag{2.25}$$

where a, b, c, d, e, and f are constants to be determined statistically by regression analysis, GR is natural gamma in API units, DT is the acoustic travel time in $\mu s\ ft^{-1}$, RHOB is the bulk density in $g\ cm^{-3}$, NPHI is the neutron porosity (dimensionless), CAL is the hole caliper in inches, and ROK is a "rock number" obtained from a numerically calculated lithology log as a recombination of several other logs. The prime (′) means those log parameters are normalized and dimensionless.

- "VOLVAN", described by Coates, Schluze and Throop (1982), calculated a shear strength through

$$\sigma_c = \frac{1.125E(1 - V_{sh}) + 2.0EV_{sh}}{C_b \times 10^{10}} \tag{2.26}$$

while C_b is rock bulk compressibility and shale content V_{sh} is derived through gamma ray logs.

- Bruce (1990) calculated UCS from bulk compressibility, shear, and compressive sonic velocities, and gamma ray data from a nearby well, with the gamma ray data first converted to a volume of clay log:

$$\mathrm{UCS} = a \times 0.026 \times 10^{-6} EK_b[0.008V_{sh} + 0.0045(1-V_{sh})] \tag{2.27a}$$

where $a = 2\cos\varphi/(1-\sin\varphi)$, φ being the internal friction angle, and unit is ANSI standard. Tensile strength is calculated from

$$T = \mathrm{UCS}/12 \tag{2.27b}$$

Coates and Denoo (1981) derived shear strength from

$$\sigma_c = \frac{0.025 \times 10^6}{C_b} \times \mathrm{UCS} \tag{2.28}$$

The sand strength UCS can be determined by using Mohr's circle analysis:

$$\mathrm{UCS} = 0.087 \times 10^{-6} EK_b[0.008V_{sh} + 0.0045(1-V_{sh})] \tag{2.29}$$

It should be noted that, since all of the currently available methods are based on empirical correlations that have been developed and calibrated to geographically limited areas, precautions should be used before trying them in a formation.

2.2.1.5.4 **Static versus Dynamic** Rock mechanical properties derived in the laboratory are often different from those from log measurements. Dynamic elastic constants are consistently higher than the static constants, especially for weak rocks and at low confining stresses. In addition to core damage induced before the sample arrives at the laboratory, which almost inevitably leads to uncertainties in laboratory data, the difference between static and dynamic measurements is also related to the effect of stress level, rock anisotropy, fluids, and so on.

Certain mechanisms responsible for rock failure, such as the creation of shear bands, shear dilation, the crushing of grain contacts, and pore collapse, can only be activated with high loading force and large rock deformation. Even though these conditions could be fulfilled conveniently in the laboratory, logging activity can only apply a much smaller dynamic load, and rock is nowhere near yield.

Many tests have witnessed the compressional and the shear wave velocities varying with increased confining stress (e.g., Morita *et al.*, 1992). The shear wave velocity declines at a lower stress level whereas the compressional wave velocity increases with higher confining stress before failure. Rock anisotropy tends to reduce as greater confining stress suppresses the onset of non-elastic behavior.

Fluid types and saturation in the cores tested in the laboratory may be very different from the *in situ* conditions, which also contributes the difference between logging- and laboratory-derived rock properties. The replacement of gas with brine substantially increases the compressional wave velocity and reduces the rate of increase with stress. Further, fluid saturation effects on compressional and shear wave velocities are much larger in low- than in high-porosity rocks (Gregory, 1976). This observation is strengthened by elevated pressures but is absent at atmospheric pressure.

In a few cases, however, static data are very close to or even the same as dynamic results. For example, the static and dynamic moduli were in close agreement if the rock is at high hydrostatic confining pressures in excess of 30 000 psi (Simmons and

Brace, 1965) or if a rock has very low and sparsely disseminated porosity, such as igneous rock or dense quartzite (Tixier, Loveless and Anderson, 1975).

2.2.2 Extraterrestrial Rocks

As surface exploration of neighboring planetary bodies continues to increase in scope and complexity, subsurface drilling will likely play a larger and more important role in future exploration. Drilling provides a means to retrieve samples from depths that are either impractical or impossible to obtain via other methods. In this section, we review the known physical and mechanical properties of planetary materials as determined by direct sampling and by penetrometry.

2.2.2.1 Lunar Drill Core Samples

Although information about the physical and mechanical properties of extraterrestrial materials is available from a number of different sources (including meteorites, *in situ* measurements from landed spacecraft, and inferences from remote measurements), the only returned cores from extraterrestrial drilling operations were collected by the Apollo astronauts and Soviet robotic spacecraft on the lunar surface. Lunar drill cores were collected from a total of nine locations: from the five Apollo sites (Apollo 11, 12, 14, 15, 16, and 17) and from three Luna sites (Luna 16, 20, and 24).

These drill cores provide the best estimates of the *in situ* material properties, such as bulk density, of the lunar regolith. (The traditional definition of a terrestrial soil is a mix of minerals and organics; since lunar surface material lacks organics, the term lunar regolith is preferred over lunar soil.) Formed from repeated bombardment of micrometeorites over time, the lunar regolith is composed of lithic fragments, mineral fragments, and impact breccias, glasses, and agglutinates (impact glass-welded aggregate particles). Heterogeneous at all scales, the regolith is dominated by angular shards and rounded melt fragments with typical median grain diameters between about 45 and 100 μm (e.g., McKay *et al.*, 1991 and references therein). Some 10–20% of particles are less than 20 μm in diameter, representing a significant inhalation hazard in addition to being a problem for joints, seals, and other mechanical implements.

Among the most unexpected properties of the lunar regolith encountered during drilling is the degree of compaction in lower sections of the cores. Relative density (R_D) is a metric of degree of compaction relative to an idealized hexagonal close-packing arrangement of particles, with an R_D value approaching 0% corresponding to an exceptionally loose granular material and a value approaching 100% corresponding to a very densely packed material (Carrier, Mitchell and Mahmood, 1973). Although R_D has been superceded by the parameter maximum index density (ASTM, 2000), it nonetheless provides insight into the nature of lunar regolith. Below a depth of 10–20 cm, the lunar regolith has a relative density approaching 90% (Figure 2.7a). This value is far in excess of values found in typical terrestrial compacted soil and is attributed to the cumulative effects of shock compaction from repeated surface impact cratering (Carrier, Olhoeft and Mendell, 1991). Such a high

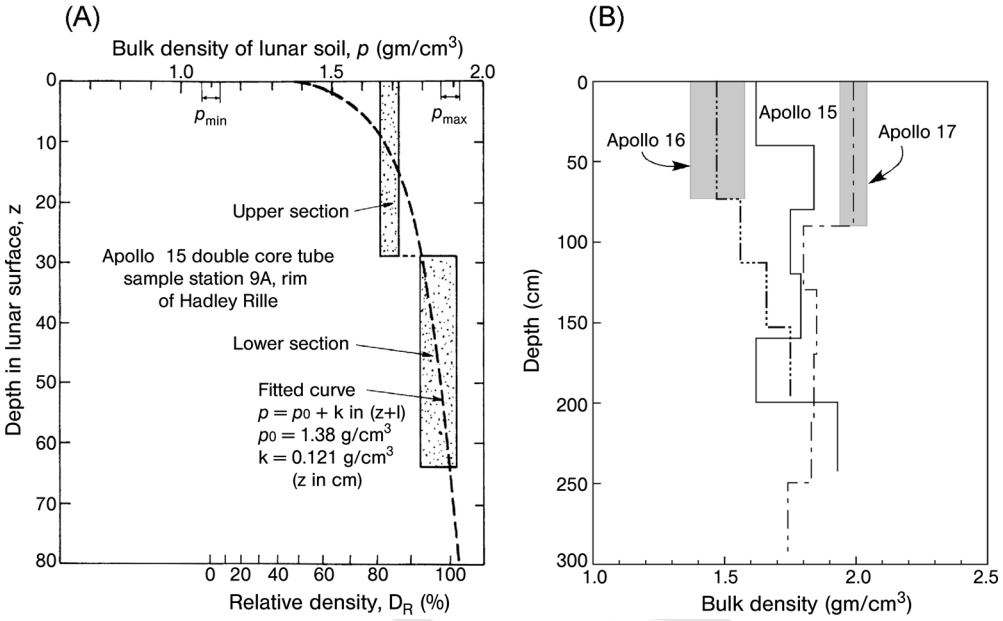

Figure 2.7 (a) Density versus depth plot for Apollo 15 drive core (samples 15 010, 15 011). Each core tube segment is 30 cm. Lower horizontal axis is relative density (0–100%). From Carrier, Mitchell and Mahmood (1973). (b) Bulk density versus depth in Apollo 15–17 drill cores. From Mitchell *et al.* (1974).

degree of compaction at depth necessitated a complete redesign of drill core collection methods used during the Apollo missions. Initially, core sampling was attempted with drive cores, which were hollow tubes physically hammered into place. Sample retrieval was difficult, and typical sample depths attained were <60 cm. Rotary drill cores were introduced in the Apollo 15 mission (Figure 2.8a), though again the high degree of compaction frustrated deep drilling. The joints between rotary drill sections were redesigned to accommodate a continuous auger (Figure 2.8b) on

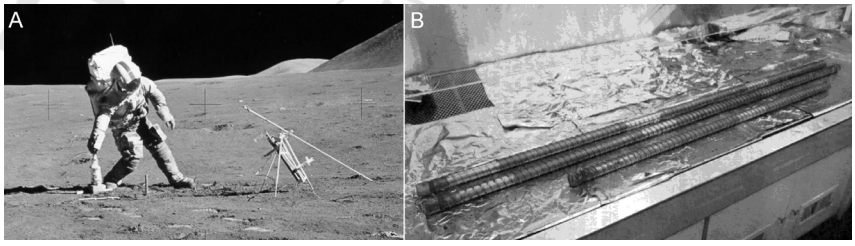

Figure 2.8 (a) Photograph of Apollo 15 Commander David Scott setting up a deep drill. NASA photograph AS15-87-11847. (b) Photograph of Apollo 17 deep drill core in the Lunar Receiving Laboratory clean bench, NASA Johnson Space Center. From Duke and Nagle (1974).

Apollo missions 16 and 17 (rather than a sectioned auger which prevented cuttings from escaping along the wall of the boring). In terms of bulk density, most cores average to $1.50 \pm 0.05\,\mathrm{g\,cm^{-3}}$ for the uppermost 15 cm, and the density generally increases to $1.74 \pm 0.05\,\mathrm{g\,cm^{-3}}$ for depths of 30–60 cm (Mitchell *et al.*, 1974). A few examples, such as the Apollo 17 deep drill core, do not follow this trend and instead possess a dense uppermost section (Figure 2.8b). This variability highlights the heterogeneous depositional histories of the lunar regolith.

The longest drill core, retrieved from a depth of about 305 cm (Carrier, 1974), was collected at the Apollo 17 site. Using a rotary drill coring tube (Figure 2.8b), this sample required a drilling time of less than 4 min and attained subsurface penetration speeds of between 40 and $80\,\mathrm{cm\,min^{-1}}$ (Mission Evaluation Team, 1973). Petrologic, geochemical, and textural analyses of the core revealed that it contains numerous layers and packets of layers that reflect a complex history of depositional and excavational impact events (e.g., Taylor, Warner and Keil, 1979; Vaniman *et al.*, 1979; Papike, Simon and Laul, 1982). An image mosaic of a portion of the core (post-sectioning) is given in Figure 2.9a. Several measured properties of the core

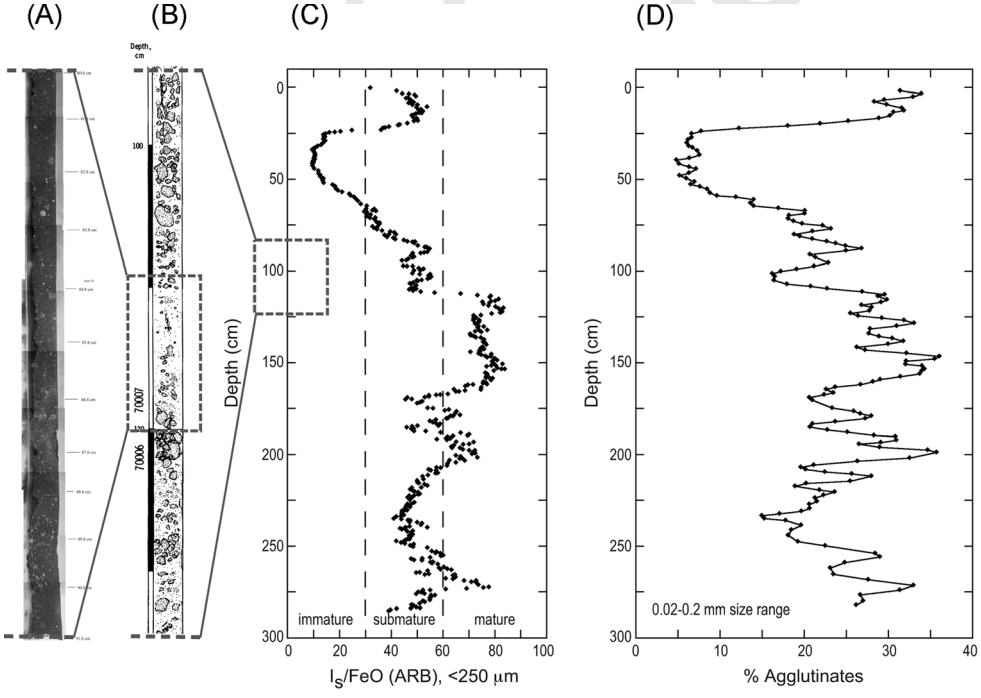

Figure 2.9 Data from Apollo 17 deep drill core (samples 70001–70009). (a) Mosaic of images of epoxy-encapsulated core segment (11 cm of lower portion of sample 70007; photograph courtesy C. Meyer, Johnson Space Center, 2008. (b) Portion of core sketch map based on X-radiography. Area given in (a) is outlined by dashed box [figure adapted from LSPET, 1973]. (c) Depth profiles of ferromagnetic resonance surface exposure (maturity) index I_s/FeO [from Morris *et al.*, 1979]. Area given in (b) is outlined by dashed box. (d) Agglutinate content along the Apollo 17 drill core [from Taylor *et al.*, 1979].

vary with regolith maturity, which is in turn a function of surface exposure time. For example, the intensity of the ferromagnetic resonance (I_s) is directly related to the abundance of extremely fine-grained metallic iron particles (FeO, typical diameter ~300 Å), which are a product of micrometeorite impacts and space weathering (e.g., Morris, Lauer and Gose, 1979). Agglutinates are also the product of surface exposure, and the abundance of agglutinates (Taylor, Warner and Keil, 1979) has a high degree of covariance with the maturity parameter I_s/FeO (Figure 2.9c and d).

The manual and powered drilling conducted by the Apollo astronauts and the robotic drilling conducted by the Luna spacecraft were ultimately successful, giving us a window into the third dimension, depth. The returned core samples also provide insight into the fourth dimension, time, since the regolith interacts with both the solar wind and cosmic rays in a depth-dependent manner. The experience gained during lunar surface drilling provides an invaluable guide for future drilling into planetary regolith environments, especially on atmosphereless bodies such as asteroids and the planet Mercury.

2.2.2.2 Mechanical Properties Inferred from Penetrometer Data

Although extraterrestrial drilling operations in excess of a few centimeters deep have yet to be conducted on bodies outside the Earth–Moon system, some inferences about the physical properties of surface materials relevant to drilling can be derived via indirect means. Perhaps the most basic physical property instrument is a surface penetrometer (e.g., Lorenz and Ball, 2001; Kömle, Kargl and Ball, 2001). The footpads of landed spacecraft can double as *de facto* penetrometers, and footpad penetration data have been returned from numerous successful soft landings. Examples include landed spacecraft on the Moon such as the Lunar Surveyor landers (Choate *et al.*, 1968), from the Luna landers and Lunokhod rovers (Cherkasov *et al.*, 1967; Kemurdzhian, Gromov and Shvarev, 1978), from the Apollo landers (Carrier, Olhoeft and Mendell, 1991), and on Mars from the Viking landers (Moore *et al.*, 1987). Other examples of penetrometers include the arm-mounted devices on the Venera landers on Venus (Surkov *et al.*, 1984), and a small piezoelectric sensor attached to the underside of the Huygens Probe on Titan, an icy moon of Saturn (Zarnecki *et al.*, 2005)

When landing on unconsolidated materials, penetrometers can provide information about the surface layer properties such as cohesion and internal angle of friction. Typical lunar regolith cohesions measured via footpad penetrations were found to be in the range 0.1–1.0 kPa, and the internal angles of friction ranged from 35 to 40° (Mitchell *et al.*, 1974). Given the heterogeneous nature of the lunar surface, however, it should be noted that measured values can vary greatly over short distances. On the Martian surface, several distinct types of soil-like materials were encountered with a range of strength parameters. Much of the regolith appears to be partially indurated, and disturbed indurated surfaces reveal millimeter- to centimeter-sized clods or aggregates of particles (dubbed "blocky material"). Blocky material compressed by the Viking 1 Lander footpad was found to have a cohesion in the range 5.5–7.1 kPa and an internal angle of friction around 30° (Moore *et al.*, 1987). Loose drift materials encountered by the footpads had a lower cohesion of 1.0–1.7 kPa and an angle of

internal friction of about 20°, although the properties of fine material are non-uniquely determined in footpad penetration data due to the possible presence of hard substrates or rocks buried at depth (Moore *et al.*, 1987).

Knowledge about the *in situ* surface properties of the planet Venus are derived chiefly from Soviet Venera and Vega landers. Venera 13 and 14 included ingenious penetrometers that consisted of a single-deployment arm mounted on the side of the spacecraft whose downward stroke served as a surface probe (Kemurdzhian, Gromov and Shvarev, 1978). Data returned from these instruments are consistent with surface material that has a load capacity of 26–100 kPa in the case of Venera 13 and 650–2500 kPa the case of Venera 14 (Surkov *et al.*, 1984). The former values are similar to those for terrestrial compacted sand, whereas the latter range is consistent with a volcanic tuff. Such low-strength materials indicate that even in a volcanism-dominated planet such as Venus, surface modification processes operate to form a thin regolith layer (Basilevsky *et al.*, 1985). Shallow (∼5 cm deep) surface drills were also employed by Venera 13 and 14 to retrieve rock and/or soil cuttings for geochemical analyses conducted within the protected body of the landers. Reported analysis of the drill telemetry indicates that depths of penetration and motor currents are consistent with weathered porous basalt or compacted ash material similar to volcanic tuff (Surkov *et al.*, 1984), although more detailed information about these shallow drill results are not available.

A surface penetrometer was also carried on the bottom of the Huygens probe (Figure 2.10a and b) that parachuted down through the thick atmosphere of the Saturian moon Titan. Titan's surface is composed of water-ice with a mean temperature less than 100 K. The Huygen's penetrometer consisted of piezoelectric sensor tipped with a small (1.6 cm diameter) hemispherical knob that extended beneath the spacecraft forebody (Zarnecki *et al.*, 2002). Analysis of the recorded force versus penetration distance reveals an initial spike, possibly due a fracture of a surface crust or small ice pebble, followed by a region near-constant force until the rest of the Huygens craft came in contact with the surface (Figure 2.10c). This plateau region (value near 50 N over the ∼2 cm projected surface area of the probe) yields a dynamic penetration resistance of 250 kPa, which is indicative of a weakly cohesive material consistent with lightly packed snow, wet sand or clay (Zarnecki *et al.*, 2005).

2.2.3 Influence Factors for Rock Mechanical Properties

It is well known rock properties vary with internal and external conditions. For example, there is generally a trend of increased rock strength with depth. However, it may be counteracted by local over-pressurization of the fluids, resulting in reduced effective stresses and therefore less intense diagenesis, by uplifting and subsequent erosion, or by other tectonic activities. In what follows, factors that influence the mechanical properties of rock are discussed. These factors could be classified into two groups: an intrinsic group such as grain size, cement type and contact pattern, *in situ* stress level, temperature, original cracks and fissures, and anisotropy, and a laboratory group such as specimen geometry, loading rate and coring method.

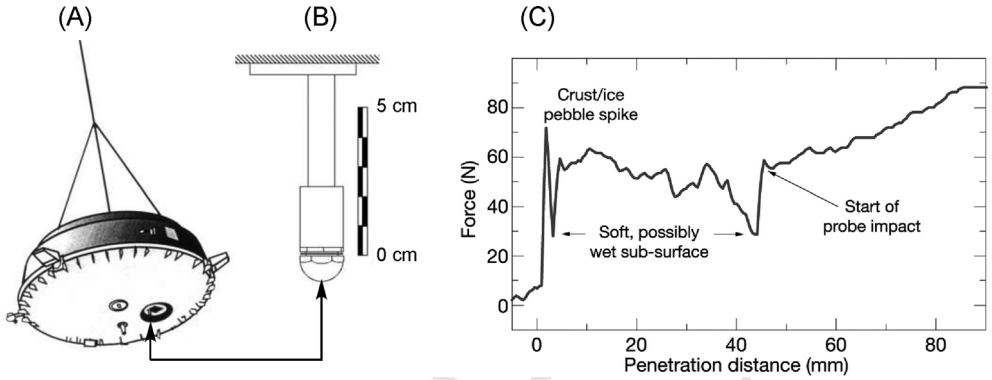

Figure 2.10 (a) Perspective diagram of the Huygens Probe in its descent configuration. Arrow points to the Surface Science Package (SSP), from which the penetrometer extends. From Lebreton and Matson (2002). (b) Diagram of penetrometer. From Zarnecki *et al.* (2002). (c) Recorded force versus penetration distance recorded by the Huygens' penetrometer. From Zarnecki *et al.* (2005).

2.2.3.1 Rock Lithology and Grain Size

Rocks with different lithologies have different properties and mechanical behaviors. Table 2.2 lists some properties from three rock categories, igneous, metamorphic, and sedimentary. Along with Table 2.1, it indicates that Young's modulus, rock rigidity (shear modulus), and strength of granite and siltstone are much higher than those of mudstone, claystone, sandstone, and chalk. For rocks from hydrocarbon formations, shale is often stronger than sandstone, whereas chalk from North Sea is relatively weak. Even though they are at large formed with the same mineral, quartz and quartzite are much stronger than sandstone, and limestone is usually stronger than chalk.

Different types of rocks have different grain sizes. In general, the grain size of salt is greater than that of granite, and diorite has larger grain size than does sandstone. Shale is the finest grained among the sedimentary rocks. For the sandstones from hydrocarbon formations, the grain diameter can easily be as large as 1 mm, or as fine as 0.1 mm. In fact, if the deposit bed is in a channel gravel, pebbles larger than 2–5 mm can dominate the grain size. In general, the porosity and permeability of sands increase with grain size, which may lead to lower strength. The grain size distribution may also influence rock strength because a wider distribution gives tighter packing of grains and hence more contact points between grains. A denser rock pack results in higher dilatancy, which resists shear distortion.

2.2.3.2 Cement Type and Contact Patterns

Cementation is another determinant factor affecting mechanical behavior of rock. Cemented sandstone is significantly stronger than uncemented sandstone. Also the "carboniferous" type is about twice as strong as the "shaly" form. Since the

Table 2.2 Engineering properties of intact rocks[a].

	Rock type	Location	γ (N m^{-3})	UCS (MPa)	ν_p (mm s^{-1})	ν	G ($\times 10^{10}$ Pa)	E ($\times 10^{10}$ Pa)
Igneous	Granite	Woodstock, MD	2650	251	4510		2.54	5.46
		Lithonia, GA	2640	193	2710	−0.19	1.18	1.91
Metamorphic	Quartzite, ferruginous	Urals, USSR	2650	374		0.13	3.08	7
	Gneiss, granite	Mineville, NY	2750	212	3630		1.96	3.85
Sedimentary	Dolomite, siliceous	Jefferson City, TN	2770	245	5180		3.19	7.52
	Dolomite: Niagara	Unknown, OH	2600	158		0.05	2.21	4.62
	Limestone	Barberton, OH	2690	197	4690		2.51	5.50
	Limestone	Ophir, UT	2780	193	5000	0.20	2.71	6.50
	Oil shale	Rio Blanco, CO	2044	82.8		0.33		
	Quartzite	Bergstrom, TX	2610	64.5			2.76	
	Salt, diamond crystal	Jefferson Island, LA	2163	21.4			0.49	
	Sandstone, cemented; Navajo	Huntington, UT	2880	124	2770	−0.07	0.945	1.75
	Sandstone, uncemented; Navajo	Huntington, UT	2130	55.9	2290	−0.05	0.586	1.12
	Sandstone, carboniferous	Woodrow, PA	2150	66.9	1800	0.01	0.352	0.69
	Sandstone, chaly; St Peter	Omaha, NB	2344	37.3		0.05		0.719
	Shale, quartzose; mauve	Lee's Ferry, AZ	2690	123		0.08		1.65
	Shale	Ophir, UT	2810	216	4540	0.09	2.66	5.82
	Shale, siliceous	OPhir, UT	2800	231	4940	0.12	3.05	6.81
	Siltstone, poorly cemented	Omaha, NB	2304	3.54		0.35		0.0125

[a]Symbols: surface tension (γ), compressive strength (σ_c), compressional velocity (ν_p), Poisson's ratio (ν), shear modulus (G), Young's modulus (E).
After Carmichael (1982).

cementation of most sandstones is to some extent a composite of different minerals, careful study should be carried on in order to understand better rock behavior as related to mineralogy.

Quartz overgrowth is a common cementing agent in sandstones. Quartz bonding between grains generally yields high strength, depending on the extent of the cementation and on its relative chemical stability. Carbonate cement can be relatively weaker than quartz cement and more reactive when contacted by unequilibrated brines. The absolute strength of carbonate-cemented sandstone, however, may be higher than that of a quartz-cemented type because of a higher contact area of cementing agents in the former. Also, under normal circumstance in sediments, carbonate can deposit much more rapidly than quartz because carbonate is far more soluble in water and can therefore be transported and precipitated faster.

Clay in sediments may appear different forms: if deposited after the sand matrix was formed, clay might not constitute part of load-bearing skeleton; if it forms as bridges between grains, it can take part in load bearing. In the latter case, the rock strength is expected to be relatively low because clay is not a strong cement and is generally sensitive to brines or geochemical changes.

Cementation texture or contact pattern mainly refers to the special arrangement of grains and cementing materials. Taylor (1950) considered two contact variations: the shape of the contact and the number of contacts per grain:

- There are five types of contact geometries, classified as tangential, long, concavo-convex, sutured, and floating (Figure 2.11). Usually long contacts are abundant and become more dominant with buried depth. Concavo-convex contacts are the next most popular and floating contacts are by no means uncommon.
- One grain is frequently surrounded by four others. The number of contacts shows an overall tendency to increase with depth, as porosity decreases.
- The cementation fabric also can give some hints about the rock deposit history. Ruistuen, Teufel and Rhett (1996) indicated that their studied sandstone had undergone considerable compaction because the grain-to-grain contacts among the particles are mainly long and concavo-convex, and extensive grain fracturing provides further evidence of compaction.

2.2.3.3 Stress Level

As rock is buried deeper, *in situ* stresses generally increase. An increasing confining stress has three effects: it increases rock compressive strength, reduces the brittle characteristics of the stress–strain curve, and decreases the tendency to dilate (Lee

Figure 2.11 Various contact patterns between rock particles.

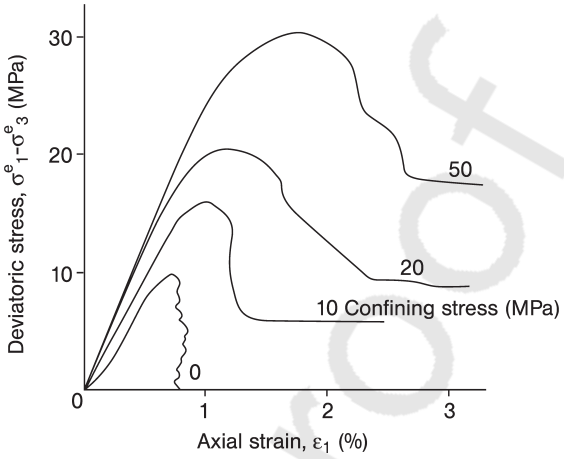

Figure 2.12 Triaxial compression tests with a sandstone at different confining stresses. After Santarelli and Brown (1987).

and Seed, 1967). In Figure 2.12, both rock modulus and strength increase significantly at higher confining stresses.

There are different empirical expressions for confining stress-dependent rock stiffness when rock behaves elastically. For example, one approach widely used in soil mechanics is (Duncan and Chang, 1970)

$$E_i = K_E P_a \left(\frac{\sigma_3'}{P_a}\right)^n \tag{2.30}$$

where K_E is a dimensionless parameter, representing the Young's modulus E_i at atmospheric pressure P_a, and n is the exponential rate of E_i change with confining stress σ_3'. This relationship implies that soil will lose its stiffness when the confining stress is zero. Rock, however, always retains some stiffness regardless of the level of confining stress before it is totally damaged (fragmented). Santarelli and Brown (1987) developed another empirical relation based on triaxial compression tests on carboniferous sandstones:

$$E_i = E_a\left(1 + m_E \sigma_3'^{n_E}\right) \tag{2.31}$$

where E_a is the Young's modulus of the rock at atmospheric pressure and m_E and n_E are constants determined from curve fitting.

The initial Poisson's ratio ν_i can be related to confining stress through a semi-logarithmic equation (Walsh and Brace, 1966):

$$\nu_i = \nu_a - D_\nu \log\left(\frac{\sigma_3'}{P_a}\right) \tag{2.32}$$

where ν_a is the Poisson's ratio of the rock at atmosphere pressure and D_ν is the rate of ν_i change with confining stress. This description implies that rock becomes less deformable when the confining stress increases.

It should be noted that the above descriptions only hold when rock behaves elastically. When rock starts to yield and accumulate non-reversible deformation, different correlations have been developed (Han *et al.*, 2004).

Duncan and Chang (1970) assumed that a typical triaxial stress–strain curve for sandstone fits a hyperbolic expression:

$$\sigma_1' - \sigma_3' = \frac{A_E \varepsilon}{1 + B_E \varepsilon} \tag{2.33}$$

where A_E and B_E are constants derived from curving fitting and their ratio A_E/B_E is the maximum stress the rock can sustain, and σ_1' is the maximum effective stress. They related Young's modulus E to shear stress using

$$E = \left[1 - \frac{R_f(1-\sin\varphi)(\sigma_1' - \sigma_3')}{2c_0\cos\varphi + 2\sigma_3'\sin\varphi}\right]^2 A_E \tag{2.34}$$

where c_0 is the rock cohesive strength, φ is friction angle, σ_1' is the effective maximum stress, and R_f is the failure ratio.

Similarly, Kulhawy and Duncan (1972) proposed the following equation for alteration of Poisson's ratio by shear damage:

$$\nu = \frac{A_\nu}{(1 - B_\nu \varepsilon_1)^2} \tag{2.35}$$

where A_ν and B_ν are constants of a hyperbolic strain relationship and the strain ε_1 in the direction of maximum effective stress (σ_1') can be expressed as

$$\varepsilon_1 = \frac{\sigma_1' - \sigma_3'}{A_E\left[1 - \dfrac{R_f(1-\sin\varphi)(\sigma_1' - \sigma_3')}{2c_0\cos\varphi + 2\sigma_3'\sin\varphi}\right]^2} \tag{2.36}$$

This expression indicates that Poisson's ratio increases with shear stress, and it increases faster if rock is more damaged. In other words, the rock becomes more deformable when microfractures are developed and plastic effects accumulate.

Other rock properties such as friction angle (φ) and bulk modulus (K) have been studied and their relations with confining stress are expressed in the following form (Byrne, Cheung and Yan, 1987):

$$\varphi = \varphi_0 - D_\varphi \log\left(\frac{\sigma_3'}{P_a}\right) \tag{2.37}$$

and

$$K = K_B P_a \left(\frac{\sigma_3'}{P_a}\right)^n \tag{2.38}$$

where φ_0 is friction angle at atmosphere pressure, D_φ is the rate of change of φ with confining stress, and K_B and n are constants derived from curve-fitting.

Even though the above correlations have been confirmed in the laboratory, they may not hold when other influence factors become dominant. For example, Poisson's ratio is affected by stress level, fissures, temperature, rate of loading, and so on. The

presence of fissures and pores decreases the Poisson's ratio of rock, but when fissures have a strong fabric and are oriented along the direction of applied stress, they may open up substantially with increasing axial compressive stress and lead to a large Poisson's ratio. An increase in effective confining stress lowers Poisson's ratio for weaker rocks, but for stronger rocks it may not have any influence (Lama and Vutukuri, 1978).

2.2.3.4 **Loading Rate**

Loading rate refers to the rate of strain change or the rate of stress change, which can be related to each other through stress rate = strain rate × Young's modulus, assuming that the rock behaves elastically under uniaxial loading conditions. Most rock testing is carried out at a strain rate of the order of 10^{-3}–$10^{-4}\,s^{-1}$. The influence of loading rate on rocks is different depending on the rock type. For sandstone, an increase in Young's modulus by 50% has been reported when the loading rate was increased from 0.18 to $0.70\,MPa\,s^{-1}$ (Phillips, 1948). Tests conducted on Berea sandstone, Barre granite, Tennessee marble, and Valder limestone showed that there is an increase in modulus with strain rate, ranging from 2.2×10^{-4} to $2.2 \times 10^{-8}\,s^{-1}$, except that the modulus of Valder limestone remains almost constant (Peng, 1975). The strain at failure increases for increased strain rate as rock strength increases. Results from norite, dolerite, Carrara marble and strong sandstone, however, show no marked effect of strain rate when it ranges from 10×10^{-3} to $10 \times 10^{-5}\,s^{-1}$ (John, 1972). For quartzite and weaker sandstone, the modulus of deformation increased slightly with increase in stress rate. Lama and Vutukuri (1978) summarized, "... it looks that homogeneous strong low porosity rocks showing linear elastic behavior will not be affected by increase in rate of loading, while for the others the modulus value will increase."

2.2.3.5 **Anisotropy**

The anisotropy of rock properties can be significant. In Tronvoll and Fjær's experiments, Young's modulus, compressive strength and tensile strength were more than twice as large in the parallel-to-laminae direction compared with those in the perpendicular direction (Tronvoll and Fjær, 1993). Also, the permeabilities tested by Holt (1990) could be as high as 1.5 darcy in the parallel direction, whereas in the perpendicular direction values of only 0.1–0.5 darcy were found. The main reason for the anisotropy is the stress levels at which rock forms and the origin fabric of the sediments after vertical compaction. Since the direction perpendicular to horizontal laminae tends to be the one of maximum principal stress, the grains have suffered more compaction in the vertical direction. As a consequence, there are more long and concavo-convex contacts deposited vertically, which leads to a preferred direction for rock to exhibit stronger and stiffer mechanical response.

On the other hand, the long axis of a grain is more likely deposited in the direction parallel with laminae, resulting in a higher cross-sectional area for fluid flow and higher permeability along the direction. Kohata *et al.* (1997) tested several sands and gravels, and confirmed that the elastic deformation moduli of the granular materials became more anisotropic at higher anisotropic stress (i.e., higher ratio of vertical

stress to horizontal stress). Further, when granular rock is more homogeneous, there is less modulus difference in the vertical and horizontal directions, which could possibly be evidence for a long-axis influence. This shows the influence of rock fabric at the microscopic scale on rock behavior.

In addition to microscopic anisotropy discussed above, the anisotropy due to secondary rock characteristics such as degree of weathering and presence of joints or fractures also plays an important role in rock mechanical response upon loading. For example, rock mechanical and conductivity properties in carbonate formations may be determined more by the number, distribution, and characteristics of fractures than the rock matrix itself. A reliable description of this type of anisotropy poses a more significant challenge as the rock samples in the laboratory may not represent *in situ* fracture conditions.

2.2.3.6 Humidity or Fluid Saturation

The deterioration of rock properties by adsorption (when liquid accumulates on the surface of a solid forming a thin film of molecules) or absorption (when a liquid diffuses into a solid to form a solution) is sometimes referred to as the Rehbinder effect; in 1944, Rehbinder led an extensive study into the hardness-reducing effects of surfactants (surface-active agents). Because most rocks are water-wet, that is, water tends to attach to the rock surface more easily than non-wetting fluids such as oil or gas, the effect of fluid saturation is also studied in addition to that of water saturation, moisture content, humidity, and so on. Many experiments have been carried out, and in summary, the results have indicated that:

- For all rock samples, strength is generally found to decrease with increase in water saturation. This includes rock tensile strength, compressive strength, and UCS. The strength decrease has been reported to range from 8% (Hawkins and McConnell, 1992) to 98% (Priest and Selvakumar, 1982), depending on the rock texture, mineralogy and fluid chemistry. Most of the strength decrease occurs after only a slight increase in water saturation or moisture content from the dry state (Mellor, 1971; West, 1994). Further increases in moisture content have little effect on rock strength and elastic properties.
- The value of the friction coefficient appears to remain unaltered in many cases (Colback and Wiid, 1965).
- Young's modulus decreases with increase in water saturation, sharing the same trend as rock strength (Burshtein, 1969; Gregory, 1976; Rao, Rao and Ramamurthy, 1987).
- The behavior of Poisson's ratio is complicated; it may increase or decrease slightly before a general increase takes place at higher saturations (Hawkins and McConnell, 1992), or remain constant (Papamichos, Brignoli and Santarelli, 1997).

There are several possible reasons that may account for rock weakening due to fluid moisture or saturation changes (Han and Dusseault, 2002), including chemical reactions, capillary strength, and shale swelling.

2.2.3.6.1 **Chemical Reactions between Water and Rock Solids** Water could react with various rock minerals. For example, quartz is the most common mineral in sand, and SiO_2 overgrowths are also common as cementation. Quartz hydrolysis is believed to reduce surface energy and cohesion (Swolfs, 1971). The common mode of hydrolysis is

$$Si - O - Si + H_2O \rightarrow Si - OH \cdot HO - Si$$

The Si−O−Si bonds break up to give two silanol groups: Si−OH and HO−Si. In such a hydrolyzed bridge, the hydrogen bonds are weaker by an order of magnitude than the silicon–oxygen bonds. Since all silicates have Si−O−Si or Si−O−M bridges (where M is a metal ion) that are susceptible to this type of hydrolysis, this water weakening may apply to silicates in general, for example, feldspar, olivine, hypersthene, tourmaline and beryl (Griggs, 1967). However, the occurrence of hydrolysis depends closely on the temperature. The fact that quartz is strong below the critical temperature motivated Griggs and Blacic (1965) to propose another model of hydrolysis, based on the assumption that "... the easy glide which occurs in the hydrolytic state can only occur when the hydrolyzed dislocation can move by exchanging hydrogen bonds with a neighboring silicon–oxygen bridge which has become hydrolyzed" (Figure 2.13).

For calcareous cementitious rocks, the possible reactions with water are carbonate dissolution:

$$CaCO_3 + H^+ \rightleftharpoons Ca^{2+} + HCO_3^-$$

where H^+ may originate from

$$H_2O + CO_2 \rightleftharpoons H_2CO_3$$

$$H_2CO_3 \rightleftharpoons HCO_3^- + H^+$$

$$HCO_3^- \rightleftharpoons H^+ + CO_3^{2-}$$

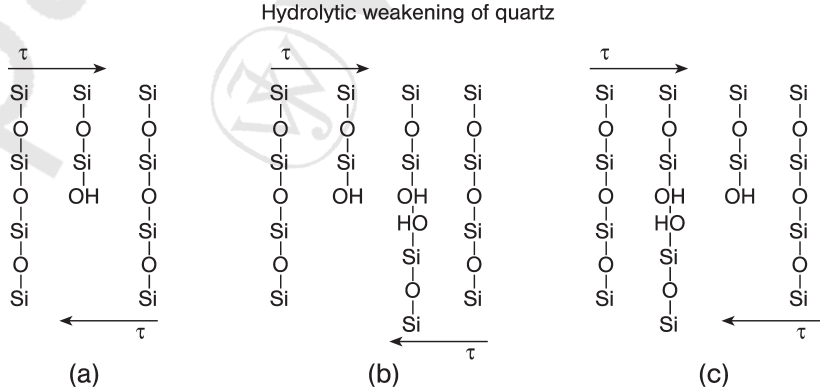

Figure 2.13 Frank–Griggs model of hydrolysis (Griggs and Blacic, 1965).

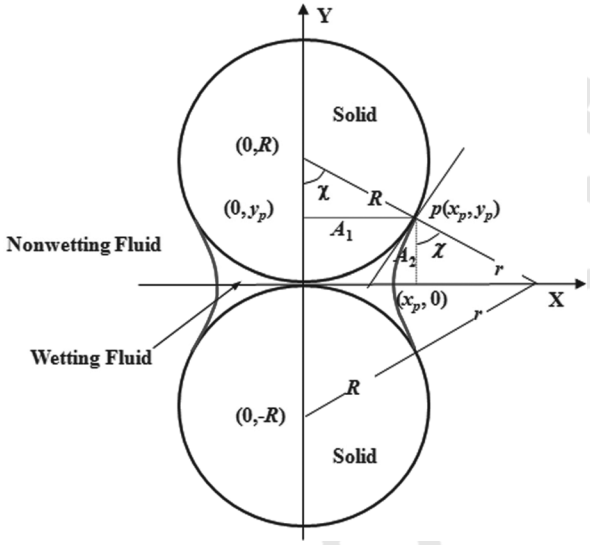

Figure 2.14 A microscopic model for capillary strength (Han, Dusseault and Cook, 2002). (Please find a color version of this figure on the color Plates).

In the normal pH range of formation water (e.g., pH = 5–8), dissolved iron is present as Fe^{2+} whereas Fe^{3+} is insoluble. Therefore, ferruginous cement will most likely be stable as formation water comes in, whereas for the formation water itself, since ferric ions commonly exist, the chemical reaction may occur as

$$Fe^{2+} + 3H_2O \rightleftharpoons Fe(OH)_3 + 3H^+ + e^-$$

that is, there may be some Fe^{3+} deposition in the rock pore system.

2.2.3.6.2 **Changes of Surface Tension and Capillary Force** Assuming that rock particles have the same size and contact tangentially, with a zero contact angle between fluid and particles (Figure 2.14), Han, Dusseault and Cook (2002) proposed a model to quantify rock strength changes with fluid saturation. Rock capillary tensile strength (σ_T) could be expressed as

$$\sigma_T = \lambda \frac{1-\phi}{\phi} \frac{F_c}{4R^2} \tag{2.39}$$

where R is the radius of the spherical rock particles, ϕ is porosity, and λ is a factor accounting for nonuniform particle size effects on total rock strength. A value of $\lambda = 6$–8 is suggested for packs of particles with a narrow size range and 1.9–14.5 for packs with wider particle size distributions (Schubert, 1984). For UCS,

$$\mathrm{UCS} = \lambda \frac{1-\phi}{\phi} \frac{\sin\varphi}{1-\sin\varphi} \frac{F_c}{2R^2} \tag{2.40}$$

which illustrates that, for loosely compacted rock, rock capillary strength is related to porosity, friction angle, capillary force, particle radius, and particle size distribution.

The pressure difference method is applied to calculate the capillary cohesive force resulting from capillary pressure (P_c):

$$F_c = \pi x_p^2 P_c \tag{2.41}$$

assuming that the shape of the liquid bridge between grains is a toroid characterized by radii r and x_p. Then, capillary pressure across the liquid bridge can be calculated by

$$P_c = \gamma\left(\frac{1}{x_p} - \frac{1}{r}\right) \tag{2.42}$$

Figure 2.15 plots various rock capillary strengths, such as UCS, tensile strength, and cohesive strength, and capillary force versus fluid saturation. Compared with the rapid decrease in capillary pressure with water saturation, the decline rates of capillary force and strengths with saturation are much slower. When the particle radius is 0.1 mm and the fluid surface tension is 0.036 N m^{-1}, the maximum capillary strength can be as high as 20 kPa, whereas all capillary variables become zero around a saturation value of 0.34. However, there is a small section of the relationship at fluid saturation approaching zero where a short increase in strength is predicted, because some volume of water is needed to build a stable liquid bridge between particles.

2.2.3.6.3 **Swelling and Disintegration of Shale** Clay behavior is very complicated and controversial. Generally, clay tends to precipitate authigenically in the voids among rock particles rather than at the contacts; therefore, it carries little direct stress and does not directly contribute to the decrease in rock strength. However, when in contact with different water chemistry, the swelling behavior of smectic clay (even in small fractions of the rock) may greatly affect rock stability. The swelling clay volume decreases the rock permeability, which increases the local pressure, which can cause increased fluid drag forces.

In many cases, several mechanisms may function simultaneously in a destabilizing direction. But is this effect important for extraterrestrial drilling? The short answer is yes. Imagine, for example, drilling deep holes on a planet or a moon with highly abundant water-ice formations (e.g., Mars or Jupiter's moon, Europa). It is highly probable that heat generated by the drilling action could sufficiently warm up the water–ice bound formations to in fact melt the ice at the bottom of the borehole. Disregarding the dangers of this situation (thawed water-ice could refreeze on to the drill and the surrounding borehole walls and trap the drill inside a hole for ever), it is very likely that liquid water could in fact make the rock ahead of the drill bit weaker and in turn easier to drill. This effect may be present on extraterrestrial bodies that have no atmosphere (i.e., vacuum), as is the case on the Moon, or have a very low atmosphere, with pressures below the triple point of water, as is the case with the Martian South Polar Region. Having an atmospheric pressure below the triple point of water, at 6.1 mbar, ensures that no liquid water can be present for an extended period of time. However, water-ice may still be present, but as soon as the ice temperature reaches zero, the ice will sublime directly to water vapor and will not go through the liquid state as is the case on Earth. However, in deep holes where drilled cuttings could accumulate around the drill, sealing the bottom of the hole from the

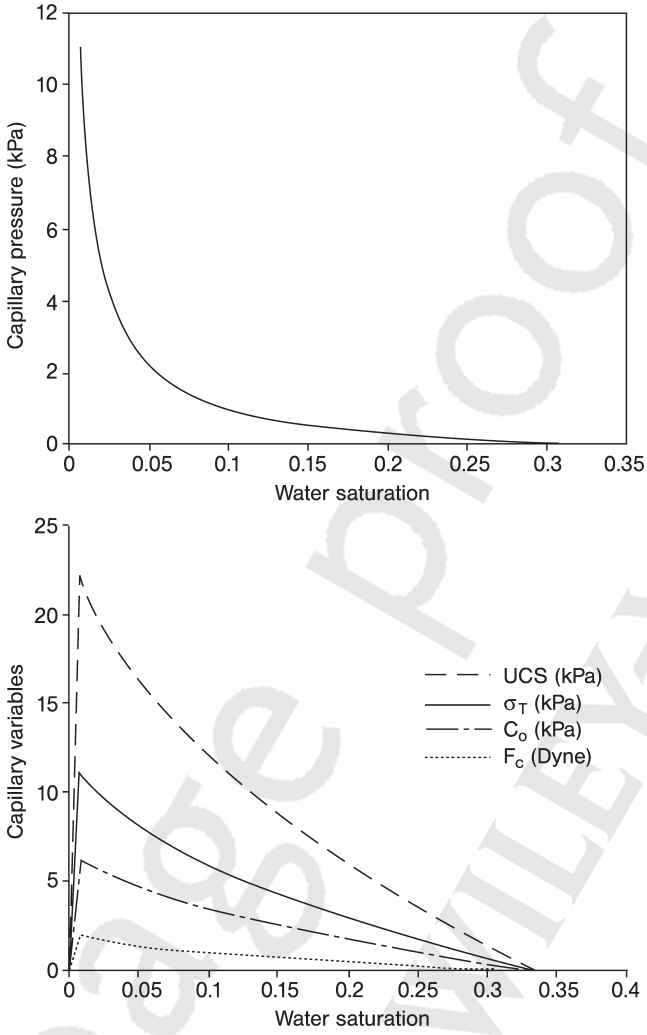

Figure 2.15 Variations of capillary pressure, force, and strengths with water saturation (Han and Dusseault, 2005).

outside atmosphere, a local atmospheric pressure in the lower part of the hole may in fact reach pressures above the triple point of water when enough ice sublimes to vapor (in this case, the partial pressure of sublimed water vapor will in fact be the same as the total atmospheric pressure).

2.2.3.7 **Temperature**

Another parameter that affects rock strength is temperature. On Earth, because of geothermal gradients, rocks lying deeper underground are hotter. Very high temperatures combined with high overburden pressure make rock more plastic and in turn more difficult to excavate. This was found, for example, by Soviet scientists and

engineers working at the Kola Superdeep Borehole project. They found that at a depth of 12 262 m the temperature was 180 °C instead of the expected 100 °C, and at these high temperatures drilling deeper was found to be infeasible with the then current state of drilling technology.

High-temperature drilling will also have to be dealt with on two planets in our Solar System: Venus and Mercury. The surface temperature of Venus is in the region of 460 °C, whereas that on Mercury ranges from −180 °C just before sunrise to 427 °C in the early afternoon (Watters, 1995). This large thermal fluctuation is due to the rotation of Mercury and a lack of atmosphere that has a tendency to trap the heat. The high surface temperature on Venus, on the other hand, is due to its very dense carbon dioxide atmosphere that traps most of the heat. On both Mercury and Venus the temperature is so high that zinc and tin, for example, would melt.

Unlike the challenges of high temperature (which make a rock more plastic) and very high overburden pressures (which make a rock stronger) that are pertinent to Earth, the challenges of drilling on most extraterrestrial bodies (except for Mercury and Venus) arise from having to deal with rocks at extremely low temperatures. For example, the temperature on Mars can be as low as −140 °C and in the lunar polar craters even as low as −230 °C. The average temperature on the surface of a typical asteroid is approximately −70 °C, on the comet Tempel 1 the temperature varies from −113 °C in shadow to −44 °C at the point directly below the sun (Tempel 1 website, 2008).

Unlike high temperatures, which make rocks more plastic, low temperatures make rock much harder and in turn much more difficult to drill. Much research has been conducted over the last century to determine the effect of low temperature and variable moisture content on the strength of different rocks. In particular, Mellor (1971) performed a very comprehensive study, during which he investigating the strength of sandstone (Berea Sandstone), limestone (Indiana limestone), and granite (Barre granite) at temperatures ranging from +23 to −195 °C and at moisture contents ranging from zero (over dried rocks) to full saturation.

The major effect of rock strengthening at low temperatures occurs when rocks have a significant amount of water. It was observed by Mellor (1971) that as the temperature of a rock decreases, its strength gradually increases and it reaches the limit at around −120 °C. At this temperature, the compressive and tensile strengths of Berea sandstone, Indiana limestone and Barre granite are higher than the room temperature values by factors of around 5, 4 and 2, respectively (see Figure 2.16). However, Mellor also observed that with a further decrease in temperature to −196 °C, the strength of the rocks in fact dropped.

Mellor explained the rock strengthening effect as follows: as the temperature dropped, water began to freeze in the largest pores, and progressively started to freeze also in smaller pores. This freezing effect of water in pore spaces had an effect of plugging cracks and pores in the rock and in turn increasing the rock strength, since now far fewer cracks were present. However, as the temperature was reduced to below a certain value, the differential coefficient of thermal expansion caused a differential strain between the rock and the ice matrix, which resulted in weakening of the rock.

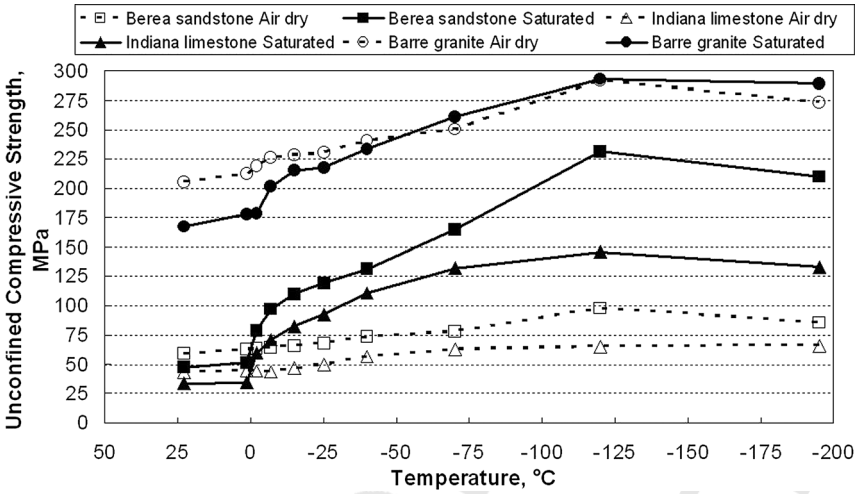

Figure 2.16 Effect of temperature on uniaxial compressive strength for the "air-dry" and saturated sandstone, limestone, and granite. After Mellor (1971).

Heins and Friz (1967) also found that the strength of oven-dried basalt rock increased by 50% when cooled to −196 °C. This temperature dependence on the strength of basalt was confirmed by Zacny and Cooper (2007). In particular, they found that the strength of basalt increased from 256 MPa at + 100 °C to 310 MPa at −100 °C, i.e., by 20%. The reason why the strength of basalt was not as pronounced as the strength of sandstone or limestone was that basalt, having much lower porosity and permeability, has intrinsically lower saturation levels.

2.3 Stresses and Energy in Drilling

2.3.1 Stress in Sedimentary Basins

2.3.1.1 Definitions, Total and Effective Stresses

Stress cannot be measured directly, only inferred from other measurements (pressure, displacements, tectonic data, geological history, . . .). Stresses are carried by the solid material and the liquid; herein, "pressure" refers only to the compressive potential in a fluid.

Stress state in rock mechanics is defined in terms of principal compressive stresses and their orientations (Figure 2.17) acting at a single point:

- Three principal stress magnitudes acting normal to the principal planes, σ_1, σ_2, and σ_3, indicate major, intermediate and minor principal compressive stresses (compression positive).

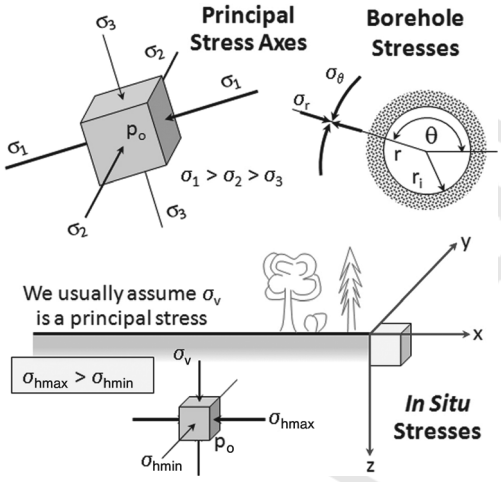

Figure 2.17 Some stress definitions commonly used in petroleum geomechanics. (Please find a color version of this figure on the color Plates).

- Three mutually perpendicular principal stress orientations, each corresponding to a principal stress direction, usually stipulated by direction cosines in a Cartesian reference frame.
- A single value for the pore pressure, p_0.

The first six define a symmetrical second-order tensor; the pore pressure is a scalar, independent of direction. With these seven independent values, stresses along and across any plane passing through the point can be computed. Further definitions and equations for stress transformations and calculations may be found in continuum mechanics texts (e.g., Beer, Johnston and deWolf, 2005).

Only exceptionally is it possible to define fully the stress state *in situ*; generally, assumptions must be made. In sedimentary basins, it is assumed that the vertical stress, σ_v, is a principal stress (either σ_1, σ_2 or σ_3); so that the other two orthogonal principal stresses are parallel to the Earth's surface. The two horizontal principal stresses are the maximum and minimum principal horizontal stresses, $\sigma_{h\,\max}$ and $\sigma_{h\min}$. In petroleum geomechanics, it is the convention to report principal stresses as total stresses, along with the pore pressure as an independent value.

In Cartesian coordinates, the Terzaghi principle of effective stress is defined as follows:

$$\begin{bmatrix} \sigma'_x & \tau_{xy} & \tau_{xz} \\ \tau_{yx} & \sigma'_y & \tau_{yz} \\ \tau_{zx} & \tau_{zy} & \sigma'_z \end{bmatrix} = \begin{bmatrix} \sigma_x & \tau_{xy} & \tau_{xz} \\ \tau_{yx} & \sigma_y & \tau_{yz} \\ \tau_{zx} & \tau_{zy} & \sigma_z \end{bmatrix} - \begin{bmatrix} p & 0 & 0 \\ 0 & p & 0 \\ 0 & 0 & p \end{bmatrix} \tag{2.43}$$

where σ is total normal stress, σ' is effective normal stresses, τ is shear stress, p is pore pressure, and x, y, z are the three coordinates. The above equation expresses the principle that effective stresses are the difference between total stresses in the rock skeleton and pore pressure in the interconnected voids. Principal effective and total

stresses are always co-axial because p is a scalar. Further, because pore pressure always acts normal to the surface of rock particles as a hydrostatic force, it contributes nothing to the shear stress that acts parallel to a plane.

The concept of effective stress lays the foundation for rock stability investigations in fluid-saturated underground conditions because it is effective stresses that act on the rock particles to stabilize or mobilize them.

In petroleum geomechanics, the form $\sigma' = \sigma - \alpha P$ has generally been used, where α is Biot's poroelastic constant. Physically it means that the rock skeleton carries the part σ' of the total external stress σ, while the remaining part, αP, is carried by the fluid in the porous medium. Expressed as $\alpha = 1 - (C_m / C_b)$, where C_m and C_b are the compressibilities of rock matrix and rock bulk, respectively, α is difficult to measure, given the inherently complex nature of a porous medium. However, α is restricted to the region $\phi < \alpha \leq 1$, and for unconsolidated or weak rocks, α is close to 1 (Fjær *et al.*, 1992).

2.3.1.2 Stress Boundary Conditions

All geomechanics problems, including drilling analysis, take the *in situ* stress state as the point of departure; the same is true for drilling; the *in situ* (far-field) stresses and pore pressures constitute the boundary conditions for analysis. *In situ* stresses are predicated by tectonic, diagenetic, and burial depth issues; these act at scales of 1–100 km. Stresses, σ, pressure and temperature, p_0 and T_0, and even the pore water chemistry, C_i, are altered by the drilling process in a zone perhaps 5–10 times the borehole diameter (Figure 2.18). A drill bit is 100–500 mm in diameter, so this zone is on the order of several meters; however, where the cutting tool tip acts on the rock, the relevant scale is perhaps 1–10 cm. Clearly, understanding stresses and stress changes at all scales is vital for drilling and borehole stability analyses.

In altered conditions, such as drilling through depleted reservoirs and zones where cold or hot fluids have been injected, or in side-tracking a new borehole from an existing cased hole, some form of mathematical modeling is needed to calculate the

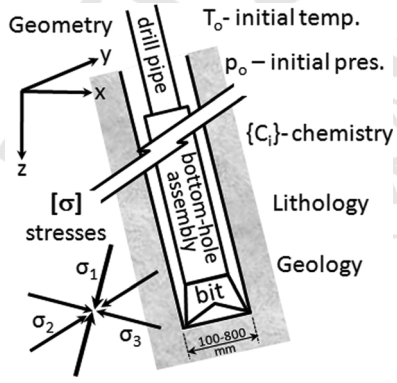

Figure 2.18 Initial conditions in drilling. All these factors change with depth, and many mechanical properties (strength, stiffness) are anisotropic. Furthermore, there are discontinuities such as joints, bedding planes, and faults.

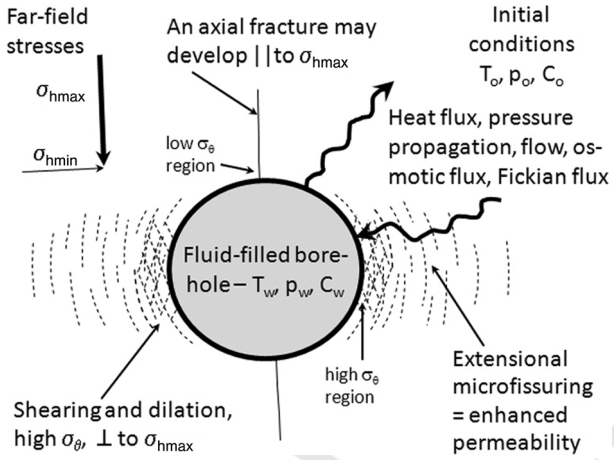

Figure 2.19 Diffusion processes near a borehole are coupled with the thermal effects, the chemical effects, and the mechanical effects.

stresses in these changed conditions. Again, initial stress and pressure fields serve as the point of departure.

Effective stresses near the drill bit are changed by fluid pressure and stress relief. Drilling fluid density, borehole wall filter cake properties, and the transport characteristics of the rock mass also affect stresses over time because of diffusion processes. In shales, pore fluid and mud filtrate chemistry, combined with Darcian and Fickian diffusion processes (Δp–flow, osmotic suction, concentration gradient-driven flux), can lead to volume changes (ΔV), which in turn alter the stresses (Figure 2.19) and perhaps affect the permeability. The drilling fluid is cooler than the rock at the bit (ΔT), leading to transient thermoelastic stress changes, in addition to changing the rate of diffusion because fluid viscosities change with temperature and diffusion processes are kinetically activated. Finally, the bit and drill string apply a normal and shear load to the rock face through the tool contact. These processes affect physical parameters such as permeability; hence rigorous analysis of rock stresses in drilling is a fully coupled thermal–hydraulic–mechanical–chemical problem. In the elastic behavior range, at least a Biot formulation is required (e.g., Wang and Dusseault, 2003), and generally effects of elastic non-linearity, plasticity, and rupture will arise. Clearly, constitutive behavior is also a vital aspect of analysis in geomechanics.

In virgin conditions, far-field stresses apply, but in depleted reservoirs and ΔT processes, stresses have been altered, perhaps massively: the stress fields have changed, and principal stress directions have rotated. Altered stress conditions are case specific, and must be measured or computed from initial conditions, constitutive laws, and boundary conditions. The subject of this section is the estimation of far-field stresses, which are the point of departure for drilling planning and analysis. Far-field stresses also impact issues such as hydraulic fracture behavior, casing shear, fractured carbonate production behavior, and so on.

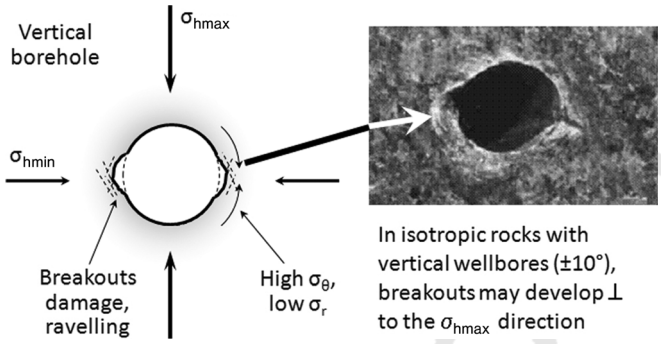

Figure 2.20 Borehole breakouts arise from yield of rock in the direction normal to $\sigma_{h\,max}$. Photograph courtesy Bezalel Haimson.

2.3.1.3 Stress Orientations

The orientations of the two horizontal principal stresses may be determined by various means. Common methods are briefly introduced and discussed here.

Borehole breakouts are spalls which develop on opposing sides of the borehole during drilling. In near-vertical holes ($\pm 10^\circ$), breakouts are oriented perpendicular to $\sigma_{h\,max}$ (Figure 2.20). Breakouts are analyzed with a set of quality control criteria; poor data are rejected and good data ranked according to quality (Zoback, 2007). Some of the factors to be considered are:

- Is the well within 10° of vertical? ($<5^\circ$ is better).
- Is the breakout occurring over a long interval?
- Are there other consistent breakouts above and below?
- Is the breakout actually hole enlargement, a wash-out, a key-seat?
- Are strata anisotropic and inclined, leading to spurious orientations?
- Is the breakout in a lithologically consistent zone?
- Do the data make sense overall, regionally and with offset wells?

Boreholes commonly display extensional fractures in the wall, arising because of wellbore damage combined with pressures from the mud, particularly repeated surge pressures during trips and connections. If the well is near-vertical, these show up clearly on geophysical logs as fine vertical cracks, sometimes continuous over substantial lengths (Figure 2.21). They are easily differentiated from natural fractures that have sinusoidal wall traces, and from the dark black breakouts which are, as expected, at 90° to the extensional fractures. Because extensional fractures will open normal to $\sigma_{h\,min}$, they can be used, along with the log azimuth data, to give the direction of the two horizontal stresses. If the well is inclined somewhat, these extensional fractures will appear "*en echelon*" in the wall, but the direction may still be reasonably estimated. Care has to be taken that the inclined well has not caused a large rotation of the principal stresses in the well vicinity, giving spurious induced fracture orientations, so quality control criteria similar to those used in breakout analysis are used.

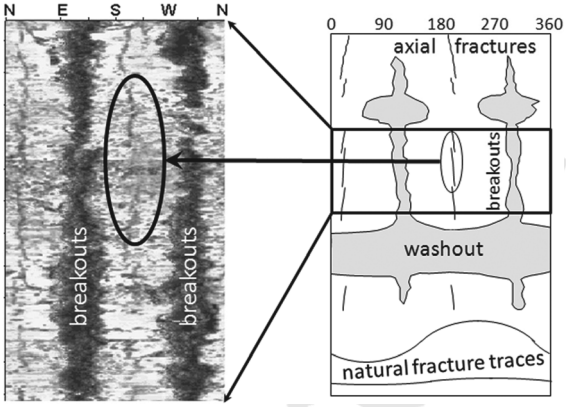

Figure 2.21 Use of borehole wall imaging methods to determine stress orientations. Here, a formation micro-resistivity imaging log is used to identify breakouts and fractures. (Please find a color version of this figure on the color Plates).

In an anisotropic stress field, the borehole will usually experience anisotropic wall damage, even if no breakouts or axial extension fractures are present. Microfissuring normal to $\sigma_{h\max}$ dominates, as with breakouts. It is likely that the filtrate has penetrated more deeply in the damaged region, giving an anisotropic resistivity response (Figure 2.22). This may be detectable on four-arm or multi-sensor resistivity meters, particularly for focused logs that measure resistivity at different wall depths, particularly in the range 10–50% of the borehole radius. As always, quality control is necessary.

Core measurements have been widely used (and often abused) to assess stress orientations. All methods take advantage of anisotropic behavior of some kind, and several common approaches are discussed briefly here.

When a homogeneous rock is cored and brought to surface, it displays a small, slow expansion for some time (days). If a fresh piece of core is mounted in a precision

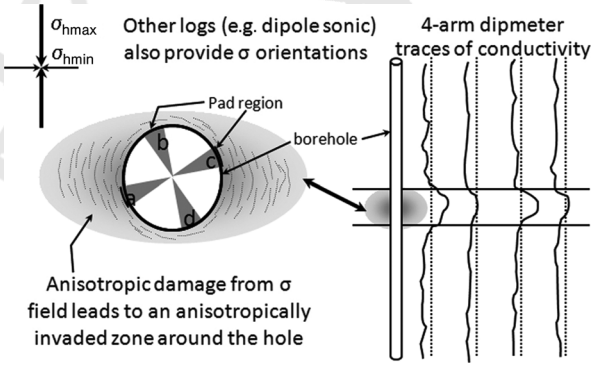

Figure 2.22 Here, induced resistivity anisotropy arising from anisotropic fluid invasion gives information about stress orientations.

measuring device, isolated from further temperature or moisture changes, and the time-dependent diameter changes are measured in several directions; the maximum strain recovery can then be related to the direction of $\sigma_{h\max}$. Assuming the orientation of the core is known, *in situ* stress directions may be inferred. This method is known as differential anelastic strain recovery (Ren and Roegiers, 1983). Rock anisotropy can confound this process, and it is best to test several specimens simultaneously to assure a consistent response.

Any piece of competent oriented core can be tested for radial variations in various properties. Core can be oriented by scribing during entry to the barrel, or by alignment with borehole wall log or image data. If the rock has a distinctly oriented microfissure fabric, it may reflect the stress field anisotropy, assuming that the anisotropy is directly related to the present stress field, not a paleo-stress field or inherent rock anisotropy. Among properties that may be used are differences in strain response, thermal expansion behavior and acoustic emissions (Villaescusa, Seto and Baird, 2002).

If old, unoriented core is all that is available, it is usually possible to obtain good core orientation ($\pm 5^\circ$ in azimuth) using paleomagnetic signatures, combined with the geological age of the specimen. Magnetic particles sedimented along with the rock matrix aligned themselves in the Earth's magnetic field at that time, and this "signature" is preserved permanently. Once the natural magnetization vector has been quantified, it can be corrected for magnetic North Pole direction at the time the sediment was laid down. Polar orientations over geological time are widely known from continental drift studies of polar wandering. After the core is oriented, other properties may be used to infer stress orientations.

Geological inference is a powerful means of assessing stress directions (Pollard and Fletcher, 2005). Generally, near faults, mountain chains, grabens (rifts), and so on, stresses reflect the geometry of the geological structures (Figure 2.23). For

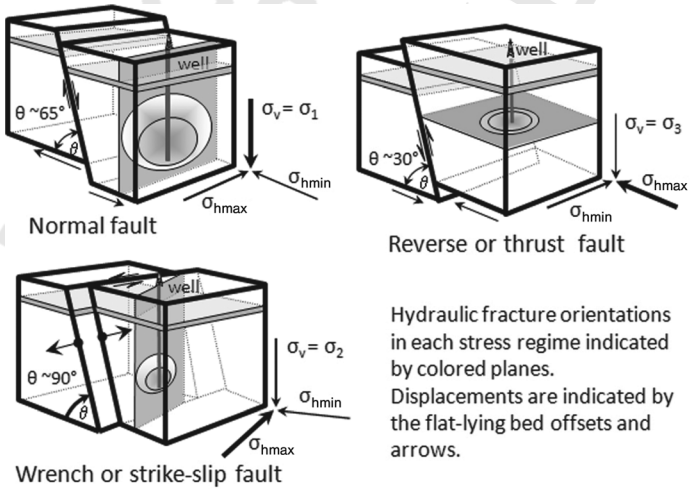

Figure 2.23 Stress regimes, characteristic fault orientations, typical hydraulic fracture orientations. (Please find a color version of this figure on the color Plates).

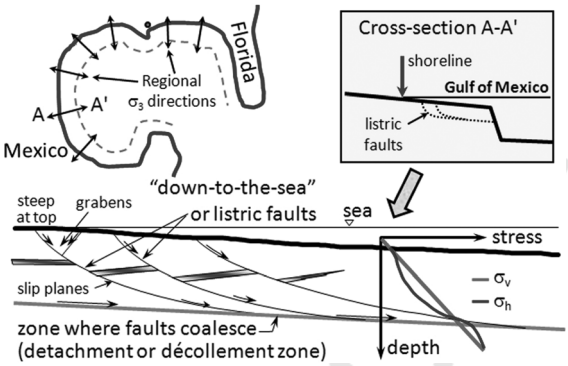

Figure 2.24 Gulf of Mexico or listric fault regime (also "down-to-the-sea" or "growth" faults).

example, σ_3 ($= \sigma_{h\,\min}$) points in the direction of the strike of an active, planar, high-angle fault (a normal fault), but at 90° to the strike of a compressive thrust fault. In the latter case, it is also the vertical stress, σ_v. If the fault is a strike-slip fault, the direction of motion must be determined, and then σ_3 ($= \sigma_{h\,\min}$) directions can be estimated; usually, $\sigma_{h\,\min}$ lies in an orientation about 60–70° from the strike of a fault. Care is necessary to assure that the features are related to the present-day stresses, and that there has not been a stress field rotation since the time the fault was active. This method works well, in a regional sense, near active rifting (e.g., East Africa rift belt) and active compressive mountain building (e.g., Rocky Mountains and Andean forelands). Of course, local distortions can be superimposed on this stress field, particularly with greater distance from the active mountain front.

In some basins, the large-scale geometry controls the stress distributions, particularly along continental margin basins (Figure 2.24). Along the Gulf Coast of the United States, $\sigma_{h\,\min}$ is consistently aligned perpendicular to the continental shelf trace, with local variations superimposed from salt tectonics and local effects. Inland basins far from mountain-building or rift tectonics may also have a regional signature imposed by the geometry of the basin.

Other geological factors can affect the stress fields at scales of 1–30 km, including volcanism, salt diapirism, regional arching or subsidence, or lithological differences. For example, in the salt-diapir related chalk oil-fields in the North Sea, a radial distribution has been superimposed. In areas of intense gas migration and active pore pressure generation, effective stresses are severely affected. In strongly uplifted regions, on the other hand, pore pressures can be much lower than hydrostatic. In such cases, measurements combined with geological inference should be used.

The orientation of large, hydraulically induced fractures will be at 90° to the orientation of σ_3. Provided that $\sigma_{h\,\min} = \sigma_3$, the fracture will propagate vertically in the natural stress field. The fracture must be large enough to be beyond the effects of the borehole region, and much larger than any joint spacing in the rock (joints affect local but not large-scale propagation direction). Hydraulic fracture orientation can be determined in various ways, but perhaps the most reliable method for large, vertical fractures at moderate depths (<3 km) is high-precision tiltmeters arrayed on the

surface (Wills *et al.*, 1992). Other methods use direct borehole measurements, interference tests among wells (one of which was fractured), microseismic mapping, and so on.

Finally, seismic shear wave velocity anisotropy can reflect stress anisotropy. However, wave transmission is highly sensitive to fabric, and if the rocks now have a different stress orientation than when the fabric developed through diagenesis and tectonics, seismic anisotropy may not reflect present-day stress orientations. Sonic dipole geophysical logs can determine seismic attributes anisotropy in the plane of the borehole, and these data may be used to estimate orientations and relative effective stress magnitudes. These data are then "calibrated" using leak-off tests (LOT, XLOT) or hydraulic fracture data (MiniFrac or similar tests), and the service company then provides a continuous estimate of the stresses with depth. Of course, as with all correlations, caution should be exercised in using the data.

2.3.1.4 Stress Magnitude Estimation

The vertical total stress, σ_v, is the weight of the overlying rocks (and water) acting on a unit area. This can be calculated using a density log assisted by precise core density measurements. It can usually be calculated to within ± 2 MPa at a depth of several kilometers, or within 2–3% with excellent reliability (95% probability).

The relative magnitude of the principal stresses can often be gauged by geological inference, using the tectonic history of the basin, appropriate faults, domal structures, and so on. For example, mobilized salt at depth sometimes forms distinct elongated ridges (almost "waves"); these are at 90° to the direction of $\sigma_{h\,\min}$ ($= \sigma_3$), and thus a relative magnitude is obtained, compared with the other two stresses. Other features (faults, folds, fracture patterns, . . .) can be used to estimate relative stress magnitudes, but quantification of stress values requires further information.

In discussing stresses, K', the ratio of the horizontal to vertical effective stresses is often used: $K' = \sigma'_{h\,\min}/\sigma'_v$. If $K' > 1.0$, lateral stresses are greater than σ_v and induced hydraulic fractures will be horizontal; these are thrust fault conditions (Figure 2.23), sometimes called compressional conditions. If $K' < 1.0$, normal or strike-slip fault conditions exist, called extensional and transpressional, respectively, and hydraulically induced fractures will be vertical. Also, on an active fault plane with friction angle φ' and no residual cohesion, the following effective stress ratio exists: $\sigma'_1/\sigma'_3 = (1 + \sin\varphi')/(1 - \sin\varphi')$. This relationship allows stress estimates to be made in some circumstances.

If a fault has been active in the recent geological past (tens of thousands of years), frictional behavior along the fault plane can be assumed; this gives some bounds to the horizontal stresses near the fault. Consider a 4 km deep active normal fault with $\sigma_v = 95$ MPa and $p_0 = 50$ MPa. We can estimate $\sigma_v = \sigma_1$ and $\sigma'_v = \sigma_v - p_0 = 45$ MPa. Assume a friction angle $\varphi' = 30°$; then, $K' \approx 0.33$ if rock is in the critical slippage condition. $\sigma'_{h\,\min} = \sigma'_3 = K'\sigma'_v = 15$ MPa and, therefore, $\sigma_{h\,\min} = \sigma'_{h\,\min} + p_0 = 15 + 50 = 65$ MPa. This is considered to be a lower-bound estimate for $\sigma_{h\,\min}$; the actual value of $\sigma_{h\,\min}$ in the fault region is probably in the range 65–75 MPa. Since $\sigma_{h\,\max} = \sigma_2$ and $\sigma_3 < \sigma_2 < \sigma_1$, $65\text{ MPa} < \sigma_{h\,\max} < 95$ MPa. Often, we estimate $\sigma_2 = (\sigma_1 + \sigma_3)/2$ so that $\sigma_{h\,\max} \approx 80$ MPa

It is instructive to repeat these calculations for a typical Gulf of Mexico listric fault at 5 km depth. The deep detachment plane is horizontal, in a zone of overpressure, and along a shale band. Although σ_v may no longer be exactly a principal stress, we will assume that it is: $\sigma_v = \sigma_3 = 105$ MPa, $p_0 = 85$ MPa, and the shale friction angle $\varphi' = 10^\circ$, so that $K' \approx 1.4$ at the condition of fault slip. Carrying out calculations gives $\sigma_{h\,\max} = 113$ MPa and $\sigma_{h\,\min}$ in the range 105–113 MPa. One notable factor is that in an overpressured regime with slip along low-friction shale beds, all of the principal stresses are of similar value.

Leak-off tests (LOTs), carried out when a casing shoe is drilled, are used to estimate the magnitude of σ_3 (usually $\sigma_3 = \sigma_{h\,\min}$ in these cases). During a LOT, if pumping is stopped after a slope change (Figure 2.25), and before a clear pressure drop takes place, a poor estimate of $\sigma_{h\,\min}$ may be obtained. Best practice is to continue pumping until a after a pressure drop is observed and a stabilized injection pressure is being approached. This is referred to as an extended leak-off test (XLOT), and σ_3 estimates using XLOT are more reliable.

Hydraulic fracturing is used to estimate stress magnitudes (Figure 2.26). Note that XLOTs are merely hydraulic fractures executed with the drilling fluid as the injectate, but there remain issues of possible pressure losses in the annulus, which can introduce errors. Fracturing stress measurements are offered commercially by several service companies (e.g., MiniFrac); they use precision pumps, downhole gauges, and a refined methodology. Such data are highly reliable σ_3 estimates, considered to give information within a small percentage of true values with 95% certainty. Much has been claimed about the possibility of using hydraulic fracture data to obtain information on the other horizontal stress ($\sigma_{h\,\max}$), through use of the fracture breakdown pressure (peak pressure before the pressure drop). The most that can be said is that the value obtained is almost certainly a lower-bound estimate, for several reasons (thermal effects, borehole wall damage, existence of natural fractures); actual $\sigma_{h\,\max}$ values are likely to be different from values based on hydraulic fracture data.

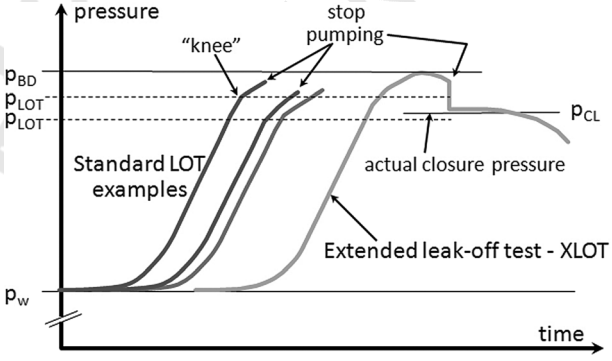

Figure 2.25 LOTs are best extended beyond the peak pressure – XLOT – for reliable σ_3 measurements. See Figure 2.24 for definitions of some of the terms.

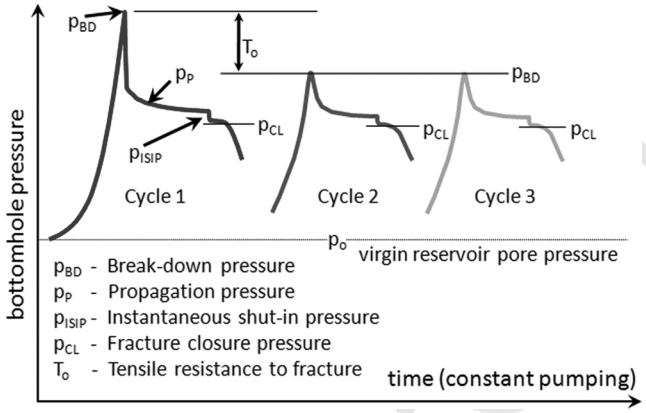

Figure 2.26 A detailed hydraulic fracture stress measurement procedure with multiple cycles.

Lateral stresses do not necessarily increase monotonically with depth, as σ_v does. Strata of different stiffnesses will display deviations from a regular increase in lateral stress magnitude; the amount and nature of the difference depends on the lithology, the mechanical properties (stiffness, creep capacity), and the deformation and stress history. In general, because of slow shear stress relaxation, σ_h values in ductile shales are closer to σ_v than are the σ_h values in adjacent dolomites and sandstones. Salt is a material which creeps under differential stress, so one may assume that virgin salt has an isotropic stress state *in situ* ($\sigma_v = \sigma_h$).

Figure 2.27 shows a hypothetical stress distribution that might arise if a sequence of beds of different stiffness is subjected to a small lateral compression in a foreland basin adjacent to compressive tectonics (e.g., west side of the Appalachians in the United States, east side of the Andes mountains). The stiffer beds have taken the greatest load, ductile shales less so, and the salt remains at an isotropic stress state. In an extensional stress regime or a depleted reservoir, one might expect the mirror image, with the stiffest beds having the lowest σ_h value, and so on. An understanding

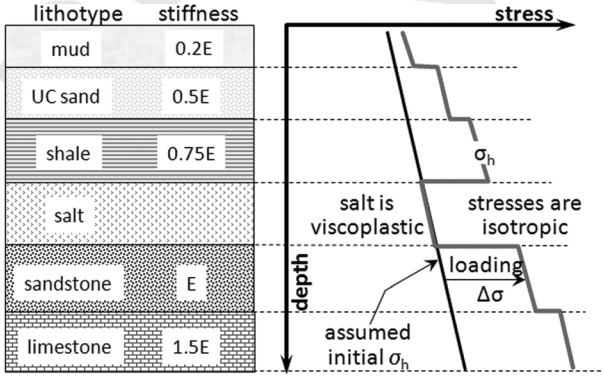

Figure 2.27 Relative stress values arising from compressional strain in a compressive foreland.

of the tectonic evolution of a sedimentary basin gives clear clues as to the distribution of stresses among various rock units.

2.3.1.5 Pore Pressures: $p_0(z)$

To complete the stress state, pore pressure values are required, and these data are also vital to design casing programs and manage blow-out risk in drilling. Robust $p_0(z)$ estimates based on geological inference, offset well data, seismic interpretation, and regional trends, are usually available. Properly calibrated correlations with geophysical log data and seismic attributes exist for some regions, but for other regions the relationships are weak or insufficiently calibrated. Ultimately, true $p_0(z)$ values must be measured directly using formation testing methods or installed sensors. Fortunately, $p_0(z)$ data are vital to oil exploration and reservoir engineering, so there is an incentive to collect good data; nevertheless, p_0 values in shallow strata, shales, and other non-reservoir rocks are rare. During hydraulic fracturing for stress measurements, a good measurement of p_0 is almost always collected to round out knowledge of the stress state.

In drilling activity, great attention is paid to influxes of hydrocarbons, water, or even the sudden onset of shale sloughing; all of these are indicators that the mud weight is less than p_0, and such data can be valuable estimates of pore pressures.

After application of various approaches, it is usually possible to have good data on orientations, and reasonable data on p_0, σ_v, and $\sigma_{h\,\min}$. Thus, the stress state can be reasonably estimated and used in geological, geomechanical, and reservoir management applications, and also in drilling prognoses and analyses.

2.3.1.6 Typical Stress Distributions with Depth

Based on experience, combined with some measurements and geological inference, it is possible to make valuable generalizations about stress distributions with depth in a number of tectonic environments. These are first-order estimates based on simple models; exceptions will always be found, and site-specific data must be developed by more detailed study.

2.3.1.6.1 Non-Tectonic Classical Basin and Diagenetic Effects In a monotonically sedimented basin without erosion or significant lateral strain events (compressional, extensional, transpressional), lateral stresses are less than vertical stresses. Figure 2.28 shows a stress distribution that might be expected in such a basin. Some general comments can be made for such cases.

The minimum K' value to be expected is perhaps 0.4–0.5 in sands and carbonates and 0.6–0.7 in shales. For example, at $z = 3$ km with $\sigma_v = 70$ MPa, $p_0 = 30$ MPa, in a sandstone bed we would expect $\sigma_{h\,\min} \approx \sigma_{h\,\max} = 45$–$55$ MPa, and in an adjacent shale, 55–60 MPa. Shale ductility and large strains during compaction mean that $\sigma_{h\,\min}$ in shales is closer to σ_v than in sandstones. However, diagenesis has a large role, especially in soluble rocks. The effect of standard burial diagenesis (compaction, pressure solution, cementation) is complex and only a few examples are presented here.

Smectite-to-illite mineralogy changes take place in shales as burial depth and temperature increase. In the Gulf of Mexico, smectite is a dominant clay mineral in

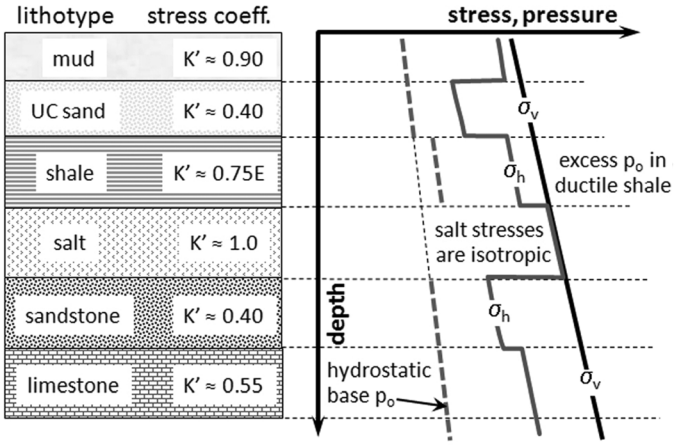

Figure 2.28 Stress coefficient values and stress distribution in a monotonically buried basin.

shales to $z \approx 3$–4 km, but is totally absent by $z \approx 6$–7 km. Consider the stress effect in a flat-lying bed of smectitic shale. A large volume change accompanies the smectite illite transition, giving a shrinkage potential of at least several percent in most smectitic shales. In the vertical direction, shrinkage is merely compaction; in the horizontal direction, because no-lateral-strain conditions apply, it results in σ_h loss until $p_0 > \sigma_h$. Furthermore, because the smectite → illite transition expels water, p_0 may rise in restricted drainage conditions. Extensive fracturing takes place, and a naturally fractured quartz–illite shale is generated with a greatly reduced lateral stress. These materials are prone to lost circulation and massive sloughing.

Gypsum ($CaSO_4 \cdot 2H_2O$) changes to anhydrite ($CaSO_4$) with burial and temperature, but the high solubility of these minerals means that pressure dissolution and recrystallization processes continue slowly, reducing the difference between σ_v and σ_h, and also eliminating porosity in the process, generating a dense impermeable and non-fractured rock in which all stresses are close to the same value. Of course, salt creeps several orders of magnitude more rapidly than anhydrite, so in salt, all stresses are equal.

Dolomitization involves shrinkage, generating vertical fractures and reduced horizontal stress.

Pressure solution and recrystallization of SiO_2 in quartz sands lead to significant porosity loss. The process is sensitive to the stresses at the grain contacts: higher local stresses lead to higher dissolution rates, which in turn tend to give larger contact areas, lower local stresses, and attenuation of the process. The negative and positive feedback processes involved in sandstone diagenesis are excellent examples of the coupling of stresses, chemistry, fluid flux, and temperature in the real world, altering stresses, permeability, and rock fabric over time.

2.3.1.6.2 **Eroded Basin** As rocks are buried, diagenesis makes them stronger and stiffer through compaction and porosity loss. Thus, in an erosive process, they are likely to respond elastically during unloading. Consider a flat-lying stratum subjected

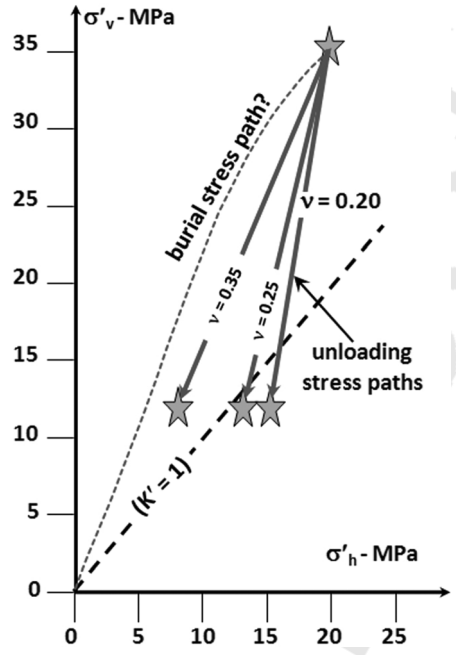

Figure 2.29 Stress path for elastic unloading arising because of erosion.

to general uniform unloading through erosion. $\Delta\sigma'_v$ leads to vertical elastic strain, ε_z, but the no-lateral-strain condition ($\varepsilon_x = \varepsilon_y = 0$) leads to the following relationship, often referred to as the "Poisson effect":

$$\Delta\sigma'_h = \frac{\nu}{1-\nu}\Delta\sigma'_v$$

For sands, Poisson's ratio is about 0.25, therefore $\Delta\sigma'_h \approx 0.33\Delta\sigma'_v$. Consider a sandstone buried to a depth of 3 km ($\sigma_v = 70$ MPa, $\sigma_h = 55$ MPa, $p_0 = 35$ MPa), and then erosion takes place until $z = 800$ m and $\sigma_v = 20$ MPa, $p_0 = 8$ MPa. $\Delta\sigma'_v = -23$ MPa, thus $\Delta\sigma'_h \approx 0.33\Delta\sigma'_v \approx -7.5$ MPa. Applying these changes to the initial conditions, $\sigma_v = 20$ MPa, $p = 8$ MPa, and $\sigma_h = 20.5$ MPa; the stress condition has changed from normal ($\sigma_v = \sigma_1$) to thrust ($\sigma_v = \sigma_3$). The stress path is sketched in Figure 2.29, and also stress paths for two other values of Poisson's ratio, 0.20 and 0.35, the latter considered more appropriate for shales.

In all eroded non-tectonic basins, such as the Michigan and Williston Basins on the United States–Canada border, a "skin" has formed where instead of $\sigma_v = \sigma_1$, the condition $\sigma_v = \sigma_3$ now exists. Depending on the amount of erosion and the initial state before erosion, this "skin" is perhaps several hundred meters to 1–2 km thick. This is why hydraulic fractures in shallow (<500 m) gas sands or oil sands in Alberta tend to be horizontal, but deeper fractures tend to be vertical. A typical stress distribution with depth is shown in Figure 2.30. High pore pressures are fairly rare in eroded basins.

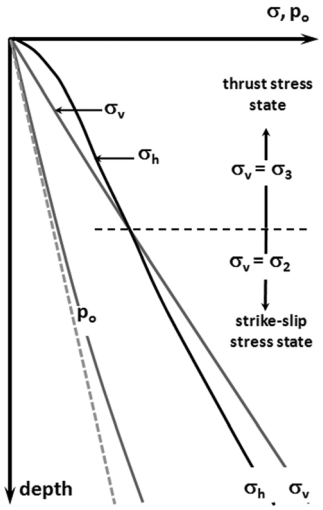

Figure 2.30 Stresses in an eroded basin.

2.3.1.6.3 **Continental Margin Basin** Figure 2.31 shows the Gulf of Mexico model of stresses with depth in the listric faulting region. The major features are a normal fault regime near the surface changing to a thrust regime at depth, a highly overpressured zone in which the horizontal detachment fault is found (high p_0 = low strength), and a stress "reversion" at depth related in part to lower pore pressures. In the overpressured regime the stresses are close to one another because of the elevated pore pressures and the ductility of the "under-compacted" sediments.

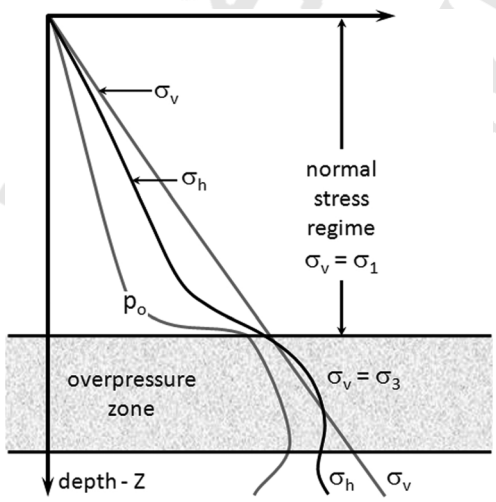

Figure 2.31 Stresses in a continental margin basin.

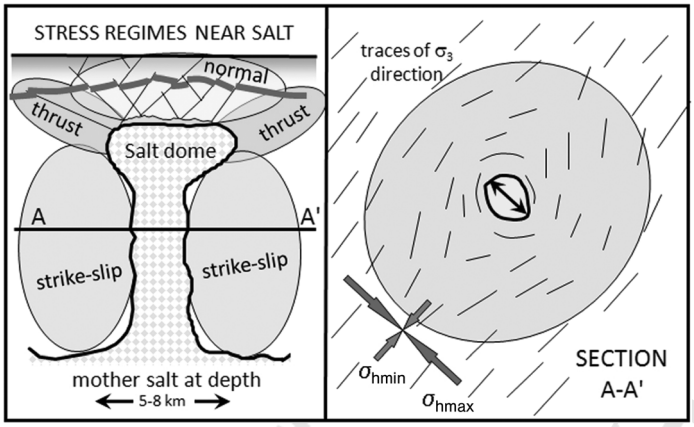

Figure 2.32 Because of the intrusion of the salt, compressive horizontal strains formed different stress regimes, depending on location. On a regional scale, the salt dome perturbs the stress regime for perhaps 4–6 dome diameters, depending on rock stiffness.

There are many other subtle features of the stress regimes of the Gulf of Mexico. Shallow gas sands only 300–1500 m below the sea floor are common, presenting great risks to drilling; these sands contain old catagenic gas (not shallow organic gas), indicating a deep pressure valving and hydraulic fracture process for emplacement. In the upper 4–5 km, above the overpressured interval, the pore pressures in shales are perhaps 10% higher than in the surrounding thick shales, so that if mud weight is keep just low enough to control sandstone pressures, shale sloughing acceleration is noted.

Salt diapirism can perturb the stress in a continental margin basin at a scale of perhaps 5–10 salt dome diameters around the dome (Gulf of Mexico, North Sea, offshore Nova Scotia, etc.). Figure 2.32 shows stresses near a salt dome, although highly complex salt structures also exist with components of faulting, horizontal salt emplacement, and so on. In this simple model, the large radial strain imposed on the rocks during domal emplacement means that $\sigma_r = \sigma_1$ and $\sigma_\theta = \sigma_3$ near the dome stock (strike-slip). Above the dome, normal faulting is associated with extensional strain. During drilling near a salt dome, it is possible to pass from a normal fault regime through a thrust fault regime, and then into a strike-slip regime. For more complex, faulted cases also involving salt tectonics, the stress state with depth can be difficult to predict.

2.3.1.6.4 **Compressional Tectonics Foreland Basin** Figure 2.33 shows a series of stress plots in a compressional foreland basin. Typical examples include Alberta and similar Rocky Mountain foreland regions, including the Andean foreland basins stretching from eastern Colombia to the southern tip of Argentina. Near the thrust faults, $\sigma_v = \sigma_3$ for considerable depths, eventually transitioning into a strike-slip regime at greater depth. Farther from the compressional front (100–200 km), the

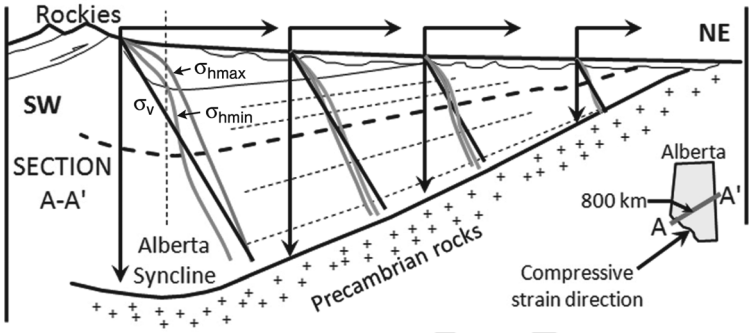

Figure 2.33 Stresses in a compressive foreland basin. Near the mountains, σ_1 is normal to the strikes of the thrust faults, and may be $\sigma_{h\,max}$ for great depths. Away from the mountains, compressive strain effects persist, but less so than near the disturbed belt. Blue line is $\sigma_{h\,max}$, red line is $\sigma_{h\,min}$. (Please find a color version of this figure on the color Plates).

depth to the transition is shallower, and at great depth it may be possible to encounter normal fault conditions. At great depth in the foreland syncline, pore pressures may be as high as 1.2–1.3 × hydrostatic, but high overpressures are rare.

2.3.1.6.5 **Transpressional Conditions** Two classic examples of strong transpressional conditions are the San Andreas fault system in southern California and the strike-slip faults of east-central Colombia (Cusiana Field) and western Venezuela (the Icotea fault passing through the middle of Lake Maracaibo). In these cases, the strike-slip conditions appear to continue to great depth, and if the faulting is active and the rate of strain is large, the two horizontal stresses can approach values of $\sigma'_{h\,max}/\sigma'_{h\,min} \approx 2.5$–2.8, essentially the condition of shear failure. In such tectonically active areas, massive shear failure and enlargement of boreholes during drilling are common, and the effects of depletion and injection can be startling, triggering small earthquakes or changes in fracture aperture because of shear distortion.

2.3.1.7 Thermal and Pressure Effects on Reservoir Stresses

Drilling often has to take place through zones that are depleted or subjected to temperature changes. A brief discussion of some effects is given here.

Depletion of a flat-lying extensive reservoir involves conditions of no lateral strain, constant σ_v, and a pressure drop Δp. Applying these in a linear elastic model leads to the prediction of a Poisson's ratio-controlled lateral total stress loss during depletion:

$$\Delta\sigma_h = \frac{1-2\nu}{1-\nu}\Delta p \left(\text{as well as } \Delta\sigma'_v = \Delta p \text{ and } \Delta\sigma'_h = \frac{-\nu}{1-\nu}\Delta p\right) \tag{2.44}$$

This is known as the reservoir stress path, and the multiplier of Δp in the equation is known as the stress path coefficient, often taken as 0.67 (for $\nu = 0.25$). In practice, the stress path coefficient is known to vary substantially, from values as low as 0.45 to as high as 1.1 in cases where there is stress-triggered fabric breakdown. For intact

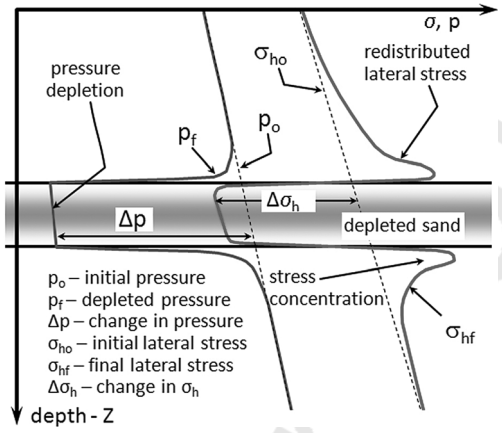

Figure 2.34 Reservoir depletion reduces the lateral stress. In this example, the lateral stress has been reduced below the pore pressure in surrounding strata, a difficult drilling condition.

sandstones, a stress path coefficient of 0.65–0.75 is recommended, and for intensely fractured reservoirs, 0.8–0.9 may be used for preliminary estimates. Using typical values for Δp shows that secondary drilling through the zone may result in lost circulation, particularly if it is necessary to maintain a high drilling fluid density because of thin high-pressure gas zones above the reservoir (Figure 2.34). It is possible to "restress" a region around the borehole through controlled injection of solids such as lost-circulation material, cuttings, mud solids, or $CaCO_3$, until a stress cage develops around the hole, reducing the tendency for hydraulic fracture. This process may help avoid additional casing strings and reduce blowout risk, but it is a delicate procedure.

Depletion of very large volumes can lead to triggering of normal fault earthquakes, particularly if the reservoir was initially in a stress state close to yield. Of course, injection leads to similar changes but with different signs, until the condition $p > \sigma_3$ is reached, at which point hydraulic fracture can be expected (shear yield can precede reaching the fracture condition in rocks of low cohesion). At high injection pressures, bedding plane slip (a form of thrust faulting) can be triggered, perhaps leading to casing shear.

Heating the reservoir through injection of hot fluids (ΔT as much as 250 °C in the case of steam injection at $z = 500$ m) leads to huge increases in lateral stresses, and simple elastic calculations show that the shear strength limit is soon reached, such that σ_v becomes σ_3 and thrust fault slip conditions limit the stresses. Drilling into a hot reservoir not only carries risks associated with heat, but also borehole problems if the lateral stresses are at the yield point.

Cooling the reservoir is usually associated with water disposal, and ΔT of -30 to -50 °C is feasible. Loss of lateral stress combined with the injection pressure means that the condition $p > \sigma_3$ ($= \sigma_{h\,\min}$) can be easily reached, so that hydraulic fracturing takes place (more often, the opening of existing fractures). This invariably improves

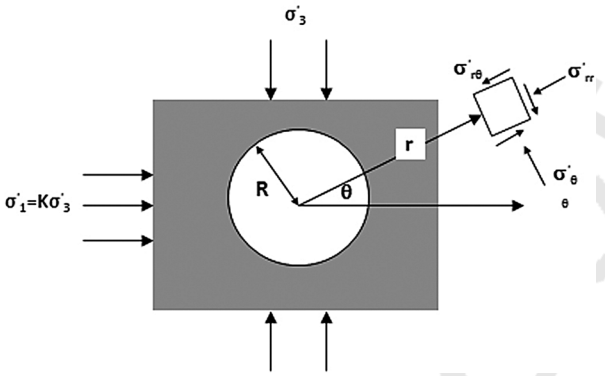

Figure 2.35 Initial stress distributions around wellbore (Brady and Brown, 1985).

the performance of the injection well, but if a large cooled zone has to be drilled, lost circulation problems may be encountered.

2.3.2 Stresses Around a Borehole

2.3.2.1 Elastic Stresses Around a Borehole

According to Brady and Brown (1985), Kirsch originally derived the complete linear elastic solutions for the two-dimensional stress distribution and displacement field around a hole loaded by two principal stresses in the far field (Figure 2.35):

$$\sigma'_{rr} = \frac{\sigma'_3}{2}\left[(1+K)\left(1-\frac{R^2}{r^2}\right)-(1-K)\left(1-4\frac{R^2}{r^2}+\frac{3R^4}{r^4}\right)\cos 2\theta\right] \tag{2.45a}$$

$$\sigma'_{\theta\theta} = \frac{\sigma'_3}{2}\left[(1+K)\left(1+\frac{R^2}{r^2}\right)+(1-K)\left(1+\frac{3R^4}{r^4}\right)\cos 2\theta\right] \tag{2.45b}$$

$$\sigma'_{r\theta} = \frac{\sigma'_3}{2}\left[(1-K)\left(1+\frac{2R^2}{r^2}-\frac{3R^4}{r^4}\right)\sin 2\theta\right] \tag{2.45c}$$

where σ'_{rr}, $\sigma'_{\theta\theta}$, and $\sigma'_{r\theta}$ are the effective stresses around the hole, assuming that the pore pressure is constant, R is the borehole radius, r and θ are cylindrical coordinates, σ'_1 is the maximum effective principal stress and σ'_3 is the minimum effective stress, and K is the ratio between them. For a vertical hole, σ'_1 and σ'_3 become maximum and minimum effective horizontal stresses ($\sigma'_{h\,\max}$ and $\sigma'_{h\,\min}$).

When far field stresses are isotropic, that is, $\sigma'_1 = \sigma'_2 = \sigma'_3$, the stresses near the wellbore become

$$\sigma'_{rr} = \sigma'_3\left(1-\frac{R^2}{r^2}\right) \tag{2.46a}$$

$$\sigma'_{\theta\theta} = \sigma'_3\left(1 + \frac{R^2}{r^2}\right) \tag{2.46b}$$

$$\sigma'_{r\theta} = 0 \tag{2.46c}$$

The difference between σ'_{rr} and $\sigma'_{\theta\theta}$ is $\sigma'_{rr} - \sigma'_{\theta\theta} = -2\sigma'_3(R^2/r^2) < 0$, which indicates that σ'_{rr} is always less than $\sigma'_{\theta\theta}$. Further, the greatest stress difference occurs at the borehole radius $r = R$:

$$\sigma'_{\theta\theta} = \sigma'_3[(1+K) + 2(1-K)\cos 2\theta] \tag{2.48a}$$

$$\sigma'_{rr} = 0 \tag{2.48b}$$

$$\sigma'_{r\theta} = 0 \tag{2.48c}$$

There is no effective radial stress at the borehole wall if it is a free boundary.

When far field stresses are isotropic, Equation 2.48a becomes

$$\sigma'_{\theta\theta} = (\sigma'_1 + \sigma'_3) + 2(\sigma'_1 - \sigma'_3)\cos 2\theta \tag{2.49}$$

If $\theta = 0$, $\sigma'_{\theta\theta} = 3\sigma'_1 - \sigma'_3$, whereas for $\theta = \pi/2$, $\sigma'_{\theta\theta} = 3\sigma'_3 - \sigma'_1$. These represent the greatest and the smallest values of the tangential stress at the borehole wall, and are used to estimate the initiation of a hydraulic fracture.

Bearing the above discussion in mind, the stress distributions around a wellbore in a plane are sketched in Figure 2.36. The dashed lines represent stress distributions that are perpendicular to the direction of the minimum principal stress (σ'_3). The rock has been treated as an isotropic elastic material, temperature is constant, and the effect of fluid flow is neglected.

2.3.2.2 Elastic Stresses Around a Borehole with Fluid Flow

For an elastic isotropic formation, stress equilibrium around a borehole in cylindrical coordinates can be expressed as

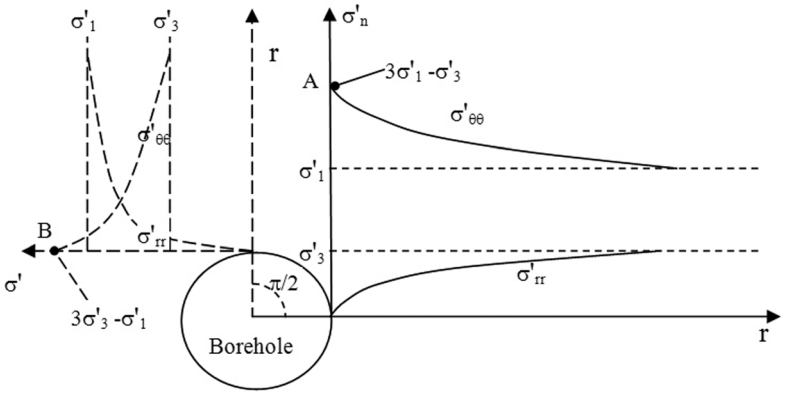

Figure 2.36 Stress distribution in the directions of $\theta = 0$ and $\theta = \pi/2$ around a hole.

$$\frac{\partial \sigma'_r}{\partial r} + \frac{\sigma'_r - \sigma'_\theta}{r} = \alpha \frac{\partial P}{\partial r} \tag{2.50}$$

where α is the Biot constant and the fluid pressure P changes with location and time. The solutions for total stresses can be found as (Wang and Dusseault, 1991)

$$\sigma'_r = \alpha P(r,t) + \frac{Ec_1(t)}{(1+\nu)(1-2\nu)} - \frac{Ec_2(t)}{(1+\nu)}\frac{1}{r^2} - \frac{1-2\nu}{1-\nu}\frac{\alpha}{r^2}\int^r rP(r,t)\mathrm{d}r \tag{2.51a}$$

$$\sigma'_\theta = \alpha\frac{\nu}{1-\nu}P(r,t) + \frac{Ec_1(t)}{(1+\nu)(1-2\nu)} + \frac{Ec_2(t)}{(1+\nu)}\frac{1}{r^2} + \frac{1-2\nu}{1-\nu}\frac{\alpha}{r^2}\int^r rP\mathrm{d}r \tag{2.51b}$$

Assuming steady fluid flow into the borehole, the pore pressure varies only with radius and follows Darcy's rule:

$$P(r) = P_1 + \bar{K}\ln\left(\frac{r}{R_1}\right) \tag{2.52}$$

where $\bar{K} = Q\mu/2\pi kh$, R_1 is the wellbore radius, and P_1 is the bottom flowing pressure. If the flow rate Q is constant, effective stresses can be expressed as (Han and Dusseault, 2003)

$$\sigma'_r = \frac{0.5\alpha}{1-\nu}P + \frac{Ec_1}{(1+\nu)(1-2\nu)} - \frac{Ec_2}{(1+\nu)}\frac{1}{r^2} + \alpha\frac{0.5-\nu}{1-\nu}\frac{\bar{K}}{2} \tag{2.53a}$$

$$\sigma'_\theta = \frac{0.5\alpha}{1-\nu}P + \frac{Ec_1}{(1+\nu)(1-2\nu)} + \frac{Ec_2}{(1+\nu)}\frac{1}{r^2} - \alpha\frac{0.5-\nu}{1-\nu}\frac{\bar{K}}{2} \tag{2.53b}$$

Coefficients c_1 and c_2 are variables related only to time and determined by boundary conditions. An appropriate condition is to assume that the effective radial stress is zero at the borehole wall and equals the horizontal effective stress at far field (R_2):

$$r = R_1, \sigma'_r = 0; \quad \text{and} \quad r = R_2, \sigma'_r = \sigma'_h \tag{2.54}$$

c_1 and c_2 can be shown to be

$$c_1 = \frac{(1+\nu)(1-2\nu)}{E}\left[\frac{R_2^2}{R_2^2 - R_1^2}\left(\sigma_h + \alpha\frac{0.5-\nu}{1-\nu}P_2 + \frac{R_1^2}{R_2^2}\frac{0.5\alpha}{1-\nu}P_1\right) - \alpha\frac{0.5-\nu}{1-\nu}\frac{\bar{K}}{2}\right] \tag{2.55a}$$

$$c_2 = \frac{1+\nu}{E}\frac{R_2^2 R_1^2}{R_2^2 - R_1^2}\left[\sigma_h + \alpha\frac{(0.5-\nu)P_2 + 0.5P_1}{1-\nu}\right] \tag{2.55b}$$

An example of the elastic stress solutions is plotted as dotted lines in Figure 2.37.

2.3.2.3 Inelastic Stresses Around a Borehole with Fluid Flow

The previous solutions are based on the assumption that the formation is elastic and that no failure occurs. However, weak or unconsolidated rocks are more likely to be

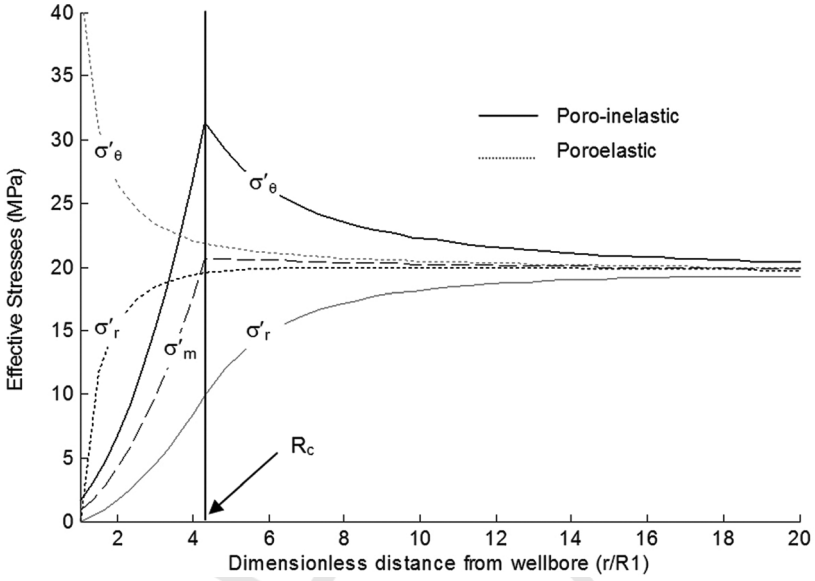

Figure 2.37 Effective stresses, σ'_r and σ'_θ, around a borehole: dotted lines are poro-elastic solutions, solid lines are poro-inelastic solutions. σ'_m is the average of the two stresses (Han and Dusseault, 2003).

yielded and mobilized by stresses and fluid flow, which may lead to borehole collapse, for example.

Assuming that the rock stresses around a borehole in a weak rock formation satisfy the M–C failure criterion, the stress solutions have been found (Han and Dusseault, 2003):

$$\sigma'_r(r) = \frac{c_3}{\omega} r^{-\omega} + \frac{2c_0 \tan\beta + \alpha\bar{K}}{\omega} \tag{2.56a}$$

$$\sigma'_\theta(r) = \frac{c_3(1-\omega)}{\omega} r^{-\omega} + \frac{2c_0 \tan\beta + (1-\omega)\alpha\bar{K}}{\omega} \tag{2.56b}$$

where $\omega = 1 - \tan^2\beta$. The constant c_3 can be given as

$$c_3 = -(2c_0 \tan\beta + \alpha\bar{K}) R_1^{\omega} \tag{2.57}$$

Plotting and comparing these with their poroelastic counterparts (Figure 2.37), the inelastic stresses shift the concentration of shear stress away from the wellbore. A Coulomb zone has been identified and defined through a critical radius R_c. In this zone, rock has yielded and been damaged to certain extent but has not completely lost its functionality and fallen into the borehole. For strong rock with low *in situ* stress magnitude, the Coulomb zone may not exist.

The analytical solutions for the inelastic case have to assume isotropic far-field stresses (i.e., $\sigma'_{h\,\max} = \sigma'_{h\,\min}$) to avoid prohibitive mathematical challenge. For

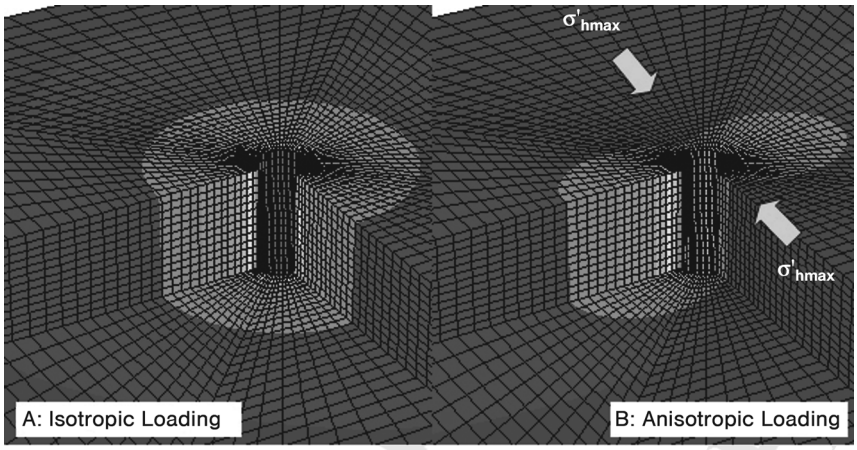

Figure 2.38 Rock deformation around a borehole when (a) isotropic loading ($\sigma'_{H\,\max} = \sigma'_{h\,\min}$) and (b) anisotropic loading ($\sigma'_{H\,\max} > \sigma'_{h\,\min}$). (Please find a color version of this figure on the color Plates).

anisotropic far field stresses $\sigma'_{h\,\max} > \sigma'_{h\,\min}$, numerical solutions of rock deformation around a pressurized vertical borehole are plotted in Figure 2.38. Instead of distributing evenly around the borehole in the isotropic case, rock deformation concentrates in the direction perpendicular to the maximum horizontal stress. These concentrated deformation zones near the wellbore have a highest risk of borehole collapse or instability, compared with the rest of the formations around the hole.

2.3.2.4 Heating and Cooling the Borehole

Thermal exchange between drilling fluid and rock occurs naturally. Figure 2.39 is a simplified sketch of the drilling fluid and *in situ* rock temperatures that might be encountered during drilling on land. Offshore, the temperatures are greatly complicated by the cooling and heating that occur in the section of the riser that makes contact with sea water, which can be on the order of 1–4 °C at the sea floor in deep offshore drilling.

Clearly, there can be a large difference between the mud temperature and the formation temperature. Below the cross-over point in Figure 2.39, the returning drilling fluid is cooler than the formation temperature. This has the following effects:

- transient reduction of the temperature in the borehole wall rock;
- reduction in the rate of diffusion processes, such as:
  -reduction of creep rates in salt;
  -increase in the viscosity of pore fluids;
  -reduction in shale reaction rates (e.g., adsorption–desorption reactions);
- slight thermoelastic shrinkage of the rock, leading to a significant decrease in the effective tangential stress σ'_θ in the near-borehole region.

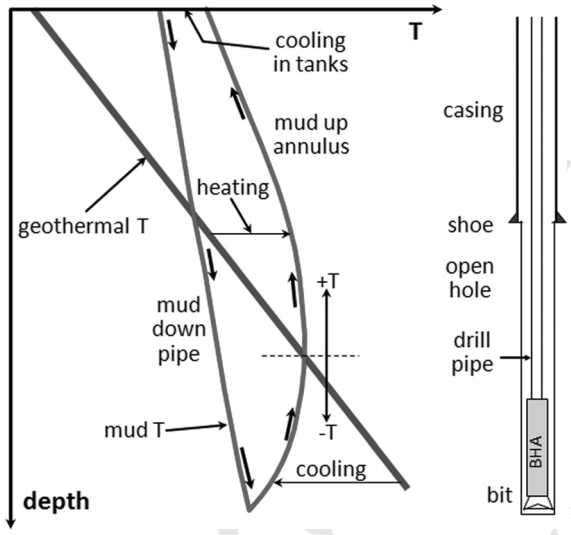

Figure 2.39 Drilling involves cooling the rock in the drill-bit region, helping stabilize the hole, while heating the rock higher in the borehole, potentially destabilizing the rock.

This effect can be a major advantage for a drilling operation, reducing the rate of bottom-hole sloughing, mass transfer, and related problems. On the other hand, consider the drilling fluid temperature at the casing shoe in Figure 2.39; it is much higher than the formation temperature, and this causes effects opposite to those listed above, which in many cases are known to lead to accelerated sloughing and hole-cleaning problems (Wang and Dusseault, 2003).

Figure 2.40 shows approximately the shape of the tangential stress distribution that one might expect from heating or cooling the borehole wall. In the heating case, the heated zone expands, so the maximum compressive stresses are increased massively, and usually the shear stresses also increase. When a wellbore is subject to cooling, however, rock around the hole shrinks and therefore the tangential stress decreases. The specific shape depends on the magnitude of convective versus conductive heat flow, although it is reasonable to assume that in the case of boreholes, conductive heat flux dominates, whereas in cases of injection and production into permeable reservoirs, convective heat flux dominates.

For a quick approximation of how much the σ'_θ values in the wall can change, the following thermoelastic equation can be used, but only on the borehole wall:

$$\Delta\sigma'_\theta]_{r=R} = \frac{\Delta T E \beta_T}{1-\nu} \tag{2.58}$$

where β_T is the linear coefficient of thermal expansion, usually about (10–15) $\times 10^{-6}$ C^{-1} for shale, E is Young's modulus, usually in the range 5–100 GPa for most deeper sedimentary rocks (lower porosity → higher stiffness), ΔT is the difference in temperature between the drilling fluid and the virgin rock temperature, and ν is

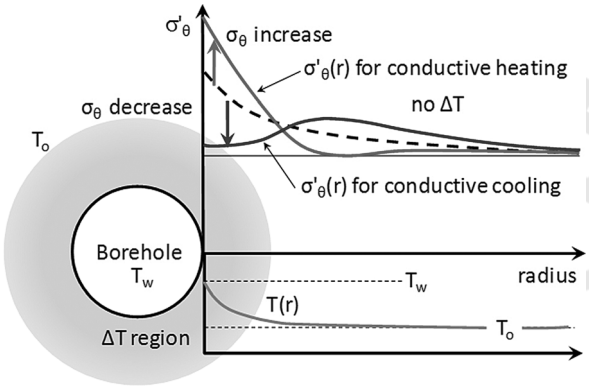

Figure 2.40 Tangential stresses near the borehole wall are dramatically altered if the drilling fluid temperature is changed. Heating leads to shear failure, cooling leads to stability.

Poisson's ratio. The change in tangential stress given by Equation 2.58 is only valid at the borehole wall; where it is usually supposed that conditions are the most critical.

2.4 Theories of Rock Breakage

The literature on rock drilling often includes such terms as "grinding", "wearing", "ripping", "ploughing", "cutting", "breaking", "shearing", "scraping", "fracturing", and "chipping". In this section, we will review various drilling methods with focuses on percussion drilling and rotary drilling.

2.4.1 Percussion Drilling

2.4.1.1 History

Developed by the Chinese more than 4000 years ago, percussion drilling basically involves raising and dropping heavy piercing tools to penetrate rocks. The Chinese used a cutting head secured to bamboo rods to drill to depths of 915 m. The raising and dropping of the bamboo drill string allowed it to impact and fracture the less dense rock formations. It was reported often to take two to three generations of workers to complete large wells (Treadway, 1997).

In 1859 at Titusville, PA, USA, Colonel F. L. Drake completed the first oil well using a cable tool percussion-type machine. One of the earliest reports of the percussion drilling technique occurred in 1949 (Harpst and Davis, 1949). Since then, different terms have been used, such as downhole hammer, percussion hammer, down-the-hole hammer, percussion drill, and percussion–rotary drill.

Major developments and research were reported between the 1950s and 1960s (Wanamaker, 1951; Fairhurst and Lacabanne, 1956; Topanelian, 1957; Fish, 1961;

Simon, 1964; Hartman, 1966; McGregor, 1967). Understanding of the percussion mechanism has been significantly improved in the laboratory. Some single-well applications have been reported in oilfields for the purpose of demonstrating the effectiveness of the percussion drill (Smith and Kopczynksi, 1961; Bates, 1964).

Mainly because of frequent mechanical failures, poor understanding and therefore control of drilling operations, and economic uncertainties, wide application of hammer drilling technology in oilfields was not reported until the 1980s. In 1987, Pratt reported that air hammers were tested on 27 wells in Alberta and British Columbia. The average time to total depth for recent air/mud-drilled wells at one location was 80 days (best 66 days), compared with rotary drills which took 103 days. Whiteley and England (1986) also showed the field application of the air hammer in the Arkoma basin, which significantly improved drilling operations including a large increase in *rate of penetration* (*ROP*), a substantial reduction in cost per foot, improved hole geometry, and reduced drillstring stresses.

Since the 1990s, wells have been drilled deeper and deeper to exploit hydrocarbon resources, and consequently drilled rocks become harder and harder. The hydraulic hammer or water hammer has been developed to accommodate these new challenges and efficient mechanical designs have been achieved (Kong, Marx, and Palten, 1996; Giles *et al*., 2001; Tibbitts *et al*., 2002). These designs, however, are still in the pre-field stage.

Throughout its history, the theoretical development of percussion drilling technology has relatively lagged behind, compared with the improvement in mechanical designs. This phenomenon is not uncommon in the drilling industry as the integrated process of rock drilling involves so many disciplines and complicated physics that rigorously modeling it faces prohibitive theoretical challenges.

2.4.1.2 Pros and Cons

It has been widely recognized that percussion drilling (even without rotary) could result in a faster penetration speed than conventional means such as the rotary drill or diamond drill, especially in some hard formations such as siliceous granite, sandstone, limestone and dolomite (Whiteley and England, 1986; Pratt, 1987). With the same rotation and weight on bit (*WOB*), the percussion–rotary method is 7.3 times faster than the conventional rotary method in a medium-hard granite, whereas under the best operational conditions for both methods, the percussion–rotary technique has a 2.3 times advantage in ROP over the rotary approach (Melamed *et al*., 2000).

The facilitation is mainly due to the effects of frequent blows and high-impact loads through the bit teeth, and chipping of rock from a clean surface with the bit rotation. Other advantages of percussion drilling are as follows{

- Static and lower WOB. For example, an ROP of $3.3\,\mathrm{m\,h^{-1}}$ was achieved with an $8^{3/4}$ inch bit when the WOB was 4.5 ton, whereas in the rotary drilling mode 18.5 ton WOB was needed to achieve the same ROP (Melamed *et al*., 2000).
- Less contact time with rock: only 1–2% of the total operational drilling time (Bates, 1964; Melamed *et al*., 2000) led to less abrasion of the bit and therefore a longer bit life.

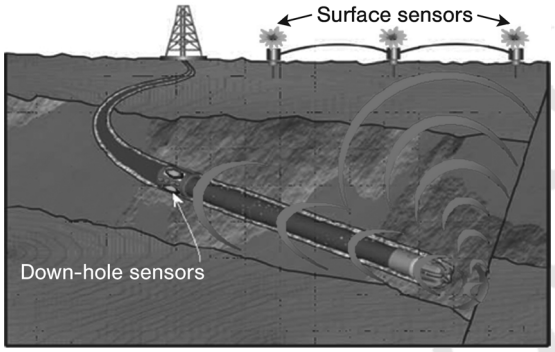

Figure 2.41 Percussion hammer seismic. After Pixton and Hall (2002). (Please find a color version of this figure on the color Plates).

- Less hole deviation and easier control of deviation problems for straight hole drilling.
- Larger cuttings may be generated, giving a better representation for geological study. However, large-sized chips may lead to hole cleaning problems in large fast-drilled holes (Pratt, 1987).
- Some potential applications of percussion drilling have been proposed. For example, the impact of the hammer may transmit mechanical impact waves to the rock through the drill bit, generate hydraulic pressure fluctuations in the borehole (Figure 2.41), and provide a steady seismic signal at the hole bottom. Vibrational energy can be in the 10–20 kHz range, which is used to estimate porosity, rock elastic moduli, and synthetic seismograms for comparison with surface seismic data (Minear, Heysse and Boonen, 1996). The hammer may also be used as a steerable drilling device that provides down-hole rotation (Bui, Meyers and Swadi, 1995), or be exploited for down-hole electricity generation, down-hole high-pressure jet intensification, and so on.

Because of these attractions, it has been predicted that "... The combination of rotary and percussion-type drilling could make a frontal attack into drilling technology and open a new era of drilling" (Samuel, 1996).

On the other hand, inclusive overall results, risks in operation (such as mechanical failure), and economic uncertainties greatly hinder the acceptance of percussion drilling technology, even though it has been a focus in rock drilling for a long time. There are many unclear but critical issues yet to be solved, such as unreliable estimation of optimized values for hammer type, number of blows, energy per blow (which is directly related to length of the stroke, area of piston, and pressure supplied), and wellbore stability issues associated with excessive hammer energy, poor performance in soft rocks, severe vibration to the drill string and the rig structure, and less field evidence of reliable and continuous operations of percussion hammers, compared with rotary drilling.

2.4.1.3 Physics of Rock Breakage in Percussion Drilling

Percussion drilling involves four fundamental processes: (1) the drillbit penetrates the rock with compression and vibration; (2) the rock receives the impact, stress

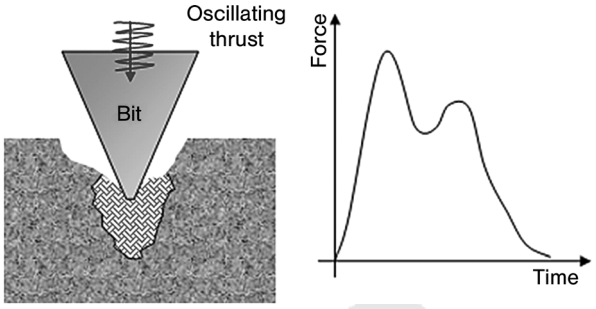

Figure 2.42 Illustration of a percussion drill and force response in bit.

propagates, and damage accumulates; (3) the rock fails and disaggregates; and (4) cuttings are transported away from the bit and up in the annulus. These are coupled physical processes, with different physics related to the tool and bit mechanics, rock mechanics, and cuttings transport mechanics.

Unlike conventional rotary drilling, where WOB first forces the bit cutters to penetrate the rock in the direction normal to the bit movement, and then the cutters shear off a conchoidal chip of the penetrated rock as the bit rotates, the percussion bit can generate much higher impact force along the direction of bit movement (Figure 2.42). When the force exceeds the rock strength, it crushes the rock below the bit and creates fractures forming a narrow wedge along the outer boundaries of the bit inserts. The cratered zone may extend to a depth several times greater than the actual depth of bit penetration.

2.4.1.3.1 **Dynamic Stress Generation and Propagation** There are limited dynamic stress data during bit–rock impact, especially close to the impact location. The photoelastic method was first applied to analyze the elastic stress behavior of rock under drilling loading conditions (Somerton, Timur and Gray, 1961; Reichmuth, 1963). Oscilloscope traces were then used to record rock displacement in a few milliseconds during an indention test (Podio and Gray, 1965). With improvements to instruments, high-frequency data from an impact steel rod were recorded in a recent indention test (Green *et al.*, 2005). Overcoming the difficulties in setting up the measurement device, the high impact force, high-frequency dynamic stress wave inside the rock was first recorded recently during hammer impact (Han, Bruno and Grant, 2006).

Figure 2.43 shows a schematic of single impact test performed on a single insert impact tester (Green *et al.*, 2005). The rock sample is loaded inside a pressure vessel and exposed to drilling mud under various pressures. A conical single cutter is located tightly against rock at a given preload. A steel anvil with the single insert attached at the bottom extends out of the pressure vessel and upwards through a hollow piston. A gas-driven piston is used to strike a shoulder on the anvil. This impact sends a compressive stress wave down the anvil, through the insert, and into the rock. Three measurements can be taken simultaneously: load in the steel rod (ILoad) measured by a load cell located outside the pressure vessel, displacement of

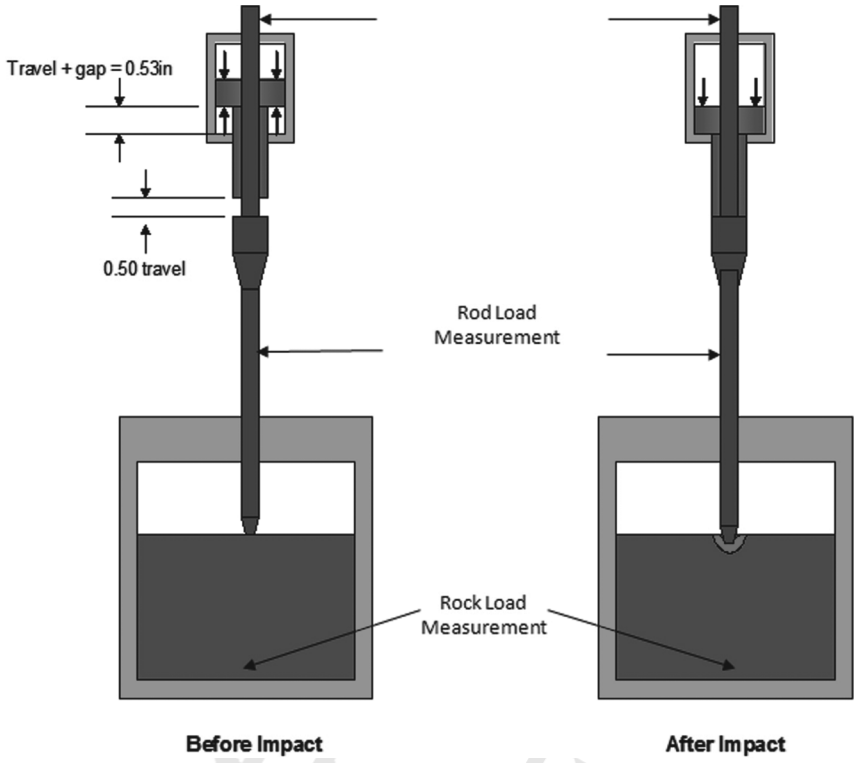

Figure 2.43 Schematic representation of test setup for single-impact tests (Han, Bruno and Grant, 2006). (Please find a color version of this figure on the color Plates).

the rod (IDispl) by a high-frequency, high-resolution laser measuring device on the upper end of the anvil, and load at the rock bottom by a rock load cell (RLoad) preloaded against rock bottom directly in line with the insert impact. Data are recorded at a high frequency of 91 kHz.

For a test with Berea sandstone exposed to air, the impact stress in the steel rod (IStress) and the dynamic stress in the rock (RStress) are plotted in Figure 2.44. The magnitude of the stress wave generated by the piston can reach as high as 120 kpsi (827.4 MPa) in the steel rod, oscillating at about 3 kHz frequency. After passing from the rod to the rock, the stress wave gradually loses its energy due to the rock damping effect (Han, Bruno and Dusseault, 2005b). After approximately 0.12 ms, the wave reaches the rock bottom, and the rock stress decreases to less than 1100 psi (7.6 MPa). Even though the loading stress in the rod diminishes after 0.01 s, the rock stress oscillates around 700 psi (4.8 MPa) because of the remaining gas pressure in the vessel.

Figure 2.45 illustrates the first stress wave in the rod, and also its displacement during the first cycle of the impact. Rod deformation first increases, levels off after the stress in the rod becomes tensional and continues to increase when the next cycle of compressive waves arrives.

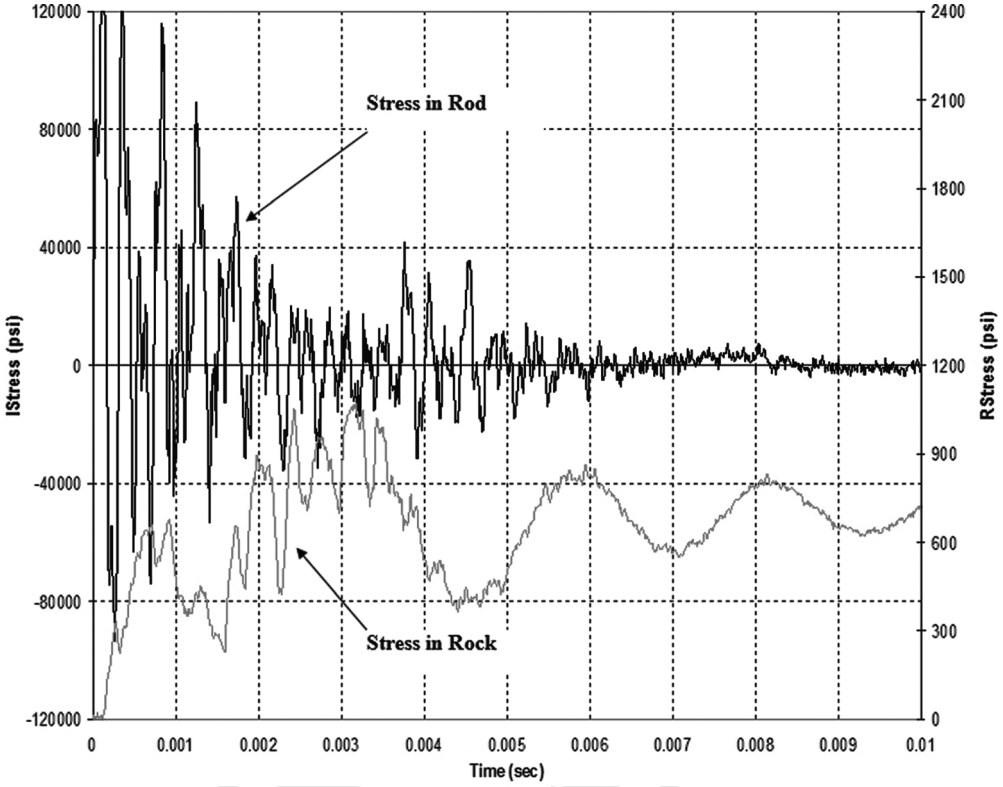

Figure 2.44 Compressive stresses recorded in the rod and the rock in a single-impact test with 0 psi confining stress and 0 psi pore pressure (Han, Bruno and Grant, 2006).

2.4.1.3.2 **Rock Damage and Defragmentation** When the insert impacts rock, some of the stress waves are transferred from the rod to the rock whereas the other waves are reflected and dissipated mechanically and thermally. Upon receiving impact, the rock deforms elastically when the impact stress is less than the rock strength. Once the loading stress is high enough, however, the rock starts to yield, fail, and disaggregate. Some examples of damaged rock from indention tests with different lithologies are shown in Figure 2.46.

To investigate the effect of repetitive percussion on rock penetration, three impacts are loaded sequentially on the same location on the rock surface. After each impact, the depth and width of the craters are measured, and debris is washed out so that a fresh rock surface can be exposed for the next impact. It is found that the repetitive percussion may affect rock penetration in different ways in different rocks. For Berea sandstone, the crater depth after each impact increases with the number of impacts, indicating that the rock becomes weaker due to cyclic loading (Han, Bruno and Dusseault, 2005b). For Mancos shale, however, the crater depth decreases with the number of impacts. Since the energy level of each impact is constant, this indicates

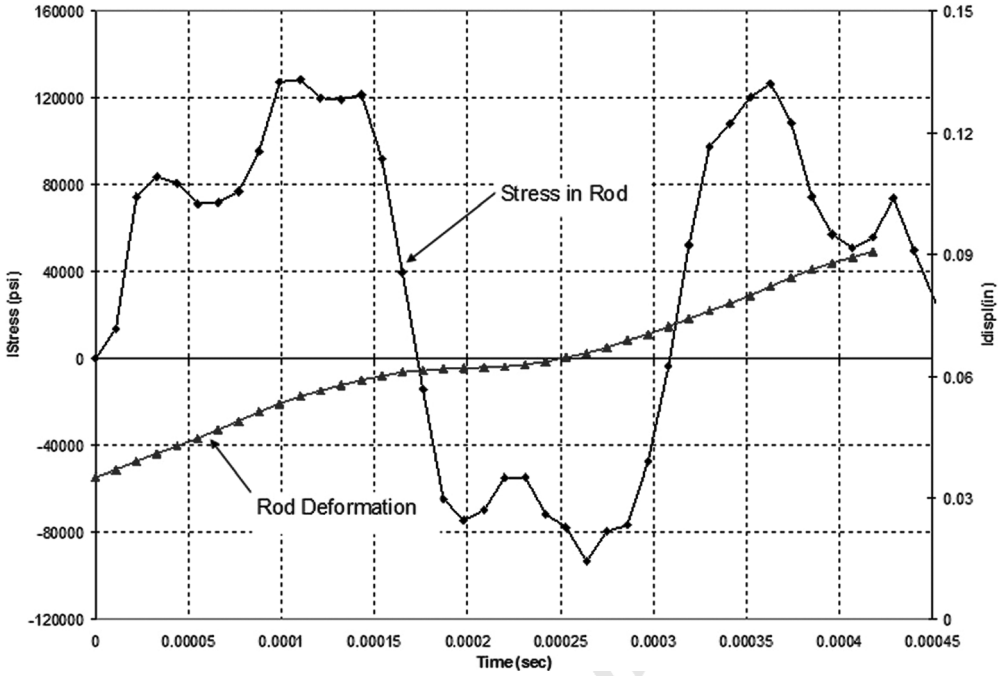

Figure 2.45 Compressive stress and displacement of the rod (Han, Bruno and Grant, 2006).

that the rock, instead of being weakened by repetitive loadings, actually becomes stronger than the original. The discrepancy may result from the difference in the rock structures. Berea sandstone is a porous (porosity 20%) and medium-strength rock (UCS = 6657 psi or 45.9 MPa). Sand particles can easily shift and rearrange themselves to accommodate the impacting energy. Therefore, micro-fissures are easily introduced when the particles shift and the rock becomes damaged. On the other hand, Mancos shale is a more compact (the porosity is only 7.9%) and highly layered rock with a higher strength (UCS = 8079 psi or 55.7 MPa). When the hammer impacts the shale, the shale particles are more restricted and are crushed into smaller powder instead of moving to a porous space. Crushed particles, as a new material with a smaller particle size, have greater strength and higher density than the original rock, which explains why Mancos shale becomes stronger after each loading.

These findings are one example that demonstrates the complexity of percussion drilling. Hammer performance is related not only to cutter and bit design and the percussion energy level that a hammer can create, but also to the mechanical properties, flow properties, and texture of the rock. Different rocks could have similar strength, but a hammer may perform very differently due to the difference in rock textures.

In addition to single indention tests, drilling tests on a similar scale to that used in oil and gas fields are also conducted. The testing facility could provide field downhole conditions such as high confining stress and high fluid pressure (Green *et al.*, 2005).

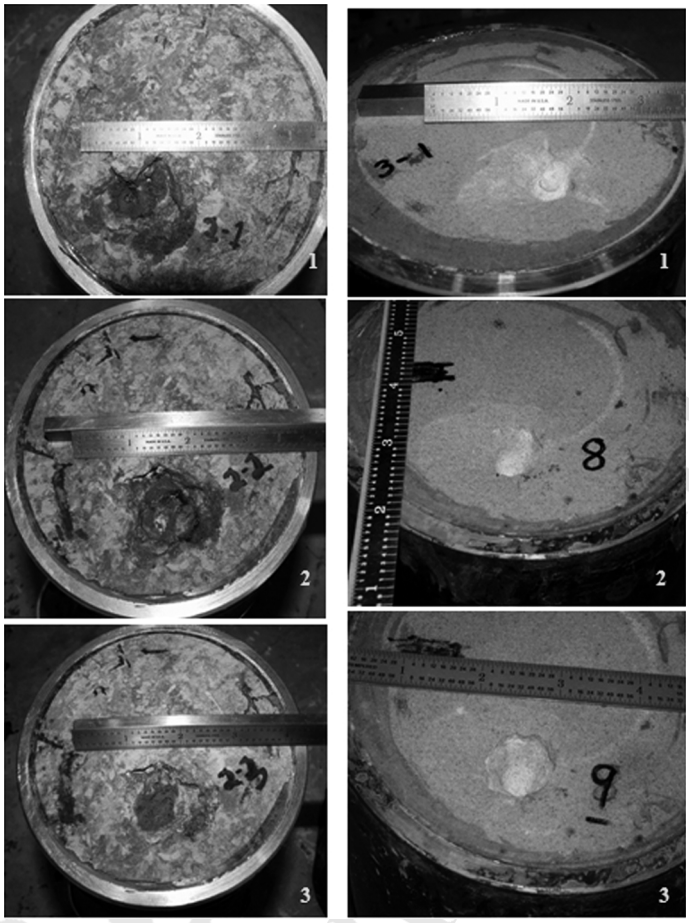

Figure 2.46 Indented rock samples after three impacts at the same location: (a) Mancos shale; (b) Berea sandstone (Han, Bruno and Grant, 2006).

During a test, as many as 16 drilling and fluid parameters can be recorded, such as penetration per revolution, torque, WOB, rotary speed, borehole pressure, flow rate, fluid temperature, overburden stress, and confining pressure. Data can be recorded at a frequency of 1 Hz, or at a high rate of 2000 Hz for a short period. Both Berea sandstones and Mancos shales are tested. Each sample is 15 in (39.4 cm) in diameter and 36 in (91.4 cm) in length. An industry mud hammer bit is applied to drill each sample under various bottom hole pressures.

Figure 2.47 illustrates the hammer, a drilled rock sample, and collected cuttings. To compare, the cuttings collected from a roller-cone drilling, a hammer drilling, and a penny coin are laid side by side. Even though the size of the cutting from the hammer bit is smaller than that from the roller-cone bit, it is as thin as a penny coin whereas the cuttings from the roller-cone bit are chunks. This may indicate

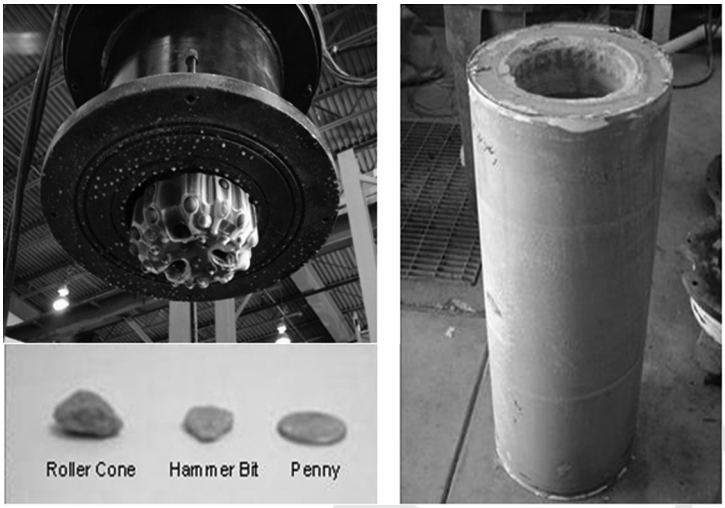

Figure 2.47 Mud hammer bit (a), drilled samples (b), and cuttings collected (c) in a full-scale hammer drilling test (Han, Bruno and Grant, 2006).

that different failure mechanisms are involved in each drilling method, as discussed below.

2.4.1.4 Rock Failure Mechanisms During Percussion Drilling

Before further discussion of rock failure, it is necessary to clarify two terms that are often misused: *rock yield* and *rock failure*. Yield refers to a process of accumulation of shear bands or microfissures developed as rock gradually starts to lose its ability to support load, whereas failure means collapse and total loss of strength.

During percussion drilling, rock failure develops at and near the impact location. Unfortunately, rock stress and deformation around the location are almost impossible to measure without damaging the device. Numerical simulations have been designed to help address rock fragmentation after receiving impacts (Han, Bruno and Lao, 2005a; Han, Bruno and Dusseault, 2005b; Han and Bruno, 2006). Rock failure could occur due to (1) excessive compression and crushing; (2) excessive shear stress and particle movement; (3) excessive tension and fracturing; and (4) cyclic loading and damage accumulation.

2.4.1.4.1 **Compressive Failure** A critical compressive strain is proposed to describe when rock crushes due to excessive compressional strain in the loading direction:

$$\varepsilon_{zz} > \bar{\varepsilon}_z \tag{2.59}$$

where ε_{zz} is the calculated compressional strain in the loading direction and $\bar{\varepsilon}_z$ is the critical strain value determined from laboratory testing (e.g., $\bar{\varepsilon}_z = 0.006$ for a Berea sandstone).

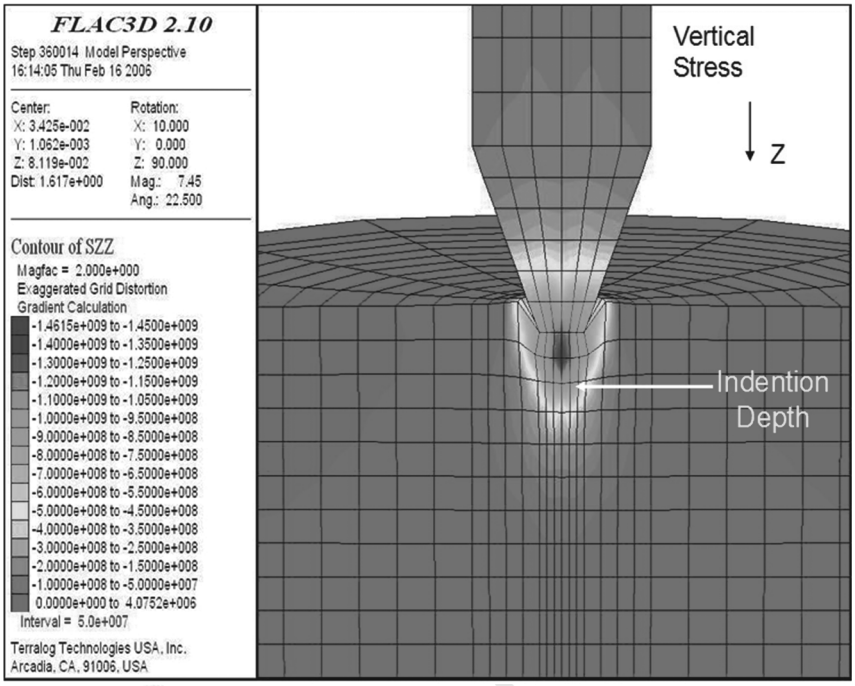

Figure 2.48 Vertical compressive stress during bit–rock impact (unit: Pa) (Han and Bruno, 2006). (Please find a color version of this figure on the color Plates).

High-impact stress passes from indentor to rock in a compressive nature. Figure 2.48 illustrates the distribution of compressive stress (in this case it is the vertical stress) in both the indentor and the rock adjacent to the impact point in a single indention test. The diameter of the impacting cone is 0.25 in (0.00 635 m). The small indentor head, along with the rigid indentor–rock interface, greatly increases the impact stress from its original 20 kpsi (137.9 MPa) at the stroked anvil to as high as 212 kpsi (1461.5 MPa) at the indentor tip. The measured indention depth is about 0.24 in (0.0061 m), which is well covered by a conical-shaped stress concentration zone (the blue and green elements in Figure 2.48).

In addition to the vertical compressive stress, the vertical strain along the impact direction is also studied in Figure 2.49. Clearly, a highly indented zone (colored in blue and dark green) is developed under the impact. This zone reaches well beyond the cutter penetration itself. It is the stress superposition under the cutter that helps rock failure extend as deep as several cutter diameters in hammer drilling. More interestingly, there are some zones (colored in red) showing opposite deformation: moving against the direction of the impact force. These elements are outside the conical compressive strain zone and in a state of tension.

2.4.1.4.2 **Tensile Failure** The fact that rock could fail in tension despite it having been compressively loaded in percussion drilling is not new (Fairhurst and

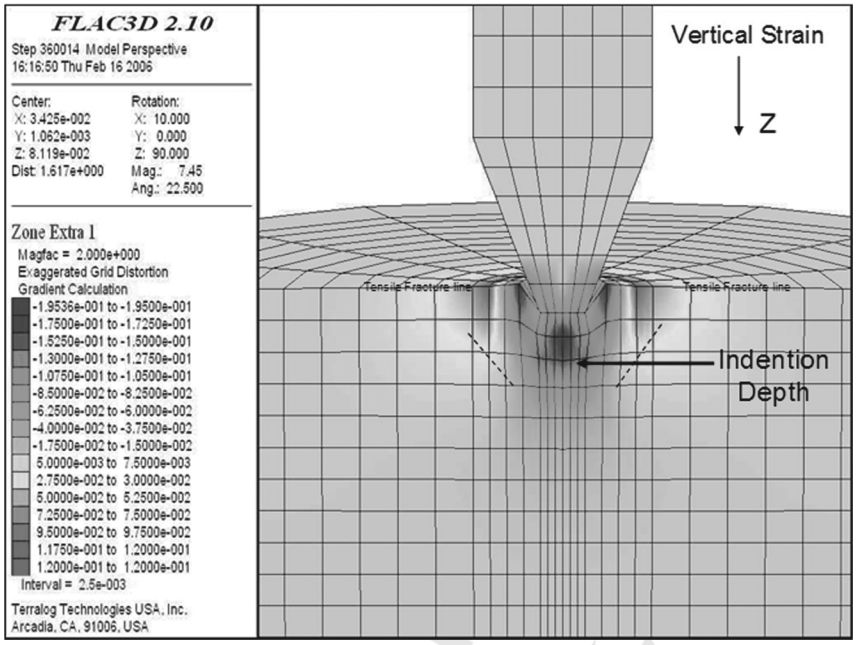

Figure 2.49 Vertical strain during bit–rock impact (Han and Bruno, 2006). (Please find a color version of this figure on the color Plates).

Lacabanne, 1956; Reichmuth, 1963; Paul and Gangal, 1969). It has been suggested that tensile fractures may be generated along the edges of the indentor (Fairhurst and Lacabanne, 1956). We find that tensile zones are formed outside the edge of the compressive zone, tipped towards the surface. Fractures may develop along the dotted lines in Figure 2.48 and the rock elements in tension could be removed.

Tensile failure is a more efficient rock failure mechanism because rock tensile strength is usually much less than rock compressive strength. The hole diameter measured in single indention tests could be easily seven times larger than the indention depth. With a rock surface exposed to the atmosphere, the fractured rock debris is easier to chip off. This becomes more evident in the full-scale hammer drilling tests. The ROP in underbalanced drilling conditions, where the *bottom hole pressure* (BHP) resulting from the weight of the drilling mud is lower than the rock pore pressure, was as high as 120 ft h^{-1} whereas it was only about 10 ft h^{-1} when the BHP was raised only 500 psi (3.45 MPa) over the pore pressure (Figure 2.52). Furthermore, the cuttings collected after the tests showed that flat, disk-shaped cuttings were generated instead of chunk cuttings by a tricone drill bit (Figure 2.47).

2.4.1.4.3 **Shear Failure** When rock is in shear, its peak strength can be defined by M–C criteria (Jaeger, Cook and Zimmerman, 2007):

$$\sigma_1' = \frac{1+\sin\varphi}{1-\sin\varphi}\sigma_3' + \frac{2\cos\varphi}{1-\sin\varphi}c_0 \tag{2.60}$$

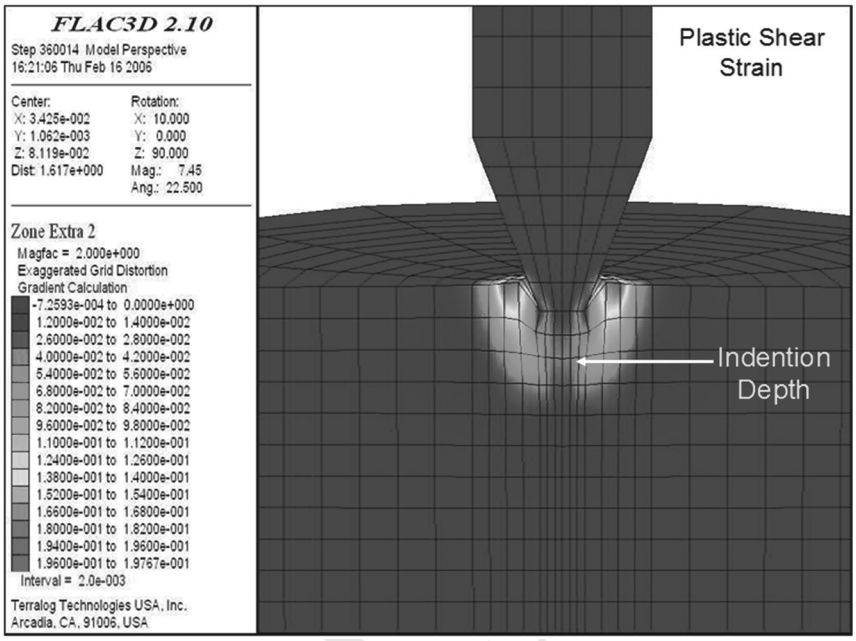

Figure 2.50 Plastic shear strain during bit–rock impact (Han and Bruno, 2006). (Please find a color version of this figure on the color Plates).

where σ_1' and σ_3' are maximum and minimum effective principal stresses, c_0 is cohesive strength, and φ is the friction angle.

High impact stress also induces abrupt movement among rock particles. When the vertical loading stress exceeds the strength defined in Equation 2.59, rock will break in shear mode. The plot of plastic shear strain is shown in Figure 2.50. Compared with the compressive deformation in Figure 2.49, where the highest compressional strain occurs right below the cutter, most shear deformation appears along the edge of the cutter, with the maximum showing at the rock surface.

2.4.1.4.4 **Rock Fatigue Due to Repetitive Impacts** Because hammer blows can be delivered at a rate up to 1500–3000 min^{-1} while the longitudinal wave velocity in drill-steel is around 5200 m s^{-1} (Roberts, 1981), the loading force on the rock oscillates dramatically, generated by the stress waves from both the initial blow and the reflected pulses along the drilling rod. Also, stress waves could be reflected if rock is heterogeneous and there are pre-existing layers and fractures. This leads to another possible important mechanism for rock failure during percussion drilling: rock fatigue due to cyclic loading.

Haimson (1978) investigated the effects of cyclic loading on rock deformation and strength with experiments on four different hard rocks, including Tennessee marble, Indiana limestone, Berea sandstone, and Westerly granite. Four types of loadings were studied: uniaxial compression, uniaxial tension, triaxial compression, and

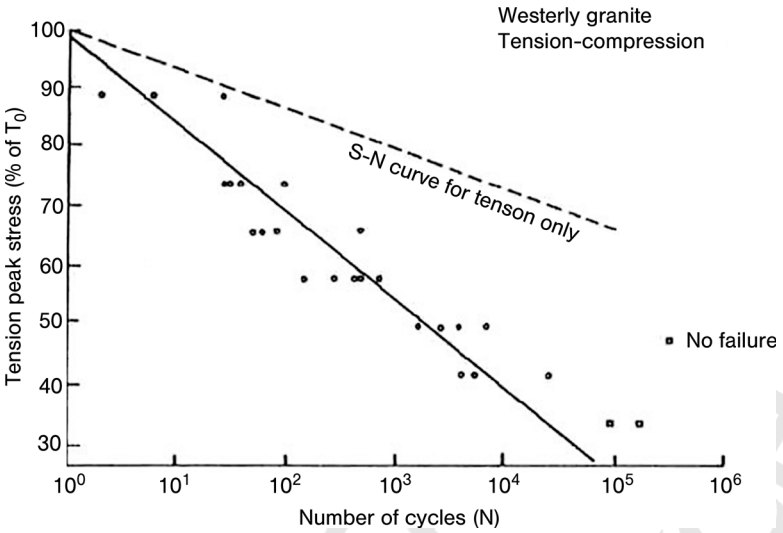

Figure 2.51 Cyclic fatigue of a granite in a uniaxial tension–compression test (after Haimson, 1978).

uniaxial tension–compression. In general, it is clear that repetitive loading of any type can weaken rock strength and result in premature rock failure. For example,

- In uniaxial tension and in uniaxial compression, the strength left after 10^5 cycles of cyclic loading is 60–80% of the respective UCS.
- Rock damage is the most severe in uniaxial tension–compression mode. The strength lost can be as high as 75% of UCS (Figure 2.51). After each cycle there is also a sharp drop in the elastic modulus as the load shifts from compression to tension.

Because the loading force in percussion drilling is essentially uniaxial compression that repetitively increases and decreases, the loaded rock is consistently, in turn, in a compression–tension state.

Acoustic emission and specimen photo-micrography suggest microfracturing as the principal mechanism of fatigue failure. If the peak loading stress reaches 75% of the rock maximum strength, the decrease in rock strength with cycles of loading could be expressed as (Ewy *et al.*, 2004):

$$\frac{\sigma}{\sigma_i} = aN^b \tag{2.61}$$

where N is number of cycles and σ/σ_i is the ratio of rock peak strength to initial strength. The coefficients a and b are derived from laboratory tests. They vary with different types of rocks.

2.4.1.4.5 **Effect of Pore Pressure and Bottom Hole Pressure** Due to the introduction of drilling fluids, the BHP may be different from the formation fluid pressure, also known as pore pressure of rock. For a long time, laboratory tests and field

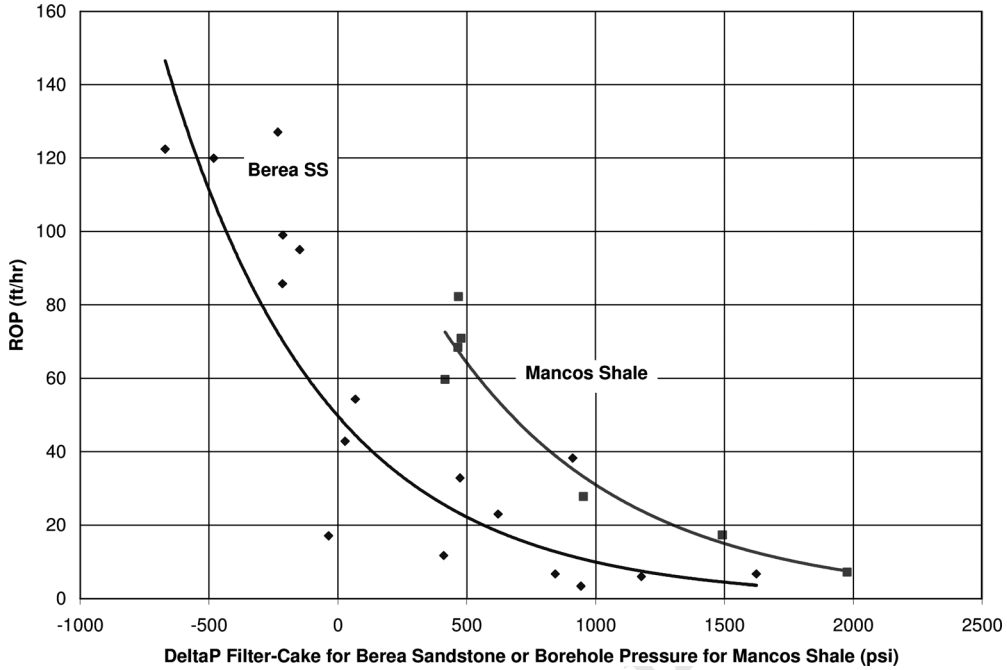

Figure 2.52 Recorded ROP reduction in full-scale hammer tests with various pressure differences across rock surfaces of a Berea sandstone and a Mancos shale (Han, Bruno and Grant, 2006).

applications have witnessed the effect of pressure differences across the rock surface on drilling performance, especially in rotary drilling (e.g., Deily and Durelli, 1958). The pressure difference between BHP and pore pressure could be positive (overbalanced), or negative (underbalanced)£. A higher positive pressure difference usually leads to slower bit penetration. Some rotary drilling tests have shown that ROP may decrease by as much as 80% at high borehole pressures, compared with atmospheric drilling results (Cheatham, 1977). Others have shown that an increase in the absolute value of either BHP or pore pressure hardly changes the bit penetration: it is the difference between the BHP and pore pressure of the rock that considerably affects bit penetration (Cunningham and Eenink, 1959; Warren and Smith, 1985). The crater volume, however, remains constant (Maurer, 1965) or increases slightly (Yang and Gray, 1967) if only the horizontal stress parallel to the bottom surface is increased while the difference between BHP and pore pressure is held constant.

Similar effects have also been observed during single cutter impact tests (Green *et al.*, 2005) and hammer drilling as shown in Figure 2.52.

There have been several speculations on the mechanisms for ROP reduction with the pressure difference in rotary drilling, such as the effective loading stress decreases as a result of an increase of BHP, or a higher confining stress around the rock results in a higher rock compressive strength. The chip-shaped cuttings

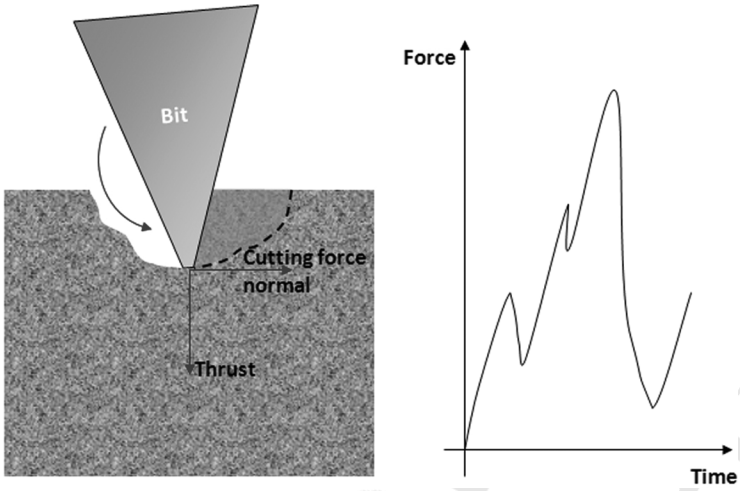

Figure 2.53 Illustration of a rotary drill and force response in bit.

collected in full-scale hammer drilling (Figure 2.53) indicate that the ROP variation is closely related to the tensile failure that occurs during bit–rock impact and thereafter. The tensile strength of rock is much less than its compressive strength, and therefore rock could fail more easily in tension than in compression. When there is little pressure difference between BHP and pore pressure compressing the rock surface, the restraint of rock tensile failure is minimized. Rock could fail in tension not only during bit–rock impact but also when the bit retreats and the impact wave starts to reflect as it passes through heterogeneous rock. In this respect, a certain type of percussion drilling is almost always better performed through encouraging rock tensile failure, such as with an air hammer (the pressure difference is close to zero) or underbalanced drilling (the pressure difference is negative).

2.4.1.5 Effect of Cutter Shapes and Interactions

The effect of different cutter shapes on the penetration into brittle rock has been intensively studied. For example, Paul and Sikarskie (1965) developed a static-wedge penetration model, based on the C–M failure theory. This model provides a macroscopic criterion for brittle failure when the rock is under a confined pressure below the brittle-to-ductile transition pressure. In percussion/vibratory drills, the teeth are located at the cutting edge and their characteristics and interactions are critical to the drilling rate.

To determine the effect of adjacent teeth and account for their interactions, Liu *et al.* (2007) developed an analytical model that extended the wedge penetration theory to express the overall specific energy as a function of the cutter's spacing and teeth number. Both their theoretical models and laboratory tests indicated that, for coring bits with wedge-shaped cutting teeth of vibratory drills, there exists an optimal spacing/depth ratio or an optimal teeth number that minimize the coring bit specific energy and hence maximize its drilling rate.

2.4.2 Rotary Drilling

In conventional rotary drilling, as shown in Figure 2.53, WOB first forces the drill bit cutters to penetrate into the rock in the direction normal to the bit movement. Then, the cutters shear off a conchoidal chip of the penetrated rock as the bit rotates. There are two requirements for a rotary drill to advance through the rock: first, WOB must be high enough to press the cutters into the rock; and second, the cutters must generate and localize enough shear stress through bit rotation to break the rock.

2.4.2.1 Rotary Drilling with Drag Bits

This section summarizes a model of the drilling response for drag bits (Detournay and Defourny, 1992; Detournay, Richard and Shepherd, 2008), that is, a set of relations between the WOB, W, the torque-on-bit, T, the rate of penetration, V, and the angular velocity, Ω, that characterize the nature of the boundary conditions at the bit–rock interface, and some experimental validation of this model. Fixed-cutter bits or drag bits have been used in rotary drilling since about 1900 (Besson *et al.*, 2000). These bits initially consisted of steel blades and were reserved for the drilling of soft and shallow formations, because of their limited resistance to wear. However, the production of synthetic *polycrystalline diamond compacts* (PDC) and the development of a technology to bond the PDC to tungsten carbide in the early 1970s led to the introduction of the modern fixed-cutter bits. The PDC bits, as they are often referred to, consist of individual PDC cutters that are mounted on a steel or tungsten carbide matrix body and are generally grouped into blades.

The PDC bit response model is restricted to the normal drilling mode, when the bit is drilling straight ahead with the bit velocity parallel to its axis of revolution and without any angular motion other than rotation around its axis of symmetry. In contrast, bit penetration into rock for the most general mode of bit–rock interaction (relevant for directional drilling) is characterized also by a lateral and an angular component in addition to an axial component (Ho, 1987). The model of bit–rock interaction summarized here distinguishes three successive regimes in the drilling response of PDC bits: (i) phase I, at low depth of cut per revolution, characterized by a dominance of the frictional contact process and by an increase in the contact forces with d; (ii) phase II, where the contact forces are fully mobilized; and (iii) phase III, where the actual contact length increases beyond ℓ, due to poor cleaning. In contrast to models that rely on a precise description of the bit cutting structure layout (Warren and Armagost, 1988; Sinor and Warren, 1989), the effect of the detailed geometry of the bit is here lumped into a few parameters.

2.4.2.1.1 **Rate Independent Interface Laws** The drilling response model for the normal mode consists of a set of relationships between W, T, V, and Ω. The kinematic variables V and Ω are conjugate to the dynamic variables W and T, respectively; that is, P, the rate of energy dissipation at the bit–rock interface, is given by

$$P = WV + T\Omega \tag{2.62}$$

where W and T are taken as positive when pointing in the same direction as V and Ω, respectively. Provided that the state variables are averaged over at least one revolution, the interface laws that relate the dynamic to the kinematic variables are generally of the form

$$W = W(V, \Omega), \quad T = T(V, \Omega) \tag{2.63}$$

meaning that the forces on the bit, W and T, depend only on the instantaneous (but suitably time-averaged) velocities, V and Ω.

While field and laboratory measurements exist (Black *et al.*, 1986; Brett, 1992) that suggest an intrinsic dependence of the torque T on the angular velocity Ω, it has recently been argued that the observed rate dependence is in fact a consequence of the axial vibrations experienced by the drill bit during drilling, and that the apparent rate effects are actually a function of the dynamic characteristics of the drilling system (Richard, Germay and Detournay, 2007). We will assume here that the interface laws are independent of rate. This assumption is supported by experimental evidence obtained from single cutter and drilling tests conducted under kinematic control (Deliac, 1986; Richard, Germay and Detournay, 2007; Dagrain, Richard and Detournay, 2008). Under the assumptions that the processes taking place at the interface between the bit and the rock are independent of rate, the drilling response can be described by relations involving only three quantities: W, T, and the ratio V/Ω:

$$W = \tilde{W}(V/\Omega), \quad T = \tilde{T}(V/\Omega) \tag{2.64}$$

The rate-independent bit–rock interface laws will be expressed in terms of two dynamic quantities, a scaled weight w and torque t, and on the depth of cut per revolution d, which is proportional to the velocity ratio V/Ω. From now on, we simply refer to weight-on-bit and torque-on-bit as weight and torque, respectively. These three basic state variables are defined as

$$w = \frac{W}{a}, \quad t = \frac{2T}{a^2}, \quad d = \frac{2\pi V}{\Omega}$$

where a is the bit radius. Scaling of the weight and torque removes the influence of the bit dimension from the interface laws. The scaled quantities w and t, which have dimensions force/length (a convenient unit is the $\mathrm{N\,mm^{-1}}$), can conveniently be interpreted as the normal and shear force per unit length on a two-dimensional cutter removing material over a depth of cut d (Figure 2.54).

2.4.2.1.2 **Cutting and Frictional Contact Processes** It is further postulated that two independent processes, cutting and frictional contact, characterize the bit–rock interaction. The torque t and weight w can thus be decomposed as

$$t = t_c + t_f, \quad w = w_c + w_f \tag{2.65}$$

where the subscript c denotes the cutting components of w and t, and f the contact components. Figure 2.55 illustrates the decomposition of the total forces (t, w) into forces transmitted by the cutting face (t_c, w_c) and by the wear flat (t_f, w_f), using the conceptual representation of an equivalent cutter.

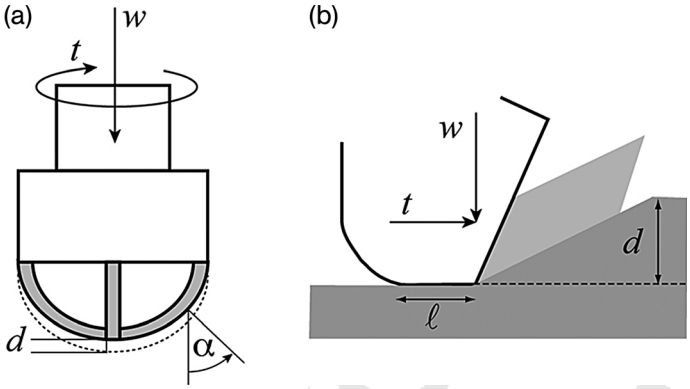

Figure 2.54 (a) Sketch of a drag bit showing the WOB *w*, torque-on-bit *t*, and depth of cut per revolution *d*; (b) sketch of the equivalent two-dimensional cutter showing the tangential force *t*, the normal force *w*, and the depth of cut *d* (Detournay, Richard and Shepherd, 2008).

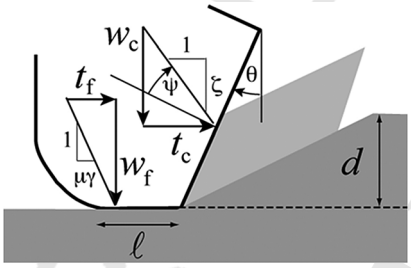

Figure 2.55 Decomposition of the total forces (*t*, *w*) into forces transmitted by the cutting face (t_c, w_c) and by the wear flat (t_f, w_f) (Detournay, Richard and Shepherd, 2008).

2.4.2.1.3 **Cutting Process** The cutting components t_c and w_c are related to the depth of cut d according to (Figure 2.56)

$$t_c = \varepsilon d, \quad w_c = \zeta \varepsilon d \tag{2.66}$$

where ε is the intrinsic specific energy, a quantity with dimensions of stress, and ζ is a number that is typically in the range 0.5–0.8. These two constants characterize the cutting process. The adjective "intrinsic" is introduced to differentiate ε from the specific energy *E*, defined below, which depends not only on the wear state of the bit, but also on the depth of cut. The intrinsic specific energy represents the energy required to remove a unit volume of rock by an ideally sharp bit under given field conditions (Detournay and Defourny, 1992). In fact, ε depends not only on the rock strength (Dagrain, Richard and Detournay, 2008) and on the bottom hole pressure and local pore pressure (Detournay and Atkinson, 2000), but also on the back-rake angle θ of the cutters. However, single cutter experiments (Richard, 1999) indicate that the dependence of the intrinsic specific energy ε on θ is very weak over the range 10–20°,

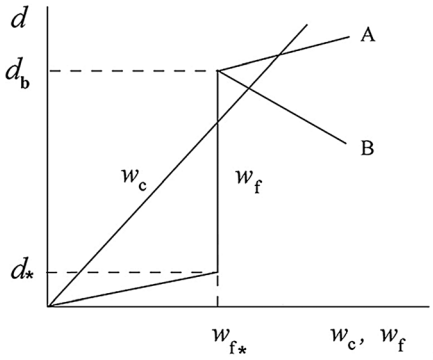

Figure 2.56 Conceptual response of the bit in the w_c–d and w_f–d spaces (Detournay, Richard and Shepherd, 2008).

which typifies the back-rake angle of most cutters mounted on drag bits. Hence for all practical purposes, ε depends only on the rock and on the pressure environment and not on the bit type and its wear state; this justifies the use of the term "intrinsic". Although it is possible to write $\zeta = \tan(\theta + \psi)$, with ψ denoting the angle between the normal to the cutter face and the cutting force, it should be noted that ψ cannot be interpreted as a friction angle independent of θ. Indeed, single cutter experiments (Richard, 1999; Dagrain, Richard and Detournay, 2008) and numerical simulations (Detournay and Drescher, 1992; Huang, Detournay and Bellier, 1999; Huang and Detournay, 2008) have indicated the existence of a complex flow process in front of the cutter, which is reflected by a dependence of the angle ψ on θ.

2.4.2.1.4 **Frictional Contact Process** Our understanding of the frictional contact process is not complete at the time of this writing. However, it is possible to describe with reasonable confidence the dependence of both the contact components of the torque and weight on the depth of cut d. Three phases appear to exist with increasing d, corresponding to an increase in the contact forces, a saturation, and another increase in the contact forces associated with poor cleaning (see Figure 2.56, which illustrates the assumed evolution of w_f with increasing depth of cut d).

First, we introduce the bit characteristic contact length ℓ, which is defined as the ratio $\ell = A_f/a$, where A_f denotes the combined area of the projection of the cutter wear flat surfaces on to a plane orthogonal to the axis of revolution of the bit. This contact length ℓ is an objective measure of the bit bluntness. Experimental evidence suggests that new or sharp bits are typically characterized by a value of ℓ less than 1 mm. In blunt bits, ℓ can increase beyond 10 mm. There is also a limiting value to the normal stress that can be transmitted by the wear flat. This limiting value will be denoted σ and will be referred to as the contact strength. The contact strength reflects the existence of a contained plastic flow process underneath the cutter wear flat, and thus will generally depend on the elastic modulus and strength parameters of the rock. Depending on rock and the pressure environment, σ can vary from a few to several hundred MPa.

In the phase I drilling regime ($w_f < w_{f*}$), the contact component of the weight, w_f, increases linearly with the depth of cut d:

$$w_f = \sigma\kappa d \tag{2.67}$$

It is conjectured that the increase in the contact force is predominantly due to a geometric effect, as the two contacting surfaces are generally non-conforming. A change in the depth of cut d indeed affects the angle between the two contacting surfaces, thus causing a variation of the actual contact area (the inclination of the rock surface in the tangential direction is parallel to the cutter velocity, whose vertical component is proportional to d). If the increase in w_f with d is entirely due to a geometric effect, then κ represents the rate of change of the contact length with d. Single cutter experiments indicate that κ is a number typically in the range 1–10 (Detournay and Defourny, 1992; Nishimatsu, 1993; Detournay and Richard, 2008).

In phase II ($w_f = w_{f*}$), the contact forces are fully mobilized. Beyond a critical value of the depth of cut per revolution d^* (function of the bit bluntness ℓ), the contact forces no longer increase because the normal contact stress has reached a maximum value σ, and the actual contact length has attained a limiting value that characterizes the bit bluntness. This drilling regime is thus defined by $w_f = w_{f*} = \ell\sigma$, with the consequence that any increase in the weight w must necessarily be translated as an increase in the cutting component w_c. In phase II, the bit behaves incrementally as a sharp bit.

Finally, in phase III, the contact surface increases, through pile-up of sheared rock material between the bit and the rock, caused by poor cleaning (the product of cutting exceeds what can be removed by the flow of mud). Because of this increase in the contact area, w_f becomes larger than w_{f*}. The threshold for phase III is taken here to correspond to a critical value of the depth of cut per revolution, d_b, which can, however, be a function of the bit geometry, mud flow rate, mud properties, and properties of the rock being drilled. Furthermore, the variation of w_f with d in phase III depends on a variety of factors, which precludes the existence of a contact law in this phase.

The contact components of torque and weight are assumed to be always constrained by a frictional relation:

$$t_f = \mu\gamma w_f \tag{2.68}$$

where μ is the coefficient of friction at the wear flat/rock interface and γ a "bit constant,, which encapsulates the influence of the orientation and distribution of the contact forces acting on the bit. The coefficient of friction μ was conjectured earlier (Detournay and Defourny, 1992) to reflect the internal friction angle of the rock φ, that is,

$$\mu = \tan\varphi \tag{2.69}$$

Extensive single cutter experiments on different rocks (Almenara and Detournay, 1992; Lhomme, 1999; Dagrain, 2006) have indeed confirmed that the friction angle at the wear flat/rock interface, assessed from the slope of the friction line in the E–S diagram (discussed below), is remarkably close to the internal friction angle, estimated from triaxial experiments at confining stress level comparable to the uniaxial compressive strength. Similarity between these two friction angles is due to the existence of

a boundary layer of failed rock below the cutter wear flat, where the shear flow takes place (Detournay and Defourny, 1992; Lhomme, 1999; Dagrain, 2006).

The bit constant γ depends on the orientation and distribution of the contact forces acting on the bit, both of which are strongly influenced by the bit design. A simple estimate of γ can be obtained for conditions that have been identified above as phase II drilling. This is indeed a situation where the contact length has reached its characteristic value ℓ and the normal contact stress has attained its limiting value σ, and thus $w_f = w_{f*} = \ell\sigma$.

The scaled torque transmitted through the contact surfaces, t_f, is sensitive both to the orientation of the contact surfaces and to the manner in which the contact length ℓ is distributed radially across the bit (it is assumed that the stress vector transmitted at the rock–wear flat interface is contained in the plane defined by the normal to the contact and the cutter velocity vector). To calculate t_f, we introduce the radial contact length density λ, a function of the radial distance r from the bit axis. Hence, we can express $\mathrm{d}\ell(r)$, the contact length associated with (parts of) the cutters inside the ring located between distance r and $r + \mathrm{d}r$ from the bit axis, as $\lambda(r)\mathrm{d}r$, and thus

$$\ell = \int_0^a \lambda(r)\mathrm{d}r \tag{2.70}$$

The contact component of the torque is then given by

$$t_f = 2\mu\sigma \int_0^a \frac{\lambda(r)r\mathrm{d}r}{\cos\alpha(r)} \tag{2.71}$$

where α is the angle between the normal to the contact surface and the bit axis. On the majority of bits, the cutting edge is curved, and hence α is a function of the distance between the cutter and the bit axis (Figure 2.53). In view of Equation 2.68 with $w_f = \ell\sigma$, and Equation 2.71, the expression for the bit constant γ becomes

$$\gamma = \frac{2}{\ell}\int_0^1 \frac{\lambda(r)r\mathrm{d}r}{\cos\alpha(r)} \tag{2.72}$$

This expression for γ has been confirmed experimentally with simple fishtail bits (Detournay, Richard and Shepherd, 2008).

2.4.2.2 Linear Constraint on the Drilling Response

2.4.2.2.1 Relationship Between Weight, Torque, and Depth of Cut Combining Equations 2.65, 2.66, 2.67, and 2.68 leads to a linear relation between w, t, and d

$$t = \mu\gamma w + E_0 d \tag{2.73}$$

where

$$E_0 = (1-\beta)\varepsilon, \quad \beta = \mu\gamma\zeta \tag{2.74}$$

Equation 2.73 represents a linear constraint on the response of PDC bits in terms of the three basic variables w, t, and d; it must be met irrespective of the

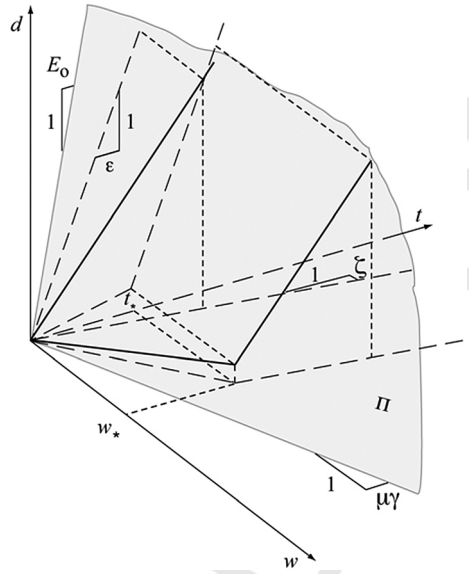

Figure 2.57 Three-dimensional representation of the PDC bit model in the (w, t, d) space for a sharp and blunt bit (with phases I and II). The plane $\prod$ represents a constraint on the bit response (Detournay, Richard and Shepherd, 2008).

state of wear of the bit and the magnitude of the contact forces. The geometric representation of Equation 2.73 is the plane Π in the (w, t, d) space as shown in Figure 2.57, which further illustrates the response of a sharp and blunt bit. A geometric interpretation of the parameters ε, E_0, ζ, and $\mu\gamma$ can also be found in Figure 2.57.

The parameter E_0 takes a particular meaning when considering the response of a bit under constant weight. According to Equation 2.73, such a response must lie on the line of slope E_0 and ordinate intercept $\mu\gamma w$ in a plot of the scaled torque t versus the depth of cut d (Figure 2.61) for the case $\beta < 1$. Also represented in this figure is the cutting line passing through the origin and inclined on the d-axis with a slope ε; the cutting line reflects the response of a perfectly sharp bit for which the torque and depth of cut per revolution are both proportional to the WOB. Introduction of the cutting line permits the decomposition of the torque into a cutting and a frictional component, and consequently a natural definition of the drilling efficiency η as from $\eta = t_c/t$.

It is obvious that moving from left to right on the constant WOB line is associated with an increasing efficiency: $\eta = 0$ on the torque axis where all the torque is dissipated in frictional processes and $\eta = 1$ on the cutting line (in this diagram, a constant efficiency is represented by a line through the origin). We finally remark that, under the constant WOB constraint, lower efficiency implies a decrease in the torque if $\beta < 1$ and the opposite if $\beta > 1$.

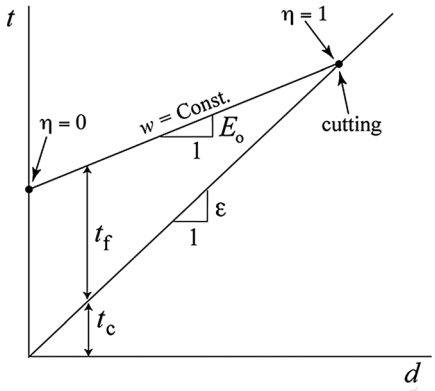

Figure 2.58 Constant weight w. Plot of torque t versus depth of cut per revolution d ($\beta < 1$) (Detournay and Defourny, 1992).

2.4.2.2.2 ***E–S* Diagram** The linear constraint (2.73) can equivalently be written as

$$E = E_0 + \mu\gamma S, \quad E \geq \varepsilon \tag{2.75}$$

where E is the specific energy and S the drilling strength, defined as

$$E = t/d, \quad S = w/d \tag{2.76}$$

Both E and S have dimensions of stress; a convenient unit is MPa (numerically equivalent to J cm^{-3}).

Equation 2.75 is represented by the friction line of slope $\mu\gamma$ in the E–S diagram (Figures 2.58 and 2.59). In this representation, E_0 is simply the intercept of the friction line with the E-axis. The cutting point, characterized by $E = \varepsilon$ and $S = \zeta\varepsilon$, corresponds to an ideally efficient drilling process, where all the energy provided to the bit is transferred into the cutting process. The cutting point is at the intersection of the friction line with the cutting locus, the line passing through the origin of the plane

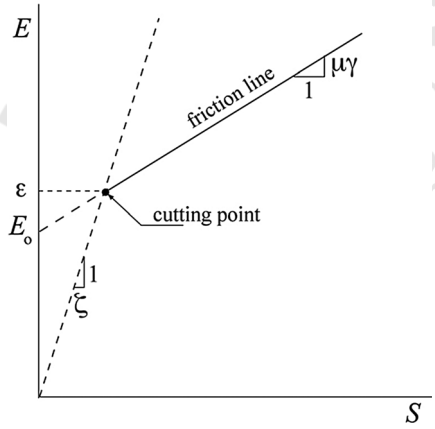

Figure 2.59 Schematic E–S diagram (Detournay and Defourny, 1992).

and inclined by ζ^{-1} to the S-axis. Admissible states of the drilling response of a PDC bit in the E–S diagram are represented by all the points on the friction line, which lies to the right of (and above) the cutting point.

Consider a horizontal line passing through the cutting point. The vertical distance between that line and a point on the friction line represents the component of the specific energy which is dissipated in frictional processes. The drilling efficiency η can thus alternatively be defined as ε/E. It is also convenient to introduce the quantity χ, defined as the ratio of the specific energy to the drilling strength, that is, $\chi = E/S$. A simple relation exists between χ and the efficiency η:

$$\eta = \frac{\chi - \mu\gamma}{(1-\beta)\chi} \tag{2.77}$$

The parameter χ varies between ζ^{-1} and $\mu\gamma$ as the efficiency η decreases from 1 to 0.

Note finally that an increase in the mud pressure p_b (all other conditions remaining the same) will cause the cutting point to move up the cutting locus, displacing with it the friction line, as the intrinsic specific energy ε is the only parameter that depends significantly on p_b.

2.4.2.2.3 **Experimental Evidence for the Existence of a Linear Constraint** Published results of a series of full-scale laboratory drilling experiments, carried out in a Mancos shale with a step-type 8.5 in diameter PDC bit for various combinations of imposed Ω and W ($W = 40$, 80, and 120 kN and Ω varying between 50 and 900 rpm) (Black *et al.*, 1986) can readily be analyzed within the above framework. [Results of tests performed at $W = 20$ kN were also reported by Black *et al.* (1986), but are not included in this discussion for reasons discussed by Detournay and Defourny (1992)].

The overall response of the laboratory tests is summarized in the E-S diagram shown in Figure 2.60. The points are coded in terms of the WOB W. A linear regression on the reduced data set gives the following estimates: $E_0 = 150$ MPa and

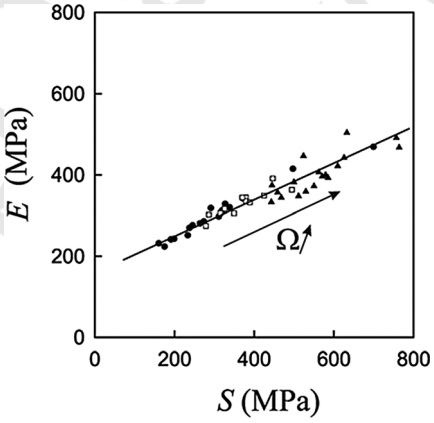

Figure 2.60 E-S diagram, according to published experimental data (Black *et al.*, 1986) with (▲) $W = 40$ kN, (□) $W = 80$ kN, and (●) $W = 120$ kN].

$\mu\gamma = 0.48$. Assuming that the bit constant $\gamma = 1$, the friction angle is approximately 26° (i.e., $\mu = \tan\varphi$). This value should be considered as an upper bound of the internal friction angle of the Mancos shale (published values of φ, deduced from conventional triaxial tests, are in the range 20–22°). The intercept of the friction line with the E-axis, E_0, represents a lower bound of the intrinsic specific energy ε; an upper bound of ε is given by the ordinate of the "lower-left" (LL) point of the data cluster. The LL point is characterized here by $E = 230$ MPa and $S = 160$ MPa, and thus by a ratio $\chi = 1.44$. This point is likely to be close to the optimal cutting point on the grounds that (i) the bit is new and (ii) the value of χ is fairly high. Thus here the cutting parameters are estimated to be: $\varepsilon = 230$ MPa and $\zeta = 0.69$.

It can be observed from the coding of the points on the E–S plot that the drilling efficiency increases with the WOB in these series of tests. The original data also indicate that the efficiency decreases with increasing rotational speed of the bit. Clearly, all the experimental data lie along the same line regardless of the angular velocity. Therefore, neither the intrinsic specific energy ε nor the apparent friction coefficient $\mu\gamma$ between the bit and the rock varies with the angular velocity. However, the dispersion along the friction line is large; the points representative of the bit response move upwards along the friction line with increasing angular velocity, under constant WOB. Furthermore, as can be seen in Figure 2.61, the mean torque decreases with increasing Ω under constant W, consistent with a value of $\beta < 1$ ($\beta = 0.35$), but in apparent contradiction with the assumption of rate independence of the interface laws.

The diminishing efficiency η with larger Ω under constant W reflects an increase in the contact forces at the expense of the forces mobilized by the cutting process. Assuming permanent contact between the bit flat and the rock, σ would have to increase with the relative velocity between the wearflat and the rock. Although such a law cannot be ruled out a priori, no significant effect of the cutting velocity on the

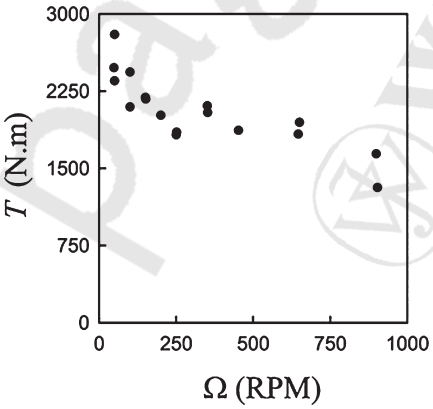

Figure 2.61 Evolution of the mean torque $\langle T \rangle$ with the angular velocity Ω_0 under constant WOB ($W = 120$ kN), according to published experimental data (Black *et al.*, 1986;Richard, Germay and Detournay, 2007).

forces has been reported in the literature. However, the mean contact stress could increase with Ω if axial vibrations responsible for an intermittent loss of contact between the bit and the rock progressively decrease in intensity with Ω. Such a result is actually predicted by the model of drilling-induced self-excitations proposed by Richard, Germay and Detournay (2007). These experimental results therefore point to the need to perform drilling experiments, aimed at characterizing the bit–rock interface laws, under kinematic control (i.e., both rate of turn and rate of penetration imposed) so as to prevent the development of self-excited vibrations.

2.4.2.3 Complete Drilling Response

2.4.2.3.1 **Model** The response equations for drilling in phase I and II are readily developed from the earlier expressions for the cutting and contact components of the torque and weight. They are interpreted geometrically in Figures 2.62–2.65, which show the response of the bit in the spaces *d–w*, *d–t*, and *t–w*.

For phase I drilling, we obtain after combining Equations 2.65–2.68 the following expressions for w and t:

$$w = S_* d, \quad t = \mu\gamma' w \tag{2.78}$$

where

$$S_* = \zeta\varepsilon + \kappa\sigma, \quad E_* = \varepsilon + \mu\gamma\sigma\kappa, \quad \gamma' = \frac{\gamma}{1 - E_0/E_*} \tag{2.79}$$

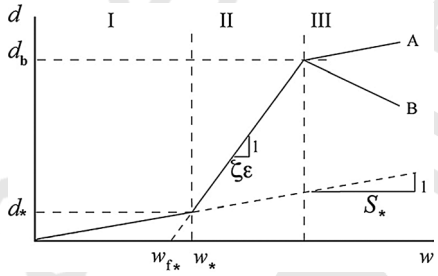

Figure 2.62 Conceptual response of the bit in the *w–d* space (Detournay, Richard and Shepherd, 2008).

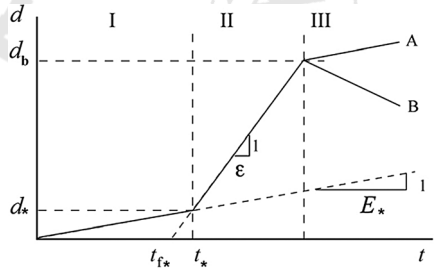

Figure 2.63 Conceptual response of the bit in the *t–d* space (Detournay, Richard and Shepherd, 2008).

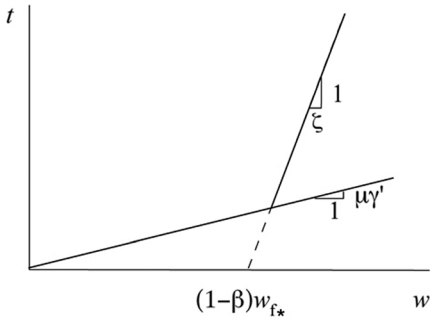

Figure 2.64 Conceptual response of the bit in the t–w space (Detournay, Richard and Shepherd, 2008).

If $|E_0/E_*| \ll 1$, as generally expected, we have $\gamma' \sim \gamma$ and thus

$$t \sim \mu\gamma w \tag{2.80}$$

The relationship between torque and weight on bit in phase I is therefore approximately the same as the constraint in Equation 2.68 between t_f and w_f. In other words, the response of the bit in phase I is dominated by the frictional contact process.

For phase II drilling, the incremental response of the bit is similar to that of a sharp bit, that is, any change in weight w and in torque t is assumed by the cutting component w_c and t_c, respectively. Hence the response in phase II can be written as

$$t - t_* = \varepsilon(d - d_*), \quad w - w_* = \zeta\varepsilon(d - d_*) \tag{2.81}$$

where

$$d_* = \ell/\kappa, \quad \frac{w_*}{w_{f*}} = \frac{E_* - E_0}{E_* - \varepsilon}, \quad \frac{t_*}{t_{f*}} = \frac{E_*}{E_* - \varepsilon}$$

Note finally that the cutting and contact components of the torque and the WOB can readily be calculated from w and t, if ζ and $\mu\gamma$ are known, according to (see Figure 2.65)

$$t_c = \frac{t - \mu\gamma w}{1 - \beta}, \quad w_c = \zeta t_c \tag{2.82}$$

$$w_f = \frac{w - \zeta t}{1 - \beta}, \quad t_f = \mu\gamma w_f \tag{2.83}$$

2.4.2.3.2 **Experimental Validation** A drilling experiment carried out at Schlumberger Cambridge Research with a small drilling rig (SDM) provides support to the drilling response model summarized above. Drilling tests in the SDM, which accommodates cylindrical rock samples that are about 200 mm in length and 150 mm in diameter and drill bits that have diameters up to 60 mm, are performed under controlled confining pressure, mud pressure, and pore pressure (prior to drilling), and under either imposed WOB or imposed rate of penetration [see Detournay, Richard and Shepherd (2008) for a presentation of drilling experiments performed under kinematic control].

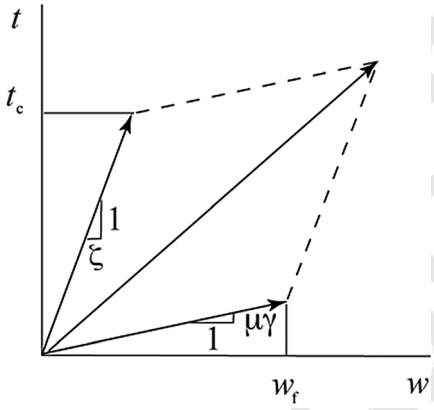

Figure 2.65 Decomposition of the bit response into cutting and contact components in the *w–t* diagram (Detournay, Richard and Shepherd, 2008).

The drilling experiment was conducted on a sample of Stancliffe sandstone under balanced conditions using a core barrel. The Stancliffe sandstone is a fine-grained rock from the Carboniferous Namurian, with uniaxial compressive strength $q = 85$ MPa, permeability $k = 2$ mD, and porosity $\phi = 13\%$. The core barrel has outer radius $a = 25.4$ mm and inner radius $b = 16.0$ mm; it is equipped with five rectangular PDC cutters with a backrake angle of 15° (angle taken positive for forward inclination of the cutting face). The nominal contact length ℓ is about 3 mm. The rock sample was saturated prior to drilling with the mud pressure and pore pressure maintained at approximately 3 MPa. The WOB was progressively increased manually until the appearance of a phase 3 regime. The angular velocity Ω was set to $2\pi\,\mathrm{s}^{-1}$ (60 rpm).

The results are illustrated in the *d–w, d–t, t–w, E–S* diagram shown in Figures 2.66 and 2.67. Gray filled points are used to distinguish a transition regime between phases I and II. Estimation of the model parameters for the "drill-on" experiment yields the following values: $\varepsilon = 77$ MPa, $\zeta = 0.64$, $\mu\gamma = 0.70$ (corresponding to a friction angle $\varphi = 35°$ at the wearflat–rock interface, on account that $\gamma = 1$), $\sigma = 40$ MPa. The inferred value of intrinsic specific energy ($\varepsilon = 77$ MPa) is close to the measured uniaxial compressive strength (UCS) (UCS = 85 MPa) of the Stancliffe sandstone, thus confirming the correlation between ε and UCS obtained in scratch tests conducted at atmospheric pressure (Dagrain, Richard and Detournay, 2008). (Since the mud pressure and pore pressure are balanced, the forces on the bit are expected to be similar to those that would be observed in a similar drilling experiment at atmospheric pressure.)

2.4.3 Percussion–Rotary

The major disadvantages of rotary drills are the occurrence of excessive bit wear at high rates of rotation, high values of thrust, and/or in hard rock; the major demerits of percussion drills are their relatively low penetration rate in soft rock and

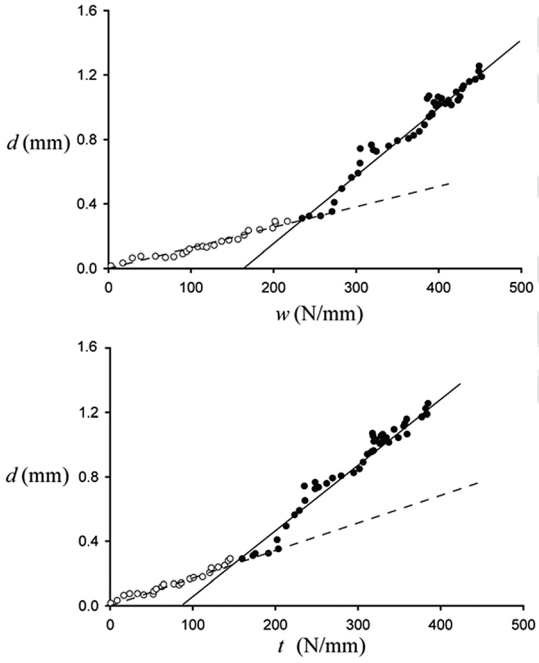

Figure 2.66 *w–d* and *t–d* diagrams for drill-on test conducted in Stancliffe Sandstone. White and black symbols identify phase I and phase II drilling regimes, respectively.

discontinuities in the process of cutting (Figure 2.68). The combination of both drills (percussion–rotary-) results in a fast ROP at a low level of thrust (Roberts, 1981).

Because rock is damaged by repetitive impacts, bit penetration and rotation become much easier than in solely percussion drilling. Therefore, larger amount of chips may be sheared off the rock. On the other hand, debris removal becomes more efficient because of bit rotation, which results in a fresh rock surface consistently.

However, combination of percussion thrust and rotation involves so many complicated processes that few experiment has been done so far to investigate the physics.

2.4.4 Other Drilling Methods

In addition to mechanical drills such as rotary and percussion, there are other drilling methods. Based on the energy type utilized in rock removal, some examples are as follows:

- Thermal drills such as the laser drill, nuclear drill, electricity melting drill, microwave drill, magnetic drill, plasma drill, and so on. Laboratory tests demon-

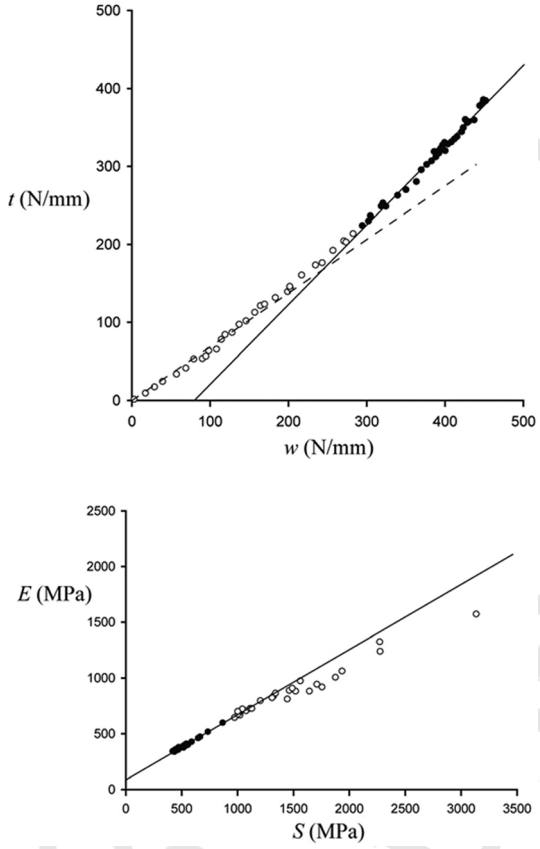

Figure 2.67 *t–w* and *E–S* diagrams for drill-on test conducted in Stancliffe Sandstone. White and black symbols identify phase I and phase II drilling regimes, respectively.

strate that modern lasers have more than enough power to spall, melt, and vaporize rock (Parker *et al.*, 2003). They also showed that the type of rock tested did not significantly change the amount of energy needed to cut or melt it.

- Nuclear reactors can produce temperatures high enough to fuse and vaporize the rock. Adams (1965) patented a needle-shaped nuclear penetrator for drilling into the Earth's crust. It melts the rock beneath it and will melt back to the surface after it reaches a predetermined depth. It has not been under development since 1960s, because of the size limitations on the reactors, high cost, and safety problems.
- Using fluorine and other reactive chemicals, chemical drilling has been successfully tested to drill sandstone, limestone, and granite in the laboratory (McGhee, 1955). However, it needs to deal with large volumes of highly reactive chemicals and damages the environment to such an extent that any logging or sampling process becomes meaningless.

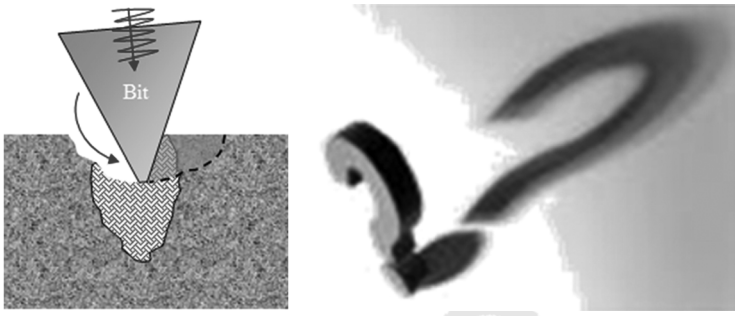

Figure 2.68 Illustration of a percussion–rotary drill.

- Explosive drills were used mainly in the Soviet Union (Ostrovskii, 1960). With mixing of two non-explosive liquids, a chemical is used to initiate the explosion, which demolishes rock.

While different drilling methods involve different rock breakage mechanisms, it is fair to say that there is still a long way to go before most of non-mechanical drills mentioned above could be applied in field.

2.4.5 Drilling Efficiency

2.4.5.1 Index for Drilling Efficiency

Different indexes have been developed in various drilling industries to evaluate the efficiency of drilling. Some examples are given below.

Specific energy is defined as the energy required to remove unit volume or mass of rock. It is related not only to the intrinsic properties of rock but also to bit type and design. Efficiency of fragmentation could be achieved through a combination of optimum bit insert spacing and steady-state cutting, which continuously removes layers cracks and weakens successive layers (Demou, Olson and Wingquist, 1983). For example, the specific energy is found to decrease rapidly with increasing inserted depth at first, but then to level off to a relatively constant value (Figure 2.69). An estimate obtained in oil shale is that the specific energy for steady-state drag bit fragmentation is about 30% of that required for independent fragmentation (Larson and Olson, 1977).

Resistance is a function of the rock toughness and of the degree of thrust exerted. It can be seen that the amount of the transmitted energy depends on these factors rather than the available energy. In very soft or very tough rock, or if the drill is operated free or with insufficient thrust, residual energy will remain in the rod and drill to build up to potential failure levels. Only a proportion of the impact energy is available for rock breakage.

Rock drillability is used as a comprehensive index, often in the mining and quarrying industries, that was initially based on the hardness and toughness of rocks and rock strength, and later related to specific gravity, penetration rate, drill bit wear, and properties of drill cuttings.

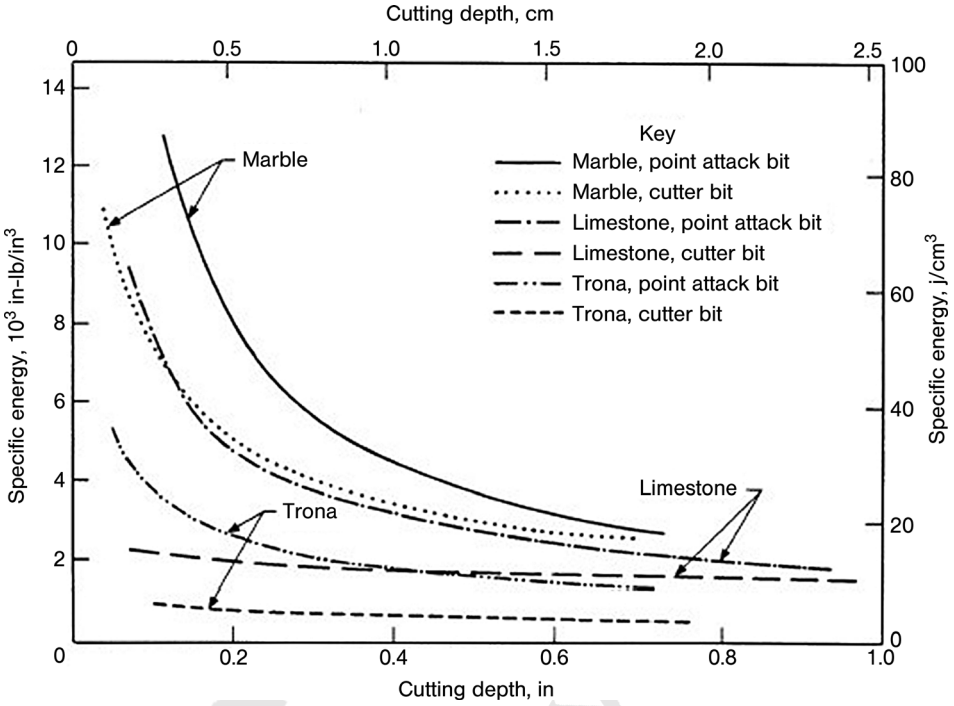

Figure 2.69 Specific energy vs cutting depth.After Demou, Olson and Wingquist (1983).

IF factor, which is the product of impact force (*I*) and the frequency of blows per minute (*F*), was used to evaluate the performance of the percussion drilling tool (Topanelian, 1957).

ROPs are more often considered in the oil industry, as a faster ROP with acceptable economic cost usually means lower cost per foot and faster capital recovery. Reducing the cost per foot generally requires achieving a higher average rate of penetration and/or increasing the useful drilling time between trips.

2.4.5.2 Static and Dynamic Variables to Improve Drilling Efficiency

All possibilities that may improve or lower ROPs may be classified into two categories: static and dynamic. The static group refers to the parameters that hardly change with time once the equipment has been installed in place, such as bit hardness and strength, rock strength, abrasiveness, and hardness. Dynamic parameters are manageable and may change with time of drilling, such as hammer energy, bit abrasion, BHP, thrust force, WOB, rotation speed (rpm), and drilling fluid.

2.4.5.2.1 **Static Variables** The selection of bit materials is a very important issue. In soft sediments, drilling bits tipped with tungsten carbide can sometimes be used. In harder rocks, diamond bits are essential. Diamond is a crystalline, compact or drypto-crystalline form of pure carbon, and is the hardest substance known so far. It occurs as octahedral crystals with a perfect cleavage parallel to the faces of the octahedron.

Alluvial diamonds may be rounded due to attrition, and the faces of diamond crystals are often curved. However, diamond is brittle; therefore very sharp edges wear away rapidly due to fracture and graphitization caused by localized overheating (McGregor, 1967). For this reason, excessive thrust should not be used on a new diamond bit.

Carbide is the single greatest variable for downhole bits. The percentage of cobalt in the carbide grade is an important consideration: it is determined by fracture toughness and wear resistance. Different shapes of carbides have been tried (Leonard, 2001): spherical carbide, also known as hemispherical carbide, is best suited for hard to medium-hard rock formations; parabolic, also referred to as semiballistic or ogive carbide, is used in medium-hard formations; the ballistic carbide's curved bullet shape offers rapid cutting speeds and is used mostly in softer formations. This type of carbide is prone to shear failure in harder formations.

Tests on different bit types, including point attack bits and cutter bits, indicate that, compared with point attack bits, cutter bits are more efficient in rock fragmentation, showing lower cutting and normal forces and less bit deterioration (Demou, Olson and Wingquist, 1983). Also, it has been found that optimum cutter spacing of the drag bit is generally equal to or greater than the average crater width at a given depth. For example, for a cutting depth of 0.5 in, a crater width of 2.4 in will be equal to or less than the optimum spacing.

Hardness is a measure of the resistance of a mineral to scratching (not breakage). The wear between moving surfaces in frictional contact depends largely upon their hardness (Rabinowicz, 1965): if one surface is significantly harder than the other, the hard surface should wear very little. Different terms have been used for quantifying hardness, such as

- Shore hardness or scleroscope hardness is measured in terms of the elasticity of the material. A diamond-tipped hammer in a graduated glass tube is allowed to fall from a known height on to the specimen to be tested, and the hardness number depends on the height to which the hammer rebounds;
- Mohs' scale, used to assign values to the hardness of different minerals from 1, the softest, to 10, the hardest, is based on the scratch test and makes use of common minerals as standards. Mohs' scale, however, becomes so compressed that it does not provide adequate distinction between hard substances. Accordingly, Ridgeway, Ballard and Bailey (1933) extended the upper portion of the scale so that it ranges from 7 to 15.
- Hardness is often related to rock strength, that is, hard rock is usually strong. For three different tested materials in Demou *et al.*'s experiment, including Indiana limestone, Tennessee marble, and Valders white rock, UCSs were 10 000, 16 800, and 29 600 psi, respectively, and the Shore hardness was 32, 55, and 68 scleroscope units, respectively (Demou, Olson and Wingquist, 1983). Compared with a baseline rock with UCS 7200 psi and Shore hardness 23, a simple relation between rock uniaxial compressive strength and Shore hardness was observed:

$$\frac{10\,000}{7200} \approx \frac{32}{23}; \quad \frac{16\,800}{7200} \approx \frac{55}{23}$$

2.4.5.2.2 **Dynamic Parameters** In percussion drilling, the energy and frequency of hammer blows rely heavily on the pressure of the working fluid and the access of flow to the workings of the tool. Physical parameters, such as the geometry and mass of the hammer, the geometry, mass, and stiffness of the drill bit used, and the stroke of the hammer may likewise be optimized, although not real-time while drilling. It has been found and can be demonstrated that most of the available energy contained in the piston during the power stroke is transferred to the rod (McGregor, 1967), provided that the rod is longer than half the impact wavelength, and given that the resistance to the bit is sufficient to enable the rod shank to be impacted.

Bit abrasion, dullness, or wear may be affected by rock abrasiveness and the torque and thrust applied to the bit. Quartz, of course, is harder than most steels. Among different types of drilling bit cutters, such as steel, tungsten carbide, natural diamonds, and PDC, wear is least rapid for tungsten carbide because it is marginally harder than silica. Similarly, diamonds rapidly lose their ability to cut if they are polished by the dust. The polishing effect may prove to be more deleterious to the bit than a scratch. With percussion drilling, the rocks that need to be considered as highly abrasive are those containing:

1. Quartz, for example, quartzite, sandstone, grit and acid-igneous rocks.
2. Other forms of silica, for example, flint, chert, jasper, and wood-opal.
3. Olivine, for example, dunite and some forms of basalt.
4. Garnet, for example, garnetiferous gneiss.
5. Thrust is the force applied to hold a bit against rock so that it can penetrate and drill forward as rock debris is removed during drilling. It can be either dynamic or static: the latter derives from the weight of the drilling string and the applied force resulting from a certain "feed mechanism". In rotary drilling, penetration is proportional to thrust (Figure 2.70). In percussion drilling, insufficient thrust produces several undesirable effects, including damage in the drill caused by the

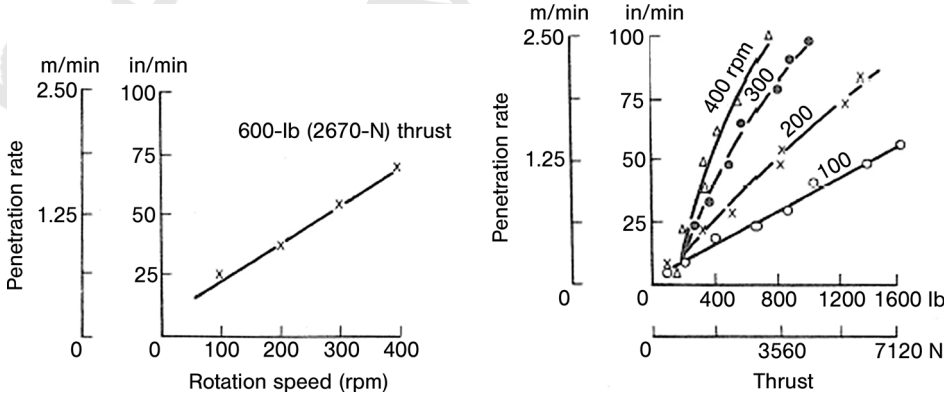

Figure 2.70 Characteristic curves for rotary drag-bit drilling (Fish and Barker, 1956).

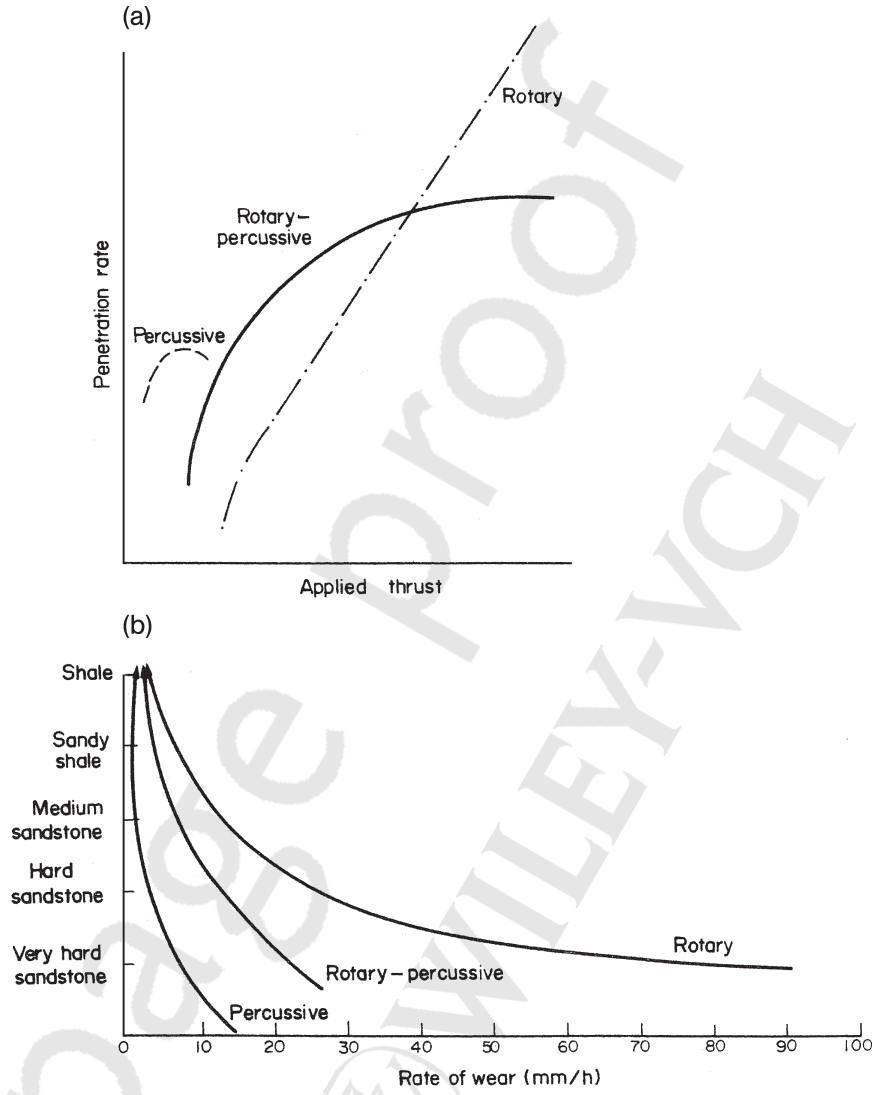

Figure 2.71 (a) Typical thrust vs penetration rate curves; (b) comparative wear rates (Fish, 1961).

piston striking the fronthead, heating up of drill rods and bits due to unabsorbed energy, and increase in bit wear and rig vibration, which is described as bit "chattering" (Roberts, 1981).

6. On the other hand, with increasing thrust, penetration increases progressively until an optimum level is reached (Figure 2.71). Further increase gives rise to reduced piston stroke length, bended rods, deviated hole, bit wear, and restricted or stalled bit rotation.

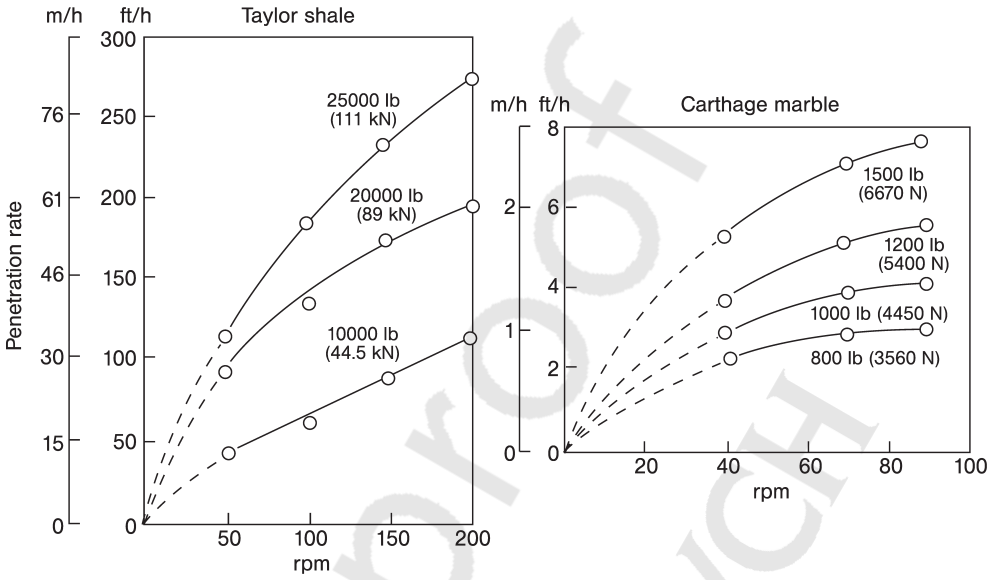

Figure 2.72 ROP vs rpm at various thrusts on a roller bit (Gatlin, 1960).

The effect of bit rotation speed (rpm) on rock penetration is a "two-edged sword". Faster rotation results in a higher input of cutting energy into the drilled rock due to higher shear stress at the contact of the bit and rock and a faster cutting speed (Figure 2.72); on the other hand, this requires more power on the ground to drive the rotation and leads to more bit abrasion that decreases penetration and increases drilling cost. Some experiments suggested that different cutting speeds between 10 and 70 in s^{-1} did not produce any significant change in cutting efficiency (Demou, Olson and Wingquist, 1983). In down-the-hole drilling, a rotation speed of about 40 rpm is commonly considered to be satisfactory; but in abrasive rock such as quartzite, 10 rpm is recommended. In non-abrasive rocks, higher rotation speeds can be selected, up to about 100 rpm (McGregor, 1967). In oil and gas drilling, the rotation speed is usually restricted to 30–100 rpm.

A side-effect of low rotation speeds is the vibration, which has been proven to be more detrimental to bit wear than rotation itself. Therefore, diamond-set drill bits operate at fairly high rotational speeds. Higher rotation speed, however, is practical with turbine drills, as these give less vibration. In certain underground mining operations, particularly in Canada, rotational speeds as high as 3000–4000 rpm are used with a gain in footage/wear ratio.

2.4.5.2.3 **Drilling Fluid** Often referred to as "mud" in the oil and gas industries, drilling fluid is critical to underground drilling. With appropriate rheology and circulation, drilling fluid could remove rock debris generated during hole introduction and leave a fresh rock surface for the bit to attack. Meanwhile, it cools the drill bit, provides pressure support to avoid hole collapse, and serves as an effective means to maintain well control.

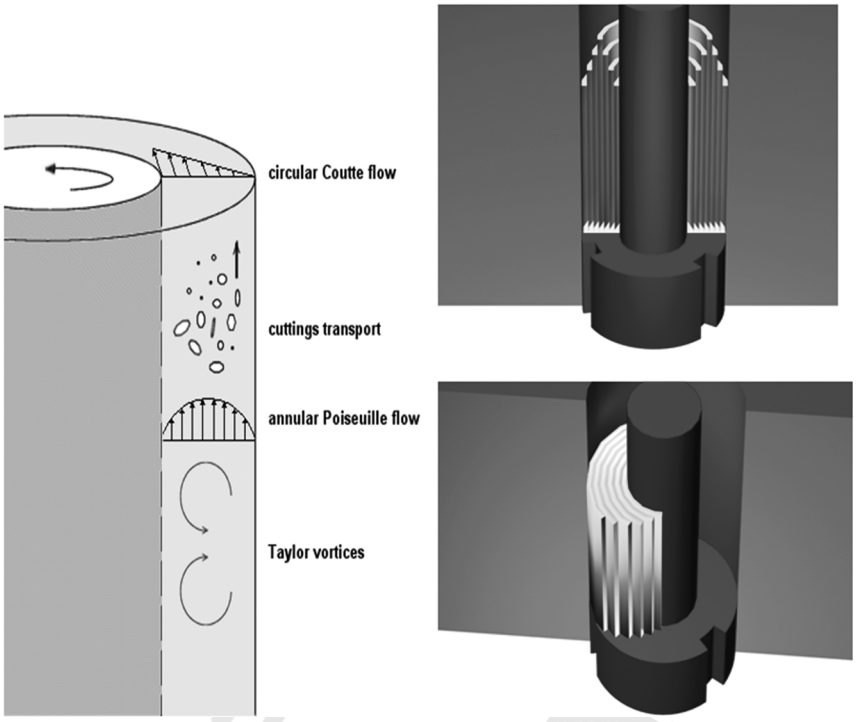

Figure 2.73 Circulation of drilling fluids in well annulus (a) and its radial (b) and axial (c) flow patterns (Bruno, Han and Honeger, 2004).

There are different drilling fluids, such as oil-based liquid, water-based liquid, gas or air. Many drilling fluids are a plastic fluid that is complex and non-Newtonian in which the shear stress is not proportional to the shear rate. A definite pressure (yield point) is required to initiate and maintain movement of the fluid.

A particle suspended in a fluid is subjected to a number of hydrodynamic forces (Figure 2.73). The momentum of a solid particle moving with a fluid can be described as (Bruno, Han and Honeger, 2004)

$$\rho_p V_p \frac{d\mathbf{v}_p}{dt} = -\rho_{fl} V_p g + \int_S T\boldsymbol{n} dS \tag{2.86}$$

where V_p is particle volume, ρ_p is its density, $\boldsymbol{v}_p$ is the particle velocity vector, S is the particle surface, $\boldsymbol{n}$ is a unit vector, and T is the instantaneous stress tensor that must satisfy the Navier–Stokes equations, and represents all forces between fluid and particle. This include forces from fluid–particle interactions in either laminar or turbulent flow, such as drag force due to fluid viscosity and pressure drop across rock particles, buoyancy force due to density difference of fluid and particles, Basset force due to fluid velocity difference from particles, Magnus force due to particle rotation,

inert force due to particle acceleration or deceleration, and so on. The effect of pipe rotation on fluid transportation can be estimated with a solution of the circumferential velocity from the Taylor–Couette experiment (Taylor, 1923).

2.5 Conclusion

This chapter is intended to cover the fundamentals of rock and its breakage. We first evaluated drilling-related properties from both terrestrial and extraterrestrial rocks, their determinations, and influence factors. Then stresses were described in sedimentary basins and around boreholes. With understanding of rock properties and stresses, various drilling methods, especially percussion and rotary, were investigated.

2.5.1 Underground Rocks and Stresses

Rocks involved in drilling could be classified into three groups: igneous, sedimentary, and metamorphic. Rock response to drilling activities relies not only on the level of applied loads, but also on rock characteristics, including elastic, strength, and transport properties. Various moduli, such as Young's modulus, bulk modulus, shear modulus, and the modulus of toughness, along with Poisson's ratio and bulk compressibility, describe rock elastic deformation. Rock strengths such as shear strength, UCS, and residual strength define the loading capacity of rock. If rock is saturated with fluid, porosity and permeability are used to quantify its transport properties.

Rock properties are often related to each other. For example, various correlations have been developed between rock strength and porosity, and among rock strength and moduli variables themselves. Rock mechanical properties are affected by many internal and external conditions. Factors include grain size, cement type, contact pattern, *in situ* stress level, temperature, cracks and fissures, and rock heterogeneity. Laboratory testing conditions, such as loading rate, coring method, and specimen geometry, could further complicate the estimation of the properties.

They could be determined through either static laboratory tests or dynamic logging methods.

- In the laboratory, rock cores must be carefully preserved and tested under high-quality conditions to determine mechanical, transport and chemical rock properties for design and analysis. Triaxial tests are the standard method of obtaining information on deformation and strength behavior for stability analysis in drilling. Drill chips and poorer quality cores can still be of value, as these materials can be assessed using rapid index tests to use as correlates to mechanical and transport properties.
- In the field, elastic constants are dynamically estimated from sonic wave velocities, bulk density, and shale content. Sonic waves are also sensitive to the presence of fluids and the level of *in situ* stresses. Furthermore, the ratio of compressional and shear wave velocities is an indicator of formation consolidation. Even though rock

strength cannot be measured directly from logs, consistent efforts have been made to develop empirical correlations between rock strength and other measurements. Due to the empirical nature of these correlations, calibrations should be made before applying to a field.

Subsurface drilling will likely play a large role in future exploration as planetary missions increase in scope and complexity. Knowledge of the physical and mechanical properties of planetary materials is derived from a number of sources, including meteorites, *in situ* measurements from landed spacecraft, and inferences from remote measurements. The only extraterrestrial drill cores returned to Earth are the lunar drill cores obtained by the Apollo and Luna missions. These samples and the experience gained through their extraction provide invaluable guides for future drilling into planetary regolith environments, especially on atmosphereless bodies such as asteroids and the planet Mercury. A second source of data on physical properties that may help guide future exploration efforts is data from penetrometers, which have been successfully flown on landed missions to the Moon, Mars, Venus, and Titan.

In situ stresses and pressures are vital data required for analysis as these values, combined with material properties and geometric disposition, define the initial conditions for all analyses including flow response, fracturing behavior, mechanical stability, and drillability.

Stress magnitudes and orientations can be estimated using large-scale tectonic fabric, geological history, depth and lithostratigraphic disposition. This provides valuable general data that can be used to design drilling programs and even to make preliminary assessments of casing points. However, for risk management, it is necessary to obtain more precise estimates of stresses and pressure. Direct measurements of *in situ* stresses are mainly based on variations of hydraulic fracturing methods, which also include leak-off tests, extended leak-off tests, and formation integrity tests. Borehole seismic and regional seismic methods can help give some indication in certain conditions using calibrations and correlations in addition to factors such as shear wave anisotropy, which is likely related to stress directions. Pore pressures are usually measured directly with borehole methods, although new seismic methods combined with knowledge of the geological and tectonic history can help in pressure estimates.

Indirect measures of stress magnitudes and orientation can be provided by geophysical log data (anisotropic response, breakouts, axial fractures), or else cores can be tested in certain ways to allow estimates to be made. For example, careful ultrasonic velocity measurements on oriented cores show anisotropy that may be related to the stress orientations *in situ*.

Stresses and pressures dictate where casing points will be placed. The limiting factors are borehole instability or blowout conditions at the bit, and also the hydraulic fracturing pressure at the shoe. As one drills deeper below an existing casing shoe, these values generally approach nearer to one another until they become virtually the same, dictating the need for a new casing string.

Stresses can be altered through drilling itself (creating an opening), by changes in pressure, through temperature changes, and by chemical effects such as salt dissolu-

tion or exposure of shale to drilling fluids of different chemistry. These factors can, of course, be controlled to increase borehole stability in various stress regimes.

The solutions of elastic and inelastic stresses around a vertical hole with or without fluid flow have been given in this chapter. For a weak formation, a Coulomb zone near the wellbore has been identified. In this zone, rock has yielded and been damaged to a certain extent but has not completely lost its functionality and collapsed into the borehole. For a strong rock with low *in situ* stresses, such a zone may not exist. When far-field stresses are anisotropic horizontally, rock deformation concentrates in the direction of minimum horizontal stress, and represents the highest risk of borehole instability or collapse.

2.5.2 Drilling Theories

Among various rock removal techniques, percussion and rotary drills are probably the two most widely used.

With a long history, percussion drilling has been recognized as a fast rock penetration method, even faster than using a rotary drill or diamond drill in some hard formations. Merits such as low requirement of WOB, shorter bit–rock contact time, longer bit life, less hole deviation, and larger cuttings have encouraged people to apply percussion drilling to both terrestrial and extraterrestrial rocks. Meanwhile, inclusive overall results, risks in operations, and economic uncertainties greatly limit the wider acceptance of this technology.

Percussion drilling involves four fundamental processes: (1) the drillbit penetrates the rock with compression and vibration; (2) the rock receives an impact, stress propagates, and damage accumulates; (3) the rock fails and disaggregates; and (4) cuttings are transported away from the bit and up into the annulus. These are coupled physical processes, with different physics related to the tool and bit mechanics, rock mechanics, and cuttings transport mechanics.

To improve the understanding of rock physics in percussion drilling, two groups of laboratory tests were summarized in the chapter: single-impact tests and full-scale hammer tests. In single impact tests, both the stress inside the rock samples and the stress of the steel rod were recorded at a frequency as high as 91 kHz, along with the displacement of the rod. For each rock sample, three impacts were sequentially loaded at the same rock location to investigate the effect of cyclic loading on rock damage. Meanwhile full-scale drilling tests were carried out with an industrial mud hammer and *in situ* high-stress conditions. Both underbalanced and overbalanced conditions were investigated.

The studies have shown that when a hammer impacts rock, some stress waves are transferred from the hammer to the rock while the other waves are reflected and dissipated mechanically and thermally. Different failure mechanisms have been involved at different stage of hammer–rock impact: compressive failure occurs in a stress concentration zone with high compression and can extend several diameters deeper than the penetration depth of the cutter; tensile fractures are critical for efficient rock breakage in percussion drilling and generally formed outside the edge of the

compressive zone, tipped towards the surface. When there is little BHP compressing the rock surface, rock may break more easily in tension, not only when the bit impacts but also when the bit retreats. The indention data from single-impact tests, the hammer performance from full-scale drilling tests, and the cuttings collected all indicate the existence and the importance of tensile failure in breaking rock in percussion drilling.

An analytical model for describing the interaction between adjacent cutters in a coring bit is derived for the coring bits with wedge-shaped cutting teeth of vibratory drills that penetrate by percussion into brittle material. The overall coring bit-specific energy is derived as a function of the cutter's spacing and teeth number. There exists an optimal spacing/depth ratio or an optimal teeth number that minimize the coring bit specific energy and hence maximize its drilling rate. Experimental drilling tests have been performed and confirmed the theoretical development.

Different indexes have been used in different industries to evaluate drilling efficiency, such as specific energy, rock drillability, and rate of penetration. Possibilities that may improve or lower the drilling efficiency may belong to either static or dynamic groups. Static variables refers to the parameters that hardly change with time once the equipment has been installed in place, such as bit hardness and strength, rock strength, abrasiveness, and hardness. Dynamic parameters are manageable and may change with time of drilling such as hammer energy, bit abrasion, BHP, thrust force, WOB, rotation speed, drilling fluid, and so on. To improve drilling efficiency, we should marry the designs of the bit and drilling system with the understanding of rock properties and behavior.

2.5.3 Effect of Environment on Drilling

The effect of temperature on the strength of rock was found to be significant by many researchers (e.g., Heins and Friz, 1967; Mellor, 1971; Zacny and Cooper, 2007). Since the drillability of rocks and the WOB required to achieve penetration are inversely proportional to rock strength (i.e., with higher rock strength it is more difficult to drill the rock), it is expected that the low temperature may in turn affect the efficiency of the rock-breaking process. Heins and Friz (1967) found that the strength of an oven-dried basalt rock increases by 50% when cooled to –80 °C, which means that in theory the WOB required to allow the cutter to penetrate the rock would be 50% higher and also the power required to drill would also be 50% higher. In practice, however, the rock in the immediate vicinity of a drill bit will heat up, and as a result the effect of the low temperature will be somewhat diminished.

Symbols and Abbreviations

C	rock compressibility
C_b	bulk compressibility
C_f	compressibility of pore fluid

C_m	rock matrix compressibility
C_s	compressibility of the reservoir solid material
c_0	rock cohesive strength
d	diameter of grain (grain size), depth of cut
E	Young's modulus, specific energy
E_s, E_d	Static and dynamic Young's modulus
F_c	capillary force
G	shear modulus, modulus of rigidity
h	formation thickness
K	bulk modulus
K'	ratio of the horizontal to vertical effective stresses
k	permeability
M_t	modulus of toughness
P	fluid pressure, rate of energy dissipation at the bit–rock interface
P_c	capillary pressure
Q	volume flow rate per unit time
R	particle radius, borehole radius
S	specific surface area, drilling strength
T	temperature, torque on bit
V	volume, rate of penetration
V_{sh}	volume of shale
v_p, v_s	velocities of compressional wave and shear wave
W	weight on bit
α	Boit's poroelastic constant
β	rock failure angle
β_T	linear coefficient of thermal expansion
λ	Lamé elastic constant, factor accounting for nonuniform particle size effect on rock strength
η	drilling efficiency
ϕ	rock porosity
φ	internal friction angle
ρ	rock density
ρ_b	rock bulk density
ρ_s	solid grain density
ρ_f	pore fluid density
Ω	angular velocity
γ	surface tension
μ	coefficient of friction, fluid viscosity
ν	Poisson's ratio
σ	total stress
σ_x, σ_y, σ_z	stresses in the direction of x, y, z in Cartesian coordinates
σ_r, σ_θ	radial and tangential stresses in cylindrical coordinates
σ_v, $\sigma_{h\max}$, $\sigma_{h\min}$	vertical, maximum, and minimum horizontal principal stresses
σ_1, σ_2, σ_3	maximum, medium, and minimum principal normal stresses

σ'_1, σ'_2, σ'_3	maximum, medium, and minimum effective principal stresses
σ_c	rock compressive strength
σ_T	tensile strength
τ	shear stress
ε	strain, intrinsic specific energy
ε_x, ε_y, ε_z	rock strain in the direction of x, y, z in Cartesian coordinates
ε_r, ε_a	radial and axial strain
$\bar{\varepsilon}_z$	critical strain for rock failure in compression
BHP	bottom hole pressure
PDC	polycrystalline diamond compacts
ROP	rate of penetration
UCS	uniaxial compressive strength
WOB	weight on bit

Acknowledgments

The authors deeply appreciate the generous and professional efforts from the three technical reviewers: Earling Fjær, Chief Scientist at SINTEF, Trondheim, Norway; Robert W. Zimmerman, Head of the Division of Engineering Geology and Geophysics at the Royal Institute of Technology, Stockholm, Sweden; and Constantinos Mavroidis, Director of the Biomedical Mechatronics Laboratory, Department of Mechanical and Industrial Engineering at Northeastern University, Boston, MA, USA. The authors would like to acknowledge Yoseph Bar Cohen of the Jet Propulsion Laboratory at Caltech and NASA for help with completing this chapter, and for his countless suggestions that helped to make it a stimulating read. Our gratitude is also extended to Patrick Fink, Honeybee Robotics, for his help with the references. The percussion drilling research was originated and sponsored by the National Energy Technology Laboratory at the Department of Energy; some other studies in this chapter were conducted at the Jet Propulsion Laboratory, California Institute of Technology, and Honeybee Robotics Spacecraft Mechanisms Corporation under a contract with NASA.

References

Adams, W.M. (1965) Nuclear reactor apparatus for earth penetration, US Patent No. 3,155,194.

Almenara, R. and Detournay, E. (1992) Cutting experiments in sandstones with blunt {PDC} cutters. *Proceedings of the EuRock'92*, Thomas Telford, London, pp. 215–220.

ASTM (2000) *Standard Test Methods for Maximum Index Density and Unit Weight of Soils Using a Vibratory Table, Publication* No. D 4253, ASTM International.

Basilevsky, A.T., Kuzmin, R.O., Nikolaeva, O.V., Pronin, A.A., Ronca, L.B., Avduevsky, V.S., Uspensky, G.R., Cheremukhina, Z.P., Semenchenko, V.V. and Ladygin, V.M. (1985) The surface of Venus as revealed by the Venera landings: Part II. *Geological Society of America Bulletin*, **96**, 137–144.

Bates, R.E. (1964) Field results of percussion air drilling. The 39th SPE Annual Fall Meeting, Houston, TX, 11–14 October 1964, SPE 886.

Beer, F.P., Johnston, E.R.J.T. and deWolf, J.T. (2005) *Mechanics of Materials*, 4th edn, McGraw-Hill, New York, p. 800.

Bell, F.G. (1978) The physical and mechanical properties of the Fell Sandstones, Northumberland, England, *Engineering Geology*, **12**, 1–29.

Besson, A., Burr, B., Dillard, S., Drake, E., Ivie, B., Ivie, C., Smith, R. and Watson, G.(Autumn 2000) On the cutting edge. *Oilfield Review*, 36–57.

Black, A.D., Walker, B.H., Tibbitts, G.A. and Sandstrom, J.L. (1986) PDC bit performance for rotary, mud motor, and turbine drilling applications. *SPE Drilling Engineering, SPE 13258*, 409–416.

Brady, B.H.G. and Brown, E.T. (1985) *Rock Mechanics for Underground Mining*, George Allen & Unwin, London.

Brett, J.F. (1992) The genesis of torsional drillstring vibrations. *SPE Drilling Engineering*, **7**, 168–174.

Bruce, S. (1990) A mechanical stability log. The 1990 IADC/SPE Drilling Conference, Houston, TX, 27 February–2 March 1990, SPE/IADC 19942.

Bruno, M., Han, G. and Honeger, C. (2004) Advanced simulation technology for combined percussion and rotary drilling and cuttings transport. *GasTips*, **11** (9), 5–8.

Bui, H., Meyers, J. and Swadi, S. (1995) Steerable percussion air drilling system. DOE Contractor Review Meeting, Baton Rouge, LA, April 1995.

Burshtein, L.S. (1969) Effect of moisture on the strength and deformability of sandstone. *Soviet Mining Science*, **N4**, 573–576.

Byrne, P.M., Cheung, H. and Yan, L. (1987) Soil parameters for deformation analysis of sand masses. *Canadian Geotechnical Journal*, **24**, 366–376.

Carmichael, R.S. (1982) *Handbook of Physical Properties of Rocks*, Vol. 2, CRC Press, Boca Raton, FL, 13:9780849302282.

Carrier, W.D. III (1974) Apollo drill core depth relationships. *Moon*, **10**, 183–194.

Carrier, W.D. III, Mitchell, J.K. and Mahmood, A. (1973) The relative density of lunar soil. Proceedings of the 4th Lunar and Planetary Science Conference, pp. 2403–2411.

Carrier, W.D. III, Olhoeft, G.R. and Mendell, W. (1991) Physical properties of the lunar surface, in *The Lunar Sourcebook* (eds G.H. Heiken *et al.*), Cambridge University Press, New York, pp. 475–594.

Cheatham, J.B. Jr (1977) The state of knowledge of rock/bit tooth interactions under simulated deep drilling conditions. Terra Tek Report. Terra Tek.

Cherkasov, I.I., Kemurdzhian, A.L., Mikhailov, L.N., Mikheev, V.V., Morozov, A.A., Musatov, A.A., Savenko, I.A., Smorodinov, M.I. and Shvarev, V.V. (1967) Determination of the density and mechanical strength of the surface layer of lunar soil at the landing site of the Luna 13 Probe. *Kosmicheskie Issledovaniya*, **5** (5), 746–757, in Russian.

Choate, R., Batterson, S.A., Christensen, E.M., Hutton, R.E., Jaife, L.D., Jones, R.H., Ko, H.Y., Scott, R.F., Spencer, R.L., Sperling, F.B. and Sutton, G.H. (1968) Lunar surface mechanical properties. Surveyor Project Final Report, Part 2. NASA Technical Report 32-1265, Jet Propulsion Laboratory, pp. 137–194.

Coates, G.R., Schulze, R.P. and Throop, W.H. (1982) VOLAN – an advanced computational log analysis. Proceedings of the SPWLA 23rd Annual Logging Symposium, Corpus Christi, TX, 6–9 July 1982, Paper A.

Coates, G.R. and Denoo, S.A. (1981) Mechanical properties program using borehole analysis and Mohr's circle. Proceedings of the SPWLA 22nd Annual Logging Symposium, Houston, TX, 23–26 June 1981.

Colback, P.S.B. and Wiid, B.L. (1965) The influence of moisture content on the compressive strength of rock. Proceedings of the 3rd Canadian Symposium of Rock Mechanics, Toronto, pp. 65–83.

Cunningham, R.A. and Eenink, J.G. (1959) Laboratory study of effect of overburden,

formation, and mud column pressure on drilling rate of permeable formations. *Journal of Petroleum Technology, Transactions of AIME*, **204**, 9–15.

Dagrain, F. (2006) Etude des mécanismes de coupe de roches avec couteaux usés. Approche des mécanismes de frottement sous les couteaux par le concept du troisième corps. PhD thesis, Université Polytechnique de Mons.

Dagrain, F., Richard, T. and Detournay, E. (2008) Determination of rock strength properties from scratching tests. *International Journal of Rock Mechanics and Mining Sciences,* to be submitted.

Davies, J.P. and Davies, D.K. (2001) Stress-dependent permeability: characterization and modeling. *SPE Journal*, **SPE 71750**, 224–235.

Deily, F.H. and Durelli, A.J. (1958) Bottom hole stress in a well bore. The SPE Annual Meeting, Houston, TX, 5–8 October 1958, SPE 1095.

Deliac, E.P. (1986) Optimization des machines d'abattages à pics. PhD thesis, Université Pierre et Marie Curie, Paris.

Demou, S.G., Olson, R.C. and Wingquist, C.F. (1983) Determination of bit forces encountered in hard rock cutting for application to continuous miner design, Report of Investigations 8748. United States Department of the Interior and Bureau of Mines, Washington, DC.

Detournay, E. and Atkinson, C. (2000) Influence of pore pressure on the drilling response in low-permeability shear-dilatant rocks. *International Journal of Rock Mechanics and Mining Sciences,* **37** (7), 1091–1101.

Detournay, E. and Defourny, P. (1992) A phenomenological model of the drilling action of drag bits. *International Journal of Rock Mechanics and Mining Sciences,* **29** (1), 13–23.

Detournay, E. and Drescher, A. (1992) Plastic flow regimes for a tool cutting a cohesive-frictional material, *Proceedings of the 4th International Symposium on Numerical Methods in Geomechanics (NUMOG IV)*, Balkema, Rotterdam.

Detournay, E. and Richard, T. (2008) Mechanics of rock cutting. *International Journal of Rock Mechanics and Mining Sciences,* in preparation.

Detournay, E., Richard, T. and Shepherd, M. (2008) Drilling response of drag bits: theory and experiment. *International Journal of Rock Mechanics and Mining Sciences,* in press.

Donaghe R.T., Chaney R.C. and Silver M.L.(eds) (1988) Advanced triaxial testing of soil and rocks. Proceedings of the 1986 ASTM Symposium, Louisville KY, ASTM Committee D-18, p. 896.

Duke, M.B. and Nagle, J.S. (1974) *Lunar core catalog*. NASA Johnson Space Center, JSC09252, p. 242.

Dullien, A.L. (1979) *Porous Media: Fluid Transport and Pore Structure*, Academic Press, New York.

Duncan, J.M. and Chang, C.Y. (1970) Nonlinear analysis of stress and strain in soils. *Journal of the Soil Mechanics and Foundations Division*, Proceedings of the ASCE, SM5, 1629–1652.

Dusseault, M.B. and Fordham, C.J. (1994) Time dependent behaviour of rocks, in *Comprehensive Rock Engineering*, Vol. 3 (ed. J.A. Hudson), Pergamon Press, Oxford, pp. 119–149.

Dusseault M.B., Cimolini, P., Soderberg, H. and Scafe, D.W. (1983) Rapid index tests for transitional material. *ASTM Geotechnical Testing Journal*, **6** (2), 64–72.

Ewy, R.T., Bovberg, C.A., Chen, G., Jansson, R. and Pepin, G. (2004) Fatigue testing of hollow cylinders and application to injection well cycling. The 6th North America Rock Mechanics Symposium, Houston, TX, 5–9 June 2004, ARMA/NARMS 04-464.

Fairhurst, C. and Lacabanne, W.D. (1956) Some principles and developments in hard rock drilling techniques. Proceedings of the 6th Annual Drilling and Blasting Symposium, Minnesota University, pp. 15–25.

Fish, B.G.(February 1961) Research in rock drilling and tunneling. *Mining, Electrical and Mechanical Engeer,* 1–13.

Fish, B.G. and Barker, J.S. (1956) *Studies in rotary drilling*. MRE Report No. 209, National Coal Board.

Fjær, E., Holt, R.M., Horsrud, P., Raaen, A.M. and Risnes, R. (1992) *Petroleum Related Rock Mechanics*, Elsevier Science, Amsterdam.

Gardner, G.H.F. and Harris, M.H. (1968) Velocity and attenuation of elastic waves in sands. 9th Annual Logging Symposium, pp. M1–M19.

Gatlin, C. (1960) *Petroleum Engineering*, Prentice-Hall, London.

Ghalambor, A., Hayatdavoudl, A. and Koliba, R.J. (1994) A study of sensitivity of relevant parameters to predict sand production. The 3rd Latin American/Caribbean Petroleum Engineering Conference, Buenos Aires, 27–29 April 1994, SPE 27011.

Giles, C.A., Seesahai, T., Brooks, J.W. and Johnatty, W. (2001) Drilling efficiencies provided by hydraulic thrusting devices. The AADE 2001 National Drilling Conference, Houston, TX, 27–29 March 2001.

Green, S., Judzis, A., Curry, D., Black, A., Prasad, U. and Rogers, J. (2005) Single cutter impact tests investigate deep-well hammer-drilling performance. The SPE Annual Technical Conference and Exhibition, Dallas, TX, 9–12 October 2005, SPE 97173.

Gregory, A.R. (1976) Fluid saturation effects on dynamic elastic properties of sedimentary rocks. *Geophysics*, **41** (5), 895–921.

Griggs, D.T. (1967) Hydrolytic weakening of quartz and other silicates. *Geophysical Journal of the Royal Astronomical Society*, **14**, 19–31.

Griggs, D.T. and Blacic, J.D. (1965) Quartz: anomalous weakness of synthetic crystals. *Science*, **147**, 292–295.

Haimson, B.C. (1978) Effect of Cyclic Loading on Rock, Dynamic Geotechnical Testing. ASTM Special Publication STP 654. American Society for Testing and Materials, Philadelphia, PA, pp. 228–245.

Han, G. and Bruno, M. (2006) Percussion drilling: from lab tests to dynamic modeling. SPE International Oil & Gas Conference and Exhibition in China, Beijing, 5–7 December 2006, SPE 104178.

Han, G. and Dusseault, M.B. (2002) Quantitative analysis of mechanisms for water-related sand production. Proceedings of the SPE International Symposium and Exhibition on Formation Damage Control, Lafayette, LA, 20–21 February 2002, SPE 73737.

Han, G. and Dusseault, M.B. (2003) Description of fluid flow around a wellbore with stress-dependent porosity and permeability. *Journal of Petroleum Science and Engineering*, **40** (1/2), 1–16.

Han, G. and Dusseault, M.B. (2005) Sand stress analysis around a producing wellbore with a simplified capillarity model. *international Journal of Rock Mechanics and Mining Science*, **42** (7–8), 1015–1027.

Han, G., Dusseault, M.B. and Cook, J. (2002) Quantifying rock capillary strength behavior in unconsolidated sand. Proceedings of the SPE/ISRM Rock Mechanics Conference, Irving, TX, 20–23 October 2002, SPE 78170.

Han, G., Bruno, M., Dusseault, M.B. and Xu, B. (2004) Rock nonlinearities in the oil–water environment around a wellbore. Proceedings of 3rd ARMS (Asian Rock Mechanics Symposium), Kyoto, 30 November–2 December 2004, pp. 335–340.

Han, G., Bruno, M. and Lao, K. (2005a) Percussion drilling in oil industry: review and rock failure modelling. The AADE National Technical Conference & Exhibition, Houston, TX, 5–7 April 2005, AADE-05-NTCE-59.

Han, G., Bruno, M. and Dusseault, M.B. (2005b) Dynamically modelling rock failure in percussion drilling. The 40th US Rock Mechanics Symposium, Anchorage, AK, 25–29 June 2005, ARMA/USRMS 05-819.

Han, G., Bruno, M. and Grant, T. (2006) Lab investigations of percussion drilling: from single impact to full scale fluid hammer. The 41st US Rock Mechanics Symposium, Colorado School of Mines, Golden, CO, 17–21 June 2006, ARMA/USRMS 06-96.

Harpst, W.E. and Davis, E.E.(17 March 1949) Rotary percussion drilling. *Oil and Gas Journal*, 182–187.

Hartman, H.L. (1966) The effectiveness of indexing in percussion and rotary drilling. *International Journal of Rock Mechanics and*

Mining Science & Geomechanics, Abstracts, **3** (4), 265–278.

Hawkins, A.B. and McConnell, B.J. (1992) Sensitivity of sandstone strength and deformability to changes in moisture content. *Quarterly Journal of Engineering Geology*, **25**, 115–130.

Heins, R. and Friz, T. (1967) The effect of low temperature on some physical properties of rock. SPE 1714. Society of Petroleum Engineers.

Ho, H.S. (1987) Prediction of drilling trajectory in directional wells via a new rock-bit interaction model. Proceedings of SPE Annual Technical Conference and Exhibition, SPE 16658.

Holt, R.M. (1990) Permeability reduction induced by a nonhydrostatic stress field. *SPE Formation Evaluation*, **5** (4), 444–448.

Huang, H. and Detournay, E. (2008) Intrinsic length scales in tool–rock interaction. *International Journal of Geomechanics*, **8** (1), 39–44.

Huang, H., Detournay, E. and Bellier, B. (1999) Discrete element modelling of rock cutting, in *Rock Mechanics for Industry* (eds B. Amadei, Z. Kranz, G.A. Scott and P.H. Smeallie), Balkema, Rotterdam, pp. 123–130.

Jaeger, J.C., Cook, N.G.W. and Zimmerman, R.W. (2007) *Fundamentals of Rock Mechanics*, Blackwell, Oxford.

John, M. (1972) The influence of loading rate on mechanical properties and fracture processes of rock. CSIR Report ME 1115, p. 28.

Kemurdzhian, A.L., Gromov, V.V. and Shvarev, V.V. (1978) Investigation of the physicomechanical properties of extraterrestrial soils, in *Soviet Progress in Space Studies: the Second Decade of Space Flight, 1967–1977* (eds A.A. Blagonravov*et al.*), Nauka, Moscow, pp. 352–380, (in Russian).

King, M.S. (1969) Static and dynamic elastic moduli of rocks under pressure. Proceedings of 11th Symposium on Rock Mechanics, University of California, Berkely, CA, June 1969.

Kohata, Y., Tatsuoka, F., Wang, L., Jiang, G.L., Hoque, E. and Kodaka, T. (1997) Modelling the non-linear deformation properties of stiff geomaterials. *Geotechnique*, **47** (3), 563–580.

Kömle, N.I., Kargl, G. and Ball, A.J. (2001) Determination of physical properties of planetary sub-surface layers by artificial impacts and penetrometry. *Advances in Space Research*, **28** (10), 1539–1549.

Kong, J., Marx, C. and Palten, P.J. (1996) Mathematical simulation of a spring-free hydraulic drilling hammer and verification of the results by experiment. *Erdol Erdgas Kohle*, **112** (1), 19–25.

Kulhawy, F.H. and Duncan, J.M. (1972) Stress and movements in Oroville Dam. *Journal of the Soil Mechanics and Foundations Division, Proceedings of the American Society of Civil Engineers*, **SM7**, 653–665.

Lama, R.D. and Vutukuri, V.S. (1978) *Handbook on Rock Properties of Rocks*, Trans Tech Publications.

Larson, D.A. and Olson, R.C. (1977) Design considerations of mechanical fragmentation systems for entry development in oil shale, in *Proceedings of the 10th Oil Shale Symposium, April 1977*, Colorado School of Mines Press, Golden, CO, pp. 99–119.

Lebreton, J.P. and Matson, D.L. (2002) The Huygens Probe: science, payload and mission overview. *Space Science Reviews*, **104**, 59–100.

Lee, L.K. and Seed, H.B. (1967) Drained strength characteristics of sands. *Journal of the Soil Mechanics and Foundation Division, Proceedings of the American Society of Civil Engineers*, **SM6**, 117–141.

Leonard, R. (2001) Features – groundwater development – tough down hole drilling demands expand bit options: Ralph Leonard of Numa explains drill bit options for down hole percussion drilling applications. *Water and Wastewater International*, **16** (2), 17.

Le Pennec, T., Jørgen Måløy, K., Flekkøy, E.G., Messager, J.C. and Ammi, M. (1998) Silo hiccups: dynamic effects of dilatancy in granular Flow. *Physics of Fluids*, **12** (12), 3072–3079.

Lhomme, T. (1999) Frictional contact at a rock-tool interface: an experimental study. Master's thesis, University of Minnesota.

Liu, Y., Mavroidis, C., Bar-Cohen, Y. and Chang, Z. (2007) Analytical and experimental study of determining the optimal number of wedge shape cutting teeth in coring bits used in percussive drilling. *Journal of Manufacturing Science and Engineering – Transactions of the ASME*, **129** (4), 760–769.

Lorenz, R.D. and Ball, A.J. (2001) Review of impact penetration tests and theories, in *Penetrometry in the Solar System* (eds N.I. Kömle, G. Kargl, A.J. Ball and R.D. Lorenz), Austrian Academy of Sciences Press, pp. 25–39.

LSPET (The Lunar Sample Preliminary Examination Team) (1973) Preliminary examination of lunar samples, Apollo 17 Preliminary Science Report, NASA Special Publication 330, Johnson Space Center, pp. 7-1–7-46.

Maurer, W.C. (1965) Bit tooth penetration under simulated borehole conditions. *Journal of Petroleum Technology, Transaction of AIME*, **234**, 1433–1442.

McGhee, E.(August 1955) New down-hole tool. *Oil and Gas Journal*, **54** (14), 67.

McGregor, K. (1967) *The Drilling of Rock*, CR Books, London.

McKay, D.S., Heiken, G., Basu, A., Blanford, G., Simon, S., Reedy, R., French, B.M. and Papike, J. (1991) The lunar regolith, in *The Lunar Sourcebook* (eds G.H. Heiken *et al.*), Cambridge University Press, New York, pp. 285–356.

Melamed, Y., Kiselev, A., Gelfgat, M., Dreesen, D. and Blacic, J. (2000) Hydraulic hammer drilling technology: developments and capabilities. *Journal of Energy Resources Technology*, **122** (1), 1–8.

Mellor, M. (1971) Strength and deformability of rocks at low temperatures. US Army Core of Engineers, CRREL-RR-294.

Minear, J.W., Heysse, D.R. and Boonen, P.M. (1996) Initial results from an acoustic logging-while-drilling tool. SPE Annual Technical Conference and Exhibition, Denver, CO, 6–9 October 1996, SPE 36543.

Mission Evaluation Team (1973) *Apollo 17 Mission Report*, Johnson Space Center, Houston, TX, p. 349.

Mitchell, J.K., Houston, W.N., Carrier, W.D. III, and Costes, N.C. (1974) Apollo Soil Mechanics Experiment S-200, Space Sciences Laboratory Series 15, Issue 7, University of California, Berkeley, CA, p. 135.

Moore, H.J., Hutton, R.E., Clow, G.D. and Spitzer, C.R. (1987) Physical properties of the surface materials at the Viking landing sites on Mars, US Geological Survey Professional Paper 1389, US Government Printing Office, Washington, DC, pp. 222.

Morita, N., Gray, K.E., Srouji, F.A.A. and Jogl, P.N. (1992) Rock property changes during reservoir compaction. *SPE Formation Evaluation*, **7** (3), SPE 13099, 197–205.

Morris, R.V., Lauer, H.V. Jr, and Gose, W.A. (1979) Characterization and depositional and evolutionary history of the Apollo 17 deep drill core. Proceedings of the l0th Lunar and Planetary Science Conference, pp. 1141–1157.

Nishimatsu, Y. (1993) Theories of rock cutting, in *Comprehensive Rock Engineering*, Vol. 1 (ed. J.A. Hudson), Pergamon Press, Oxford, pp. 647–662.

Ostrovskii, N.P. (1960) *Deep-Hole Drilling with Explosives*, Gostoptekhizat, Moscow, translated by Consultants Bureau Enterprises, New York.

Papamichos, E., Brignoli, M. and Santarelli, F.J. (1997) An experimental and theoretical study of a partially saturated collapsible rock. *Mechanics of Cohesive-Frictional Material*, **2**, 251–278.

Papike, J.J., Simon, S.B. and Laul, J.C. (1982) The lunar regolith: chemistry, mineralogy, and petrology. *Reviews of Geophysics and Space Physics*, **20**, 761–826.

Parker, R.A., Gahan, B.C., Graves, R.M., Batarseh, S., Xu, Z. and Reed, C.B. (2003) Argonne National Laboratory laser drilling: effects of beam application methods on improving rock removal. The SPE Annual Technical Conference and Exhibition, Denver, CO, 5–8 October 2003, SPE 84353.

Paterson, M.S. and Wong, T.F. (2005) *Experimental Rock Deformation – The Brittle Field*, 2nd edn, Springer-Verlag, Berlin, p. 347.

Paul, B. and Gangal, M.D. (1969) Why Compressive Loads on Drill Bits Produce Tensile Splitting in Rock, SPE 2392.

Paul, B. and Sikarskie, D.L. (1965) A preliminary model for wedge penetration in brittle materials. *Transactions of the American Institute of Mine Engineers*, **232**, 373–383.

Peng, S.S. (1975) A note on the fracture propagation and time-dependent behaviour of rocks in uniaxial tension. *International Journal of Rock Mechanics, Mining Science & Geomechanics, Abstracts*, **12**, 125–127.

Phillips, D.W. (1948) Tectonics of mining. *Colliery Engineering*, **25**, 199–202.

Pixton, D. and Hall, D. (2002) *Advanced Mud Hammer Systems*, DOE Project DE-FC26-97FT34365, Novatek, Provo, UT.

Plumb, R.A. (1994) Influence of composition and texture on the failure properties of clastic rock. Proceedings of EUROCK'94, pp. 13–20.

Podio, A. and Gray, K.E. (1965) Single-blow bit-tooth impact tests on saturated rocks under confining pressure: I. Zero pore pressure. *SPE Journal*, **SPE 1056**, 211–225.

Pollard, D.D. and Fletcher, R.C. (2005) *Fundamentals of Structural Geology*, Cambridge University Press, Cambridge, p. 500.

Pratt, C.A. (1987) Modifications to and experience with percussion air drilling. The SPE/IADC Drilling Conference, New Orleans, LA, 15–18 March 1987, SPE/IADC 16166.

Priest, S.D. and Selvakumar, S. (1982) The failure characteristics of selected British rocks. Report to the Transport and Road Research Laboratory. Imperial College, London, unpublished.

Raaen, A.M., Hovern, K.A., Jøranson, H. and Fjær, E. (1996) FORMEL: a step forward in strength logging. The SPE Annual Technical Conference and Exhibition, Denver, CO, 6–9 October 1996, SPE 36533.

Rabinowicz, E. (1965) *Friction and Wear of Materials*, John Wiley & Sons, Inc., New York.

Rao, K.S., Rao, G.V. and Ramamurthy, T. (1987) Strength of sandstones in saturated and partially saturated conditions. *Geotechnical Engineering*, **18** (1), 99–127.

Reichmuth, D.R. (1963) Correlation of force–displacement data with physical properties of rock for percussive drilling systems, in *Rock Mechanics* (ed C. Fairhurst), Pergamon Press, Oxford, pp. 33–60.

Ren, N.K. and Roegiers, J.C. (1983) Differential strain curve analysis – a new method for determining the pre-existing *in situ* stress state of rock core measurements. Proceedings of the 5th International Conference of the International Society of Rock Mechanics, Melbourne, pp F117–F127.

Reuss, A. (1929) Berechung der Fließgrenze von Mischkristallen auf Grund der Plastizitätsbedingung für Einkristalle. *Zeitschrift fur Angewandte Mathematik und Mechanik*, **9**, 49–58.

Richard, T. (1999) Determination of rock strength from cutting tests. Master's thesis, University of Minnesota.

Richard, T., Germay, C. and Detournay, E. (2007) A simplified model to explore the root cause of stick-slip vibration in drilling systems with drag bits. *Journal of Sound and Vibration*, **305** (3), 432–456.

Ridgeway, R.R., Ballard, A.H. and Bailey, B.L. (1933) A revised Mohs hardness scale. *Transactions of the Electrochemical Society*, **63**, 267.

Roberts, A. (1981) *Applied Geotechnology – A Text for Students and Engineers on Rock Excavation and Related Topics*, Pergamon Press, Oxford.

Ruistuen, H., Teufel, L.W. and Rhett, D. (1996) Influence of reservoir stress path on deformation and permeability of weakly cemented sandstone reservoirs. SPE Annual Technical Conference and Exhibition, Denver, CO, 6–9 October 1996, SPE 36535.

Samuel, G.R. (1996) Percussion drilling . . . is it a lost technique? A review. The Permian Basin Oil & Gas Recovery Conference, Mildland, TX, 27–29 March 1996, SPE 35240.

Santarelli, F.J. and Brown, E.T. (1987) Performance of deep wellbores in rock with a

confining pressure-dependent elastic modulus. Proceedings of the 6th International Congress on Rock Mechanics, Montreal, II, pp. 1217–1222.

Santarelli, F.J. and Brown, E.T. (1989) Failure of three sedimentary rocks in triaxial and hollow cylinder compression tests. *International Journal of Rock Mechanics and Mining Sciences*, **26** (5), 401–413.

Sarda, J.P., Kessler, N., Wicquart, E., Hannaford, K. and Deflandre, J.P. (1993) Use of porosity as a strength indicator for sand production evaluation. 68th SPE Annual Technical Conference, Houston, TX, 3–6 October 1993, SPE 26454.

Schlumberger Educational Services (1987) *Log Interpretation Principles/Applications, Schlumberger Manual*, Schlumberger Educational Services, Houston, TX.

Schmitt, L., Forsans, T. and Santarelli, F.J. (1994) Shale testing and capillary phenomena. *International Journal of Rock Mechanics, Mining Sciences and Geomechanics*, **31** (5), 411–427.

Schubert, H. (1984) Capillary Forces – modelling and application in particulate technology. *Powder Technology*, **47**, 105–116.

Simmons, G. and Brace, W.F. (1965) Comparison of static and dynamic measurements of compressibility of rocks. *Journal of Geophysical Research*, **70**, 5649–5656.

Simon, R. (1964) Transfer of stress wave energy in the drill steel of a percussive drill to the rock. *Journal of Rock Mechanics and Mining Science*, **1**, 397–411.

Sinor, A. and Warren, T.M. (1989) Drag bit wear model. *SPE Drilling Engineering*, 128–136.

Smith, F.W. and Kopczynksi, W. (1961) Oilfield percussion drilling. The 32nd Annual California Regional Meeting of SPE, Bakerfield, CA, 2–3 November 1961, SPE 222.

Smorodinov, M.I., Motovilov, E.A. and Volkov, V.A. (1970) Determinations of correlation relationships between strength and some physical characteristics of rocks. Proceedings of the 2nd Congress of the International Society, for Rock Mechanics, Vol. 2 (3–6), pp. 35–37.

Somerton, W.H., Timur, A. and Gray, D.H. (1961) Stress behavior of rock under drilling loading conditions. The 36th Annual SPE Fall Meeting, Dallas, TX, 8–11 October 1961, SPE 166.

Surkov, Y.A., Barsukov, V.L., Moskalyeva, L.P., Moskaleva, L.P., Kharyukova, V.P. and Kemurdzhian, A.L. (1984) New data on the composition, structure, and properties of Venus rock obtained by Venera 13 and Venera 14. Proceedings of the l4th Lunar and Planetary Science Conference, pp. 393–402.

Swolfs, H.S. (1971) Chemical effects of pore fluids on rock properties, underground waste management and environmental implications. Proceedings of the Symposium of American Association of Petroleum Geologists (AAPG), 6–9 December 1971, Memoir 18, pp. 224–233.

Taylor, G.I. (1923) Stability of a viscous liquid contained between two rotating cylinders. *Philosophical Transactions of the Royal Society of London*, **A223**, 289–343.

Taylor, J.M. (1950) Pore space reduction in sandstone. *Bulletin of American Association of Petroleum Geology*, **34**, 701–716.

Taylor, G.J., Warner, R.D. and Keil, K. (1979) Stratigraphy and depositional history of the Apollo 17 drill core. Proceedings of the l0th Lunar and Planetary Science Conference, pp. 1159–1184.

Tibbitts, G.A., Long, R.C., Miller, B.E., Judzis, A. and Black, A.D. (2002) World's first benchmarking of drilling mud hammer performance at depth conditions. The IADC/SPE Drilling Conference, Dallas, TX, 26–28 February 2002, IADC/SPE 74540.

Tixier, M.P., Loveless, G.W. and Anderson, R.A. (1975) Estimation of formation strength from the mechanical-properties log. *Journal of Petroleum Technology*, **27** (3), SPE 4532, 283–293.

Tokle, K., Hosrud, P. and Bratli, R.K.(October 5–8, 1986) Predicting uniaxial compressive strength from log parameters. 61st SPE Annual Technical Conference and

Exhibition, New Orleans, LA, 5–8 October 1986, SPE 15645.

Topanelian, E. Jr, (1957) Effect of low frequency percussion in drilling hard rock. The SPE 32nd Annual Meeting, Dallas, TX, 6–9 October 1957, AIME 2013.

Treadway, C. (1997) Percussion and down-the-hole hammer drilling: yesterday and today. *Water Well Journal*, **51** (7), 55–59.

Tronvoll, J. and Fjær, E.(August, 1993) Experimental study of sand production from perforation cavities, in *Investigation of Cavity Failures for Sand Production Prediction*, University of Trondheim, Trondheim, pp. 92–106.

Vaniman, D.T., Labotka, T.C., Papike, J.J., Simon, S.B. and Laul, J.C. (1979) The Apollo 17 drill core: petrologic systematics and the identification of a possible Tycho component. Proceedings of the l0th Lunar and Planetary Science Conference, pp. 1185–1227.

Villaescusa, E., Seto, M. and Baird, G. (2002) Stress measurements from oriented core. *International Journal of Rock Mechanics & Mining Sciences*, **39**, 603–615.

Voigt, W. (1910) *Lehrbuch der Kristallphysik*, Teubner, Leipzig.

Walsh, J.B. and Brace, W.F. (1966) Cracks and pores in rocks. Proceedings of the 1st Congress of International Society of Rock Mechanics, Lisbon, Vol. 1, pp. 643–646.

Wanamaker, J.A. (1951) Rotary percussion drilling in West Texas, *World Oil*, (September), 182–187.

Wang, Y. and Dusseault, M.B. (1991) Borehole yield and hydraulic fracture initiation in poorly consolidated rock strata – Part II. Permeable media. *International Journal of Rock Mechanics, Mining Science & Geomechanics*, Abstracts, **28** (4), 247–260.

Wang, Y. and Dusseault, M.B. (2003) A coupled conductive–convective thermo-poroelastic solution and implications for wellbore stability. *Journal of Petroleum Science and Engineering*, **38** (3–4), 187–198.

Warren, T.M. and Armagost, W.K. (June 1988) Laboratory drilling performance of PDC bits. *SPE Drilling Engineering*, SPE 15617, 125–135.

Warren, T.M. and Smith, M.B. (1985) Bottomhole stress factor affecting drilling rate at depth. *Journal of Petroleum Technology*, **SPE 13381**, 1523–1533.

Watters, T. (1995) *Planets: Smithsonian Guides*, Ligature, New York.

West, G. (1994) Effect of suction on the strength of rock. *Quarterly Journal of Engineering Geology*, **27**, 51–56.

Whiteley, M.C. and England, W.P. (1986) Air drilling operations improved by percussion-bit/hammer-tool tandem. *SPE Drilling Engineering*, **SPE 13429**, 377–382.

Wills, P.B., DeMartini, D.C., Vinegar, H.J., Shlyapobersky, J., Deeg, W.F., Woerpel, J.C., Sorrells, G.G. and Adair, R.G.(July 1992) Active and passive imaging of hydraulic fractures. *The Leading Edge*, **11** (7), 15–22.

Yang, J.H. and Gray, K.E.(December, 1967) Single-blow bit-tooth impact tests on saturated rocks under confining pressure: II. Elevated pore pressure. *Society of Petroleum Engineering Journal*, **SPE 1702**, 389–409.

Zacny, K. and Cooper, G. (2007) Coring basalt rock under simulated Martian atmospheric conditions. *Mars Journal*, **Mars 3**, 1–11.

Zarnecki, J.C., Leese, M.R., Garry, J.R.C., Ghafoor, N. and Hathi, B. (2002) Huygens' surface science package. *Space Science Reviews*, **104**, 593–611.

Zarnecki, J.C., Leese, M.R., Hathi, B., Ball, A.J., Hagermann, A., Towner, M.C., Lorenz, R.D., McDonnell, J.A.M., Green, S.F., Patel, M.R., Ringrose, T.J., Rosenberg, P.D., Atkinson, K.R., Paton, M.D., Banaszkiewicz, M., Clark, B.C., Ferri, F., Fulchignoni, M., Ghafoor, N.A.L., Kargl, G.n., Svedhem, H., Delderfield, J., Grande, M., Parker, D.J., Challenor, P.G. and Geake, J.E. (2005) A soft solid surface on Titan as revealed by the Huygens surface science package. *Nature*, **438**, 792–795.

Zoback, M.D. (2007) *Reservoir Geomechanics*, Cambridge University Press, Cambridge, p. 449.

Internet Links

Meyer, C., Lunar Sample Compendium, Apollo 17 samples 70001–70009, on-line resource, http://www-curator.jsc.nasa.gov/lunar/compendium.cfm, accessed May 2008.

Tempel 1, http://www.nasa.gov/mission_pages/deepimpact/main/index.html, accessed 25 May 2008.

The International Society for Rock Mechanics lists many suggested methods for testing of rock. ASTM International also has established standards for rock and soils testing. Both of these societies support refereed journals that publish articles related to rock testing.

International Society of Rock Mechanics: http://www.isrm.net/.

ASTM Geotechnical Testing Journal and Standards: http://www.astm.org.

The following commercial sites are of interest. Also, many universities around the world have excellent testing facilities for petroleum rock mechanics.

http://www.sintef.no/.

http://www.terratek.com/.

http://www.corelab.com/PetroleumServices/Advanced/RockMech.asp.

http://www.reslab.com.

http://www.metarocklab.com.

http://www.csiro.au/science/RockMechanicsTesting.html.

Keywords/Abstract

Dear Author,

Please check and/or supply keywords and an abstract. These will not be included in the print version of your chapter but in the online version.

If you do not supply an abstract, the section heading will be used instead.

Keywords: drilling; excavation; rocks; stress; energy; borehole; rock breakage.

Author Query

1. Please update Ref. (Dagrain et al., 2008).
2. Please update Ref. (Detournay and Richard, 2008).
3. Please update Ref. (Detournay et al., 2008).
4. Please check the equation (2.47) is missing.